Carbon Fiber Electrode Arrays for Cortical and Peripheral Neural Interfaces

by

Elissa J. Welle

A dissertation submitted in partial fulfillment
of the requirements for the degree of
Doctor of Philosophy
(Biomedical Engineering)
in the University of Michigan
2021

Doctoral Committee:

Associate Professor Cynthia A. Chestek, Chair
Associate Professor Tim M. Bruns
Associate Professor William C. Stacey
Professor James D. Weiland

Elissa J. Welle

elissajw@umich.edu

ORCID iD: 0000-0001-5141-7656

Dedication

This dissertation is dedicated to my grandmothers, the trunks of my family tree.

To Nana Beyers, whose aura has remained with me through my family's stories of the Brooklyn Beyers. Your lasting legacy was the untimely wish that all women should be able to attend college. You would be proud Nana, now all your granddaughters are doctors. Democratic socialists, too.

And to Grandma Welle, the only grandparent I knew. I wish you could be here to sing a song of celebration with me. I miss your beautiful singing and watching you swim across the lake. Your vibrant love of others lives on in me.

Acknowledgements

Thank you to my family. Mom, Dad, Cristin, Jonathan, Ethan, Declan, Kiernan, Elliott, Aunt Joan, Uncle Peter, Aunt Rita, and Colin. I love you all. You've listened to my worries, fears, and cries with the grace that I needed. Nearly every single word of encouragement I have written down somewhere. Little droplets of hope misting my life when I was feeling withered. I am thrilled to be together after these long months apart and show you how I've blossomed.

Thank you to my advisor, Cindy. I knew from the moment we met that I wanted you to be my advisor, and I'm so grateful that you were. I was guided through this journey under the expert navigation of your kindness, wisdom, and love of science. You've understood me and my strengths and struggles in a way most people can only dream of being understood. I wish you all the success and happiness in your life.

Thank you to my friends. Maggie, Emeline, Vitchyr, Sharon, Shannon, and Hillary, among many others, your long-distance friendship kept me sane and laughing. My Michigan friends, I'm grateful that I have too many to name, but you know who you are. Your hugs, texts, and weekend plans were the bright spots in my life these last five years. We've made many memories and had our fair share of adventures, too. Cheers, to lifelong friendships all around.

Thank you to my lab members. There are no better people to watch Guy Fieri or critique Babybel cheese with. I'm proud to be the first and last safety cadet of the lab, and I expect that picture to stay on the wall forever. I miss seeing you every day in lab. I miss our daily antics at lunch. Thank goodness for Zoom for keeping us close during the last year.

Thank you to my committee members. I'm grateful for the relationships I've had with each one of you. Jim, your guidance early on in my PhD put me on the right track and gave me the confidence I needed. Thank you for supporting me along the way. Bill, your encouragement during my quals reminded me that my work was meaningful, and I needed that reminder. Thank you also for gathering us all at your house to socialize every year. Tim, your steadiness through the SPARC project was invaluable to me. Thank you for the numerous hours of help during the final stretch of experiments. I couldn't have done it without you. And thank you also for your engagement with the BME graduate student community. I'm glad the rest of BME has access to your excellent mentorship.

Thank you to my church community. You were not my escape from school, you were my anchor amid school. I felt most myself with you all in my life.

Thank you to my therapists. You got me through my hard times and celebrated with me during my good ones.

Thank you to my pets, for lightening my mood. Skye, Dundee, Finnegan, you are such good pups.

Finally, thank you to my Benjamin. My light. I loaf you.

Table of Contents

List of Tables

List of Figures

Abstract

Neural interfaces create a connection between neural structures in the body and external electronic devices. Brain-machine interfaces and bioelectric medicine therapies rely on the seamless integration of neural interfaces with the brain, nerves, or spinal cord. However, conventional neural interfaces cannot meet the demands of high channel count, signal fidelity, and signal longevity that these applications require.

I investigated the damage resulting from conventional Utah arrays after multiple years of implantation in the cortex of a non-human primate as a possible explanation for these limitations. The neuron density around the electrode shanks was compared to the neuron density of nearby healthy tissue, finding a 73% loss in density around the electrodes. The explanted arrays were imaged and characterized for degradation. Coating cracks, tip breakage, and parylene cracks were the most common degradation type. A significantly higher number of tip breakage and coating crack occurrences were found on the edges of the arrays as compared to the middle. In this work, I made clear the need for a minimally damaging alternative to the Utah electrode array.

Neural interfaces composed of carbon fiber electrodes, with a diameter of 6.8 microns, could enable a seamless integration with the body. Previous work resulted in an array of individuated carbon fiber electrodes that reliably recorded high signal-to-noise ratio neural signals from the brain for months. However, the carbon fiber arrays were limited by only 30% of the electrodes recording neural signals, despite inducing minimal inflammation. Additionally, it was relatively unknown if carbon fibers would make suitable long-term peripheral neural interfaces.

Here, I illustrate the potential of carbon fiber electrodes to meet the needs of a variety of neural applications.

First, I optimized state-of-the-art carbon fiber electrodes to reliably record single unit electrophysiology from the brain. By analyzing the previous manufacturing process, the cause of the low recording yield of the carbon fiber arrays was identified as the consistency of the electrode tip. A novel laser cutting technique was developed to produce a consistent carbon fiber tip geometry, resulting in a near tripling of recording yield of high amplitude chronic neural signals. The longevity of the carbon fiber arrays was also addressed. The conventional polymer coating was compared against platinum iridium coating and an oxygen plasma treatment, both of which outperformed the polymer coating. In this work, I customized carbon fiber electrodes for reliable, long-term neural recording.

Secondly, I translated the carbon fiber technology from the brain to the periphery in an architecture appropriate for chronic implantation. The insertion of carbon fibers into the stiffer structures in the periphery is enabled by sharpening the carbon fibers. The sharpening process combines a butane flame to sharpen the fibers with a water bath to protect the base of the array. Sharpened carbon fiber arrays recorded electrophysiology from the rat vagus nerve and feline dorsal root ganglia, both structures being important targets for bioelectric medicine therapies. The durability of carbon fibers was also displayed when partially embedded carbon fibers in medical-grade silicone withstood thousands of repeated bends without fracture. This work showed that carbon fibers have the electrical and structural properties necessary for chronic application.

Overall, this work highlights the vast potential of carbon fiber electrodes. Through this thesis, future brain-machine interfaces and bioelectric medicine therapies may utilize arrays of sub-cellular electrodes such as carbon fibers in medical applications.

Chapter 1: Introduction

Neural interfaces connect the brain, nerves, or spinal cord to the outside world [1]. Neural information is transmitted to the body in the form of electrical stimulation and transmitted from the body to the neural interface through the recording of electrical signals [2]. In addition to an electrical connection, neural interfaces also interact with neural targets in mechanical, material, and structural ways [3]. It is therefore important to consider neural interfaces through the holistic lens of their size, shape, and material composition, in addition to their electrical conductivity [4]. This work focuses on one neural interface, the carbon fiber electrode array. Carbon fibers are small 6.8 μm diameter wires of carbon [5]. They can be sharpened, cut, and bent to match the requirements of the neural target, all while maintaining an intrinsic structural integrity, despite their small size [6], [7]. Further, this small size allows them to minimally perturb the region of implantation, permitting them to access difficult or sensitive areas of the body [8]. Here, I examine carbon fiber electrode arrays in the context of the motor cortex of the brain and various peripheral structures, as well as in comparison to conventional neural interfaces.

1.1 Clinical applications of neural interfaces

1.1.1 Brain-machine interfaces

Neural interface engineering is motivated by recent successes in brain-machine interfaces (BMIs) and bioelectric medicine (BM) therapies [9], [10]. In both BMIs and BM therapies, a neural interface is inserted into a cortical or peripheral region to record neural signals and transmit them to an external computer [11], [12]. BMIs translate the information obtained from the motor cortex of the brain into physical movements of a computer cursor or robotic hand [13]. Patients suffering

from tetraplegia have used BMIs to interact with their world independently, in functions like shaking President Obama's hand or sipping from a cup of coffee [14], [15]. BMIs record brain signals using the only clinically approved device, the Utah electrode array (UEA) [16]. UEAs are composed of 100 silicon shanks spaced 400 µm apart in a 10 x 10 grid [17]. Each shank tapers from 80 µm to roughly 20 µm across the length of 1.5 mm [18]. BMI studies show that the UEAs' effectiveness decreases over time as the number of channels recording neural signals decreases along with the amplitude of the neural signals themselves [19], [20]. Sophisticated algorithms can extract the necessary information from the remaining channels to enable BMIs to remain useful for a number of years [21], [22]. However, BMI performance suffers from the reduced quality and quantity of neural information recorded using the UEA.

1.1.2 Bioelectric medicine therapies

BM therapies rely on neural interfaces to stimulate the body's circuitry in the treatment of a range of chronic disorders [11], [23]. BM therapies provide more specific, localized treatments than medical pharmacological treatments because they interact directly with the peripheral nervous system, whose nerves lie closer to the intended target organs [24]. BM therapies treat systemic illnesses such as hypertension and depression through the stimulation of the cervical vagus nerve [25]–[27]. In non-clinical settings, researchers are experimenting with stimulation of dorsal root ganglia in felines to trigger bladder voiding [28], [29]. While stimulation is the primary focus of BM research, the interconnection of the peripheral nervous system and the organs targeted by therapies remains relatively unknown. A detailed map of the peripheral nervous system may enable increasingly specific and useful therapies and closed-loop control of stimulation [30]. To that end, BM research needs a recording array that can record high fidelity information from the small amplitude action potentials that travel down nerves [31]. An ideal BM recording array would also

contain a large number of electrodes, similar to the specifications of an ideal BMI recording array [32]. However, the architecture of peripheral neural interfaces poses the additional design constraints of interfacing with neural structures of a variety of sizes, shapes, and stiffnesses [33]. Many of these structures are delicate and less than 1 mm in overall size [34]. Therefore, BM therapies also require a neural interface that does not disrupt or damage the nearby tissue.

1.2 Neural interface designs

1.2.1 Limitations of conventional Utah electrode arrays

There are several indications that the UEA, or the modified multi-length slanted UEA (USEA) used in the periphery, is not well suited for chronic implantation in the body for BMIs or BM therapies [18], [35], [36]. Studies using electrical stimulation found that the stimulation threshold needed to trigger a response increased over time [10]. Additionally, neural signals recorded by the UEA, and their slanted array counterparts, decrease in quantity and quality over time [37]. Sophisticated algorithms circumvent some of this loss of information, but the majority of UEA electrodes fail within the first year [20]. Histological analysis of neural tissue after UEA extraction indicates that a heightened immune response, scar formation, and electrode degradation result from a chronic implant in the brain and nerves [38]. Blood vessels are often ruptured during insertion, which triggers an inflammatory response [39]. Reactive oxide species often accumulate at the site of injury and cause electrode degradation [40]. In the nerve, fibrotic tissue forms an encapsulating sheath around implanted UEAs, which may result in the UEA being pushed out of the nerve [36], [41]. In the few studies examining the effect of chronic UEA implantation in non-human primate cortices, it appears that neuron density decreases near the electrode sites, similar to what has been shown in other long term silicon studies in the brain [42], [43]. The nearby

immune response, surrounding scarring, and local neuronal population decrease may all be contributing factors to the UEA signal loss over time.

1.2.2 Advanced small or soft neural electrodes

Recent electrode research has focused on ways to mitigate the problems facing UEAs [44], [45]. Some adjustments include decreasing the total size of the metal electrodes [46]–[48]. Others replace metal backplanes with softer materials, such as polyimide or PDMS [49]–[53]. In several instances, thin polymer arrays, some with features as small as 5 μm in diameter, were tested *in vivo* to great histological success [54]. One group used coiled carbon nanotube yarn (10–20 μm diameter) to record spontaneous neural signals in a rat vagus nerve [55], [56]. However, small soft electrodes rely on an insertion agent, such as a metal shank or wire, to penetrate into the brain or nerve [4], [9], [57]. This complicates surgical procedures, impedes inserting a large number of electrodes, and indicates the inherently fragile nature of the thin, soft material [9], [58].

1.2.3 State-of-the-art carbon fiber recording technology

Carbon fibers, however, are sub-neuronal sized with a 6.8 μm diameter and are strong enough to maintain structural integrity during insertion. Our lab has been at the forefront of this push for ultra-small carbon fiber electrodes. In 2012, we published the first-ever results showing that insulated carbon fiber electrodes (diameter 8 μm), can record electrophysiology signals from a rat brain [5]. This work revolutionized the carbon fiber electrode field, which previously was dominated by glass-capillary-insulated carbon fibers used to detect neurotransmitters [59]. The smaller device footprint of the parylene-insulated device caused very little damage to the brain tissue after months of implantation [60]. Next, an array of carbon fiber electrodes was fabricated for recording multi-channel neural signals from the brain. The carbon fibers in this array required a dissolvable stiffening agent for bulk insertion [61]. The signals were high amplitude and

histological analysis showed very a minimal inflammatory response [8]. However, despite the good signal fidelity and histology, only 30% of the carbon fiber electrodes remained functional once inserted into the tissue [62]. Another group provided preliminary results indicating that carbon fibers can stimulate autonomic nerves and record evoked responses in a rat [63]. These past examples illustrate the potential utility of carbon fiber electrodes in a variety of settings but leave room for improvement.

1.3 Summary of Thesis

In this thesis, I examine the ways in which carbon fiber electrode arrays can be improved and applied to neural systems across the body. Additionally, I point out the ways in which the only clinically approved electrode array does not align with the goals of a chronic neural interface. The work included in this thesis highlights the potential for wide scale use of carbon fiber arrays in BMI and BM applications.

In Chapter 2, I design and test the next iteration of carbon fiber electrodes for brain recording [6]. I analyze the previous manufacturing process to decipher the cause of the low recording yield of our carbon fiber arrays. Despite high amplitude recordings obtained from the rat motor cortex for several months and a healthy neuronal population within the critical 0–50 μm distance around the recording site after months of implantation, just 30–40% of functional carbon fibers recorded neural signals from the brain. In this work, I investigate a laser cutting method to reliably fabricate stable carbon fiber electrode sites and increase the long-term recording yield to greater than 80%. I also identify potential improvements to the impedance-reducing metal tip coating, such as platinum iridium or oxygen plasma etching. I evaluate the laser cut carbon fiber electrodes in chronic studies of the rat motor cortex and compare the new technology to previous carbon fiber arrays. I also verify the recording capability of alternative electrode coatings and

perform accelerated testing analysis. In this chapter, I identify and evaluate key improvements to the carbon fiber brain recording arrays.

In Chapter 3, I discuss the application of carbon fiber brain technology to the peripheral nervous system for the betterment of BM therapies [7]. The sub-cellular size of carbon fibers, the resulting lack of inflammatory response, and the strength of carbon fiber materials provide ample justification for fabricating a carbon fiber array capable of chronic peripheral nerve implantation. To that end, I sharpened the carbon fiber electrode tips to enable self-inserting penetration into peripheral neural structures. The sharpened carbon fibers self-inserted into – and recorded from – rat cervical vagus nerve, feline dorsal root ganglia, and the rat cortex. Physiologically relevant neural signals corresponding to bladder pressure and cutaneous brushing were recorded from the feline dorsal root ganglia. In this work, I also harnessed the inherent strength and anti-fatigue properties of the carbon fiber material by partially embedding them in silicone. When embedded in silicone, carbon fibers bent without breaking. The work in this chapter shows that carbon fiber electrodes can make suitable peripheral neural interfaces with the potential for chronic application.

In Chapter 4, I look back at traditional UEAs to analyze the histological and mechanical outcomes of long-term chronic implantation in the cortex of a non-human primate. Four UEAs were implanted in the right and left sensory and motor cortices of one NHP for 1.6 to 2.3 years. After UEA extraction, the tissue was stained for neurons and the UEAs were imaged under scanning electron microscopy. I analyzed neuron density near electrode holes and compared this to neuron density in nearby healthy tissue. I also analyzed the scanning electron microscopy images of the extracted UEAs for degradation of the electrode surface, namely tip breakage, parylene delamination, shank fracture, abnormal debris, coating cracks, and parylene cracks. This

chapter points to the damage caused by UEAs in the brain and the damage to UEAs during long term implant.

In summary, this thesis examines ultra-small carbon fiber neural interfaces suitable for next generation BMIs and BM therapies and solidifies the need for a minimally damaging neural interfaces through examination of damage caused by conventional UEAs.

Chapter 2: Ultra-small Carbon Fiber Electrode Recording Site Optimization and Improved In Vivo Recording Yield

A version of this chapter has been published in the Journal of Neural Engineering.

Elissa J. Welle, Paras R. Patel, Joshua E. Woods, Artin Petrossians, Elena della Valle, Alexis Vega-Medina, Julianna M. Richie, Dawen Cai, James D. Weiland, and Cynthia A. Chestek

2.1 Abstract

Objective. Carbon fiber electrodes may enable better long-term brain implants, minimizing the tissue response commonly seen with silicon-based electrodes. The small diameter fiber may enable high-channel count brain-machine interfaces capable of reproducing dexterous movements. Past carbon fiber electrodes exhibited both high fidelity single unit recordings and a healthy neuronal population immediately adjacent to the recording site. However, the recording yield of our carbon fiber arrays chronically implanted in the brain typically hovered around 30%, for previously unknown reasons. In this paper we investigated fabrication process modifications aimed at increasing recording yield and longevity. *Approach.* We tested a new cutting method using a 532 nm laser against traditional scissor methods for the creation of the electrode recording site. We verified the efficacy of improved recording sites with impedance measurements and *in vivo* array recording yield. Additionally, we tested potentially longer-lasting coating alternatives to PEDOT:pTS, including PtIr and oxygen plasma etching. New coatings were evaluated with accelerated soak testing and acute recording. *Main results.* We found that the laser created a consistent, sustainable 257 ± 13.8 μm^2 electrode with low 1 kHz impedance (19 ± 4 kΩ with PEDOT:pTS) and low fiber-to-fiber variability. The PEDOT:pTS coated laser cut fibers were

found to have high recording yield in acute (97% >100 μV_{pp}, N = 34 fibers) and chronic (84% >100 μV_{pp}, day 7; 71% >100 μV_{pp}, day 63, N = 45 fibers) settings. The laser cut recording sites were good platforms for the PtIr coating and oxygen plasma etching, slowing the increase in 1 kHz impedance compared to PEDOT:pTS in an accelerated soak test. *Significance.* We have found that laser cut carbon fibers have a high recording yield that can be maintained for over two months *in vivo* and that alternative coatings perform better than PEDOT:pTS in accelerated aging tests. This work provides evidence to support carbon fiber arrays as a viable approach to high-density, clinically-feasible brain-machine interfaces.

2.2 Introduction

Brain-machine interfaces (BMIs) translate neural dynamics into therapeutic technologies for the restoration of movement and sensation to critically disabled patients [12]. Exciting recent proof of concept demonstrations using neural interfaces to treat neurological disorders include multi-degree-of-freedom control of paralyzed limbs using functional electrical stimulation [64], [65], novel prosthetic hands with tens of degrees of freedom [66], [67], more widely available upper limb exoskeletons [68], and systems of implantable devices with realistic power consumption for neural recording with high channel count [69]–[71]. Future BMIs will aim to translate movement intention into more naturalistic or complex movements, such as control of individual fingers [21], [72]–[74].

BMI research relies heavily upon the Utah array [75], the only multi-shank electrode approved for clinical use, for decoding intended movements from motor cortex [13], [64], [65], [76]–[79]. High density neural electrodes have also been applied to other biological systems to restore complex functions, such as closed loop bladder control [80], vision restoration [81]–[83], or memory encoding [84]. However, Utah arrays and other conventional silicon-based arrays are

associated with a number of limiting factors that may inhibit a dramatic expansion of channels or increase in longevity. For example, it has been observed that the number of channels on silicon-based arrays capable of recording neural activity, termed recording yield, decreases over time and is associated with a decrease in the amplitude of recorded action potentials [19], [85]. Experiments using Michigan-style silicon arrays typically begin with a recording yield of 50% or less in the first week [62], [86], [87] and with amplitudes of 150 μV or lower. This may be due in part to an electrode configuration that spans multiple cortical layers containing neurons. However, any decrease in yield or amplitude may threaten the utility of the entire array. In BMI experiments, decode performance can be maintained by using threshold crossings instead of well-isolated action potentials [85], common average referencing [87], and high frequency field potentials [88] that may reflect underlying spiking activity [89]. However, the inability to record individual spikes may limit the creation of intuitive neural prosthetics. Thus, there is a pressing need for robust, stable, high-density neural interfaces.

Tissue damage and inflammation may play a role in the degradation of electrode performance over time. There is damage during insertion of conventional silicon-based electrodes, often disrupting the blood brain barrier and triggering an immune response [89]. Once inserted, an electrode's presence often induces an inflammatory tissue response in the surrounding tissue that can be much larger than the electrode footprint itself [90]. Chronic inflammation leads to fibrotic encapsulation, distancing the recording electrode from healthy neurons [91], [92]. Finally, the lining of the encapsulation is composed of activated macrophages and foreign body giant cells that produce enzymes and reactive oxygen species, which contribute to electrode degradation [93]. Therefore, in maintain high quality signals on all channels over time, it is critically important to minimize tissue damage and inflammation.

With the overall goal of minimizing scarring, groups have developed electrodes that are softer, smaller, or both. Soft electrodes more closely align with the brain's Young's modulus [94] and show some improvement in histological results. Most soft devices have been similar in size to conventional probes, however [95], which is not sufficient by itself to eliminate the immune response. Very little scarring has been observed near soft probes that have neuron sized dimensions [96]–[98]. However, like larger soft electrodes, small-footprint devices may need to rely on an insertion shuttle, such as an injection needle [96], microwire [99], [100], or a temporary stiffening agent [101], which adds to surgical complexity.

Multiple groups have made cellular scale probes out of higher Young's modulus materials, such as carbon fiber [5], [61], [63], [102]–[105], silicon carbide [46], or glass [106], that can be driven directly into the brain. At these size scales, even stiff materials are quite flexible and cause much less scarring than conventionally sized probes [62]. However, most small-footprint devices were developed recently and have not been rigorously evaluated in terms of recording yield in long term studies comparable to the Utah array. For example, a recent white paper of high-density, small electrodes reported a low acute yield [99]. This could be explained by the fact that small electrodes typically have recording sites of smaller surface area, which can make it difficult to achieve the low impedances often needed for single unit recording. Increasing the surface area is one possible solution, which has unknown effects on the yield of small single unit spike detection [102], [107]. Even without active scar formation around the probe, biofouling of adherent proteins within the first few days of implant can cause a sharp increase in electrical impedance [108]. It is also possible for neurons to be present but quiescent due to inflammation [109], which could also lead to lower apparent recording yield.

In our own group, previous carbon fiber arrays yielded neural units on fewer than half of the electrodes on average when chronically implanted in motor cortex [61], with signals decreasing after several months despite minimal scarring [62]. In the present study, we investigated potential reasons for this low yield, and attribute it primarily to inconsistent tip exposure from manual cutting of the carbon fibers. We explored heat-based cutting approaches and found that a novel laser cutting technique achieved consistent recording site exposure in a batch, repeatable process with minimal labor. While only increasing the surface area to 257 μm^2, this technique resulted in electrodes of relatively small geometric volume and significantly lower average impedance than the conventional scissor cut electrodes. Furthermore, laser cut electrodes enabled high unit yield in both acute and chronic recordings in the rat motor cortex. Additionally, this study found that longer-lived electroplated materials, such as platinum iridium, or carbon-only surface modifications, such as oxygen plasma surface roughening, perform well on laser cut electrodes in accelerated soak tests as compared to a conventional electrodeposited polymer coating.

2.3 Methods

2.3.1 Experimental design

In this work, we first explored fabrication methods to expose the recording surface of carbon fiber electrodes. The most suitable exposure method was characterized by *in vivo* recording yield in acute and chronic settings. The chronic recording yield was compared to our previous scissor cut carbon fiber electrode from Patel *et al* 2016 [62]. Secondly, we tested our standard electrode coating material for degradation and explored alternative coatings and treatments for the recording site.

2.3.2 Carbon fiber array fabrication

The electrodes in this study were composed of electrically conductive strands of carbon fiber (T-650/35 3 K, Cytec Thornel, Woodland Park, NJ). The 6.8 µm diameter carbon fibers were attached to printed circuit boards (PCBs) designed to facilitate electrical recordings. Electrode fabrication followed the steps previously described in Patel *et al* 2015 and 2016 [61], [62]. In brief, individual, uninsulated carbon fibers were manually placed and electrically connected to the bond pad or exposed gold trace of the PCB using conductive silver epoxy (H20E, Epoxy Technology Inc., Billerica, MA). After baking, the junction was covered with an insulating epoxy (353NDT, Epoxy Technology Inc., Billerica, MA). The entire device was insulated with approximately 800 µm of parylene-C using 2 g of precursor (PDS2035CR, Specialty Coatings Systems, Indianapolis, IN). Electrode tip fabrication continued in Section 2.3.3.

Several array designs were used in this study, all previously described in Patel *et al* 2015 and 2016 [61], [62]. The first array, a large PCB design called a Wide Board (WB), contained up to 8 fibers per array and was used in the accelerated soak tests for ease of handling [62]. The second array, a smaller PCB called a ZIF array, contained up to 8 fibers per array and was developed for *in vivo* neural recordings using the Tucker-Davis Technologies ZIF headstage (Tucker-Davis Technologies, Alachua, FL) [61]. In some cases, the ZIF array was exchanged for a third array, a preliminary device containing up to 16 fibers that uses a permanent shuttle, similar to that shown in Patel *et al* 2015, to avoid PEG application during insertion.

2.3.3 Carbon fiber electrode tip preparation

After parylene-C insulation, fibers were manually cut to the final desired length using stainless steel microsurgical scissors (15002-08, Fine Science Tools, Foster City, CA) or ceramic microsurgical scissors (15750-11, Fine Science Tools, Foster City, CA) under a stereoscope equipped with a reticle. Carbon fibers were cut to 500 µm for SEM imaging, 2 mm for in vivo

implantation, and 5 mm for accelerated soak testing. Fibers were laser cut using a 532nm Nd:YAG pulsed laser (LCS-1, New Wave Research, Fremont, CA; 5 mJ/pulse, 5 ns pulse duration) at a power of 900mW and intensity of 100% in combination with a Karl Suss probe station (LC3, SUSS MicroTec, Garching, Germany) for optical alignment. The device was secured to a glass slide and the tip of each fiber was aligned within the 22 µm by 75 µm window of the laser. The laser was pulsed an average of 3 times to completely remove the roughly 75 µm length of the fiber that was within the window.

2.3.4 Electrochemical deposition of coatings and oxygen plasma treatment

The exposed site on laser cut fibers was electrodeposited with a solution of 0.01M 3,4ethylenedioxythiophene (483028, Sigma-Aldrich, St. Louis, MO) and 0.1 M sodium p-toluenesulfonate (152536, Sigma-Aldrich, St. Louis, MO) by applying 600 pA/channel for 600 s to form a layer of poly(3,4-ethylene dioxythiophene):sodium p-toluenesulfonate (PEDOT:pTS) [5], [61], [62], [110]. PEDOT:pTS was deposited on scissor cut fibers by applying 100 pA/channel, as previously done in our carbon fiber work [61], [62]. High-surface area electrodeposited platinum-iridium (PtIr) coating (Platinum Group Coatings, Pasadena, CA) was deposited onto the exposed section of the laser cut carbon fibers using a process described previously by Petrossians *et al* 2011 [111]. The presence of PtIr after electrodeposition was confirmed by an increase in current drawn during cyclic voltammetry (CV) and a decrease in 1 kHz impedance measured by electrochemical impedance spectroscopy (EIS). Fibers were treated with oxygen plasma (O_2P) in the Glen 1000P Plasma Cleaner (pressure 200 mT, power 300 W, time 120 s, oxygen flow rate 60 sccm, and argon flow rate 7 sccm) by placing the arrays on a floating tray beneath active plasma bombardment.

2.3.5 Electrochemical impedance spectroscopy (EIS) and cyclic voltammetry (CV)

To characterize fabrication and deposition steps, three-electrode EIS measurements were taken with a PGSTAT12 Autolab potentiostat (Metreohm/Eco Chemie, Utrecht, Netherlands) controlled by the vendor supplied NOVA software. Fibers were submerged by 1 mm in 1x phosphate buffered saline (PBS, BP3994, Fisher, Waltham, MA). An Ag|AgCl electrode (RE-5B, BASi, West Lafayette, MA) served as a reference electrode and a stainless steel rod was selected as the counter electrode to better match the stainless steel bone screw counter electrode used *in vivo* [61], [62]. EIS measurements were obtained by applying a 10 μV_{RMS} signal from 10 Hz to 31 kHz. CV measurements were obtained by sweeping three times between 0.8 V to −0.6 V and 0.8 V at a scan rate of 1 Vs^{-1}. Prior to EIS measurements, PtIr coated electrodes were conditioned using a scan rate of 0.5 Vs^{-1} with step potential of −0.01 V for a total of 13 sweeps in order to remove any extraneous debris [112]. EIS and CV measurements were analyzed using custom MATLAB (Mathworks, Natick, MA) scripts. Fibers were cleaned in deionized water after EIS measurements.

2.3.6 Scanning electron microscopy and energy-dispersive x-ray spectroscopy (EDS)

SEM images were collected of carbon fibers at various stages of the fabrication and experimental process. All images were collected in either the Nova Nanolab 200 DualBeam SEM (FEI, Hillsboro, OR) or the Tescan Rise SEM (Tescan Orsay Holding, Brno–Kohoutovice, Czech Republic), using 2 kV or 16 kV accelerating voltage and 0.21 nA or 165.90 µA current, respectively. SEM analysis of different fiber tip cutting methods used ZIF arrays with 500 µm length fibers mounted on standard SEM pin stub mounts (16111, Ted Pella, Redding, CA) using double sided carbon tape (16073, Ted Pella, Redding, CA). The mounted fibers were then sputtered with gold for one to two minutes (11429, Structure Probe, Inc. West Chester, PA) and imaged on the Nova Nanolab SEM at either a 45° or 60° tilt with a 12 kx magnification using the

Everhart-Thornley detector. Similarly, plating evaluation was performed with ZIF arrays prepared with 2 mm fiber lengths, coated with PEDOT:pTS or treated with O_2P, sputtered with gold for two minutes, and imaged in the Nova Nanolab SEM using the same settings. The PtIr-coated fibers of 2 mm length were prepared on ZIF arrays and imaged in the Tescan Rise SEM using a low vacuum acquisition mode, allowing for imaging without gold coating. The fibers were imaged using the low vacuum secondary electron Tescan detector at a 20° tilt with a magnification of 8 kx. Fibers were imaged after the accelerated soak test in the Tescan Rise using low vacuum acquisition mode. Charging was reduced by touching the 5 mm long fibers to a piece of silicon wafer during imaging. SEM images of explanted fibers were collected in the Tescan Rise using low vacuum acquisition mode after 1 min and 20 s of gold sputtering. EDS analysis was performed using the Tescan Rise to chemically characterize the PEDOT:pTS coated carbon fibers before and after the accelerated soak test. The analysis was done at 10 kV at a working distance of 15 mm, acquiring both an EDS map and spectra signals of the coated surface.

2.3.7 Accelerated soak test setup

Similar to our previously documented accelerated soak test assembly in Patel *et al* 2016 [62], the soak test was conducted on 8-fiber WBs in a water bath (FSGPD05, Thermo Fisher, Hampton, NH) set to 50° C. Four WBs were secured to the underside of the lid of a glass jar using a 16-pin DIP socket secured with epoxy (353ND-T, Epoxy Technology Inc., Billerica, MA). The lids were fastened to the soak test jars, which were filled with 1x PBS solution (BP3994, Fisher, Waltham, MA) to a level such that the tips of the fibers were submerged by several millimeters into the PBS. Three jars were used to hold a total of 12 WBs, three from each of the following categories: laser cut PEDOT:pTS-coated fibers, laser cut PtIr-coated fibers, laser cut O_2P-etched fibers, and uninsulated bare fibers that served as the control. The control boards received the same

fabrication steps prior to parylene-C coating. They were used to indicate any degradation of the PCB itself. The WBs were randomly distributed between the jars at the beginning of the experiment. At the time of measurement, the jars were removed from the soak test bath and each WB was rinsed in deionized water. Normal EIS measurements were then conducted for each WB. Following measurements, the jars were then rinsed, filled with fresh PBS, and returned to the water bath with the WBs secured. The position of the jars within the water bath was shifted following each measurement to account for any heating irregularities in the water bath.

Similar to Patel *et al* 2016 [62], and the works by Green *et al* [110] and Hukins *et al* [113], the simulated aging time of the heated fibers can be determined by the equation

$$t_{37} = t_T \times Q_{10}^{(T-37)/10}$$

in which t_{37} is the simulated aging time at 37 °C, t_T is the amount of real time that the samples have been kept in heat at temperature T, and Q_{10} is an aging factor that is equal to 2, according to ASTM guidelines for polymer aging [114]. Calculating the simulated time for $t_T = 1$ and T = 50 °C results in $t_{37} = 2.46$. This value of 2.46 is the acceleration factor and all real time measurements are scaled by this amount to obtain the simulated time.

2.3.8 Electrode preparation for surgical implantation

EIS measurements were collected and electrophysiology ground and reference wires (AGT05100, World Precision Instruments, Sarasota, FL) were soldered to the ZIF PCB, each with roughly 5 mm of exposed contact at the end. Fibers attached to ZIF arrays were rinsed with deionized water prior to prepping with 2050MW poly(ethylene glycol) (PEG, 295906, Sigma Aldrich, St. Louis, MO), a non-toxic material that temporarily stiffens the fibers in order to increase insertion depth without fiber buckling, as explored in Patel *et al* 2015. Briefly, the row of 8 fibers were gently rested on an aluminum foil surface lightly coated with mineral oil (M8410,

Sigma Aldrich, St. Louis, MO). A coil of wire was wrapped around a soldering iron set to 500 °F and used to pick up a single flake of 2050MW PEG. Once melted, the droplet of liquid PEG was brushed along the length of the fibers, leaving the very tip of fibers exposed. The fibers easily released from the oiled surface once the PEG cooled.

2.3.9 Surgical procedures for implantation of carbon fibers

All animal procedures were approved by the University of Michigan Institutional Animal Care and Use Committee. Surgical procedures of carbon fiber arrays used adult male Long Evans rats weighing 400–500 g. Vitals were monitored during surgery using a pulse oximeter and rectal temperature probe. Animal preparation for carbon fiber insertion followed the procedure described in Patel *et al* 2015. In brief, once the skull surface was cleaned, a burr bit (19008–07, Fine Science Tools, Foster City, CA) was used to drill holes for the bone screws (19010-00, Fine Science Tools, Foster City, CA). Acute rats received one bone screw near the posterior edge of the skull, while chronic rats had seven holes placed around the periphery of the skull. Next, a 2.5 mm by 2.5 mm craniotomy was made over the right hemisphere's motor cortex according to a reference atlas [115]. Following dura resection, the PEG coated fibers on the ZIF array were brought near the surface of the brain with fibers aligned along the anterior-posterior axis. The exposed fibers were driven into the brain manually using a stereotactic manipulator until the PEG coated portion reached the surface of the brain, at which point a small amount of Lactated Ringer's (2B2324, Baxter, Deerfield, IL) was applied to the craniotomy via syringe to dissolve the PEG nearest to the brain. The fibers were then manually driven in further until the final target depth of 1.2 mm to layer V was reached [116] and all remaining PEG was dissolved. Acute non-survival surgeries were performed on N = 3 animals, with one animal receiving a ZIF array and the other two each receiving a permanent shuttle array.

For chronic animals, silicone (3–4680, Dow Corning, Midland, MI) was added via syringe to the craniotomy to cover fiber length above the brain surface to the junction with the PCB. Ground and reference wires were then wound around the ground bone screw. Dental acrylic was applied to the skull, bone screws, and PCB to form a headcap. The skin flaps were sutured together at the anterior and posterior ends of the headcap and triple antibiotic ointment was liberally applied. Animals were then removed from the stereotax and allowed to recover on a heated pad placed under their cage. Chronic survival surgeries were performed on N = 4 animals, with two animals receiving ZIF arrays and two receiving permanent shuttle arrays.

2.3.10 Electrophysiology recordings

The collection of all electrophysiology recordings was done using a ZC16 headstage, RA16PA pre-amplifier, and RX5 Pentusa base station (Tucker-Davis Technologies, Alachua, FL). During data acquisition, the pre-amplifier high-pass filtered at 2.2 Hz, anti-alias filtered at 7.5 kHz, and sampled at a rate of 25 kHz. Recordings done with acute implants took place while the rats were under ketamine/xylazine anesthesia, while the chronic electrophysiology measurements were collected on awake and behaving animals, as described in Patel *et al* 2015. Each recording session lasted 3 and 10 min for acute and chronic implants, respectively. This study also analyzed chronic electrophysiology recordings from N = 6 animals reported in Patel *et al* 2016. The neural data was collected on N = 77 scissor cut PEDOT:pTS coated carbon fiber electrodes mounted on ZIF arrays.

2.3.11 Histological analysis

Animals were transcardially perfused and brains were extracted, as detailed in Patel *et al* 2016, after 91 or 94 days of implant. Explanted headcaps were soaked in enzymatic cleaning solution (J-J2252, Enzol, Johnson & Johnson, New Brunswick, NJ) for 1.5 hours, rinsed in dionized water, and dried prior to SEM imaging. For immunohistochemical analysis, we chose six

100 µm thick slices that contained the targeted region of motor cortex where the carbon fiber electrodes were implanted. To assess neuronal health, we stained the sections to visualize all cells, neurons, astrocytes, and microglia. The slices were incubated in 4% (w/v) paraformaldehyde (P6148, Sigma Aldrich, St. Louis, MO) (pH 7.40) in 1x PBS overnight as a post-fixation step and washed in 1x PBS at room temperature for two hours the following day. We then placed the slices in a blocking solution containing StartingBlock™ (PBS) Blocking Buffer (37578, Thermo Fisher, Waltham,MA) and 1.0% Triton X-100 (T8787, Sigma Aldrich, St. Louis, MO), overnight at room temperature, followed by three washes in 1x PBS containing 0.5% Triton X-100 (0.5% PBS-T) at room temperature, one hour each. The slices were incubated in a solution containing StartingBlock™ (PBS) Blocking Buffer, 1.0% Triton X-100, and the following primary antibodies: Mouse anti-NeuN (MAB377, Millipore, Billercia, MA), Rabbit anti-GFAP (Z0334, Dako, Carpinteria, CA), and Guinea Pig anti-Iba-1 (234004, Synaptic Systems, Goettingen, Germany), for three nights at 4 $^{\circ}$C in a covered chamber. The slices were then triple rinsed with 0.5% PBS-T, with each wash lasting one hour. The slices were then incubated in a solution containing StartingBlock™ (PBS) Blocking Buffer, 1.0% Triton X-100, and the following secondary antibodies: Donkey anti-Mouse IgG Alexa Fluor 647 (715-605-150, Jackson, West Grove, PA), Donkey anti-Rabbit IgG Alexa Fluor 546 (A10040, Life Technologies, Waltham, MA), Donkey anti-Guinea Pig Alexa Fluor 488 (706-545-148, Jackson, West Grove, PA), and DAPI (D1306, Invitrogen, Grand Island, NY), for two nights at 4 $^{\circ}$C in a covered chamber. All primary and secondary antibodies were used at a 1:250 dilution. The slices were rinsed twice in 0.5% PBS-T, each wash one hour long, followed by a final overnight wash in 1x PBS. The slices were then cover slipped with VECTASHIELD Antifade Mounting Medium (H-1000, Vector

Laboratories, Burlingame, CA) and left to dry overnight to prepare for imaging with a laser scanning confocal microscope.

Imaging was performed on a Zeiss LSM 780 Confocal Microscope using a C-Apochromatic 10x/0.45W M27 water immersion objective. A 15x15 tile, 75 µm z-stack was acquired to visualize all four stains on the whole slice. Track 1 scanned with the 405 nm laser, track 2 scanned with the 488 nm and the 633 nm lasers, and track 3 scanned with the 543 nm laser. All laser intensities were adjusted manually to prevent pixel saturation and ranged from 1.2-35% laser power. The gain and contrast were altered during image processing in FIJI.

2.3.12 Neural data analysis

We used two methods of electrophysiology data analysis, one to spike sort in a semi-automated fashion and another to detect bipolar waveforms at set thresholds. Analysis was performed on chronic data collected 7 days after implant once recordings were believed to stabilize [117], and on day 63 or 64 after implant. Prior to analysis, chronic data was cleaned by removing time snippets containing headstage or movement artifacts. Spike sorting was conducted in Offline Sorter (OFS, Plexon, Dallas, TX) on 180 s of data common average referenced between intact fibers within each animal [87]. We made sure that common average referencing did not introduce false waveforms into datasets with small n by invalidating artifacts that appeared across all channels. For each recording session, channels were high-pass filtered (250 Hz corner, 4th order Butterworth) and waveforms were detected at a −3.5*RMS threshold. Cluster centers were then identified in principle component space using a K-means sorting method and obvious noise clusters were invalidated [118], as determined by a trained operator. Remaining waveforms were then clustered using an automated mixture of Gaussian model (standard expectation-maximization) with fixed number of iterations, between 1 and 6 [118]. Units with similar

amplitude and waveform shape were combined. For each sorted unit, we collected the average peak-to-peak waveform amplitude. Carbon fiber electrodes with discernible units following this method of analysis were considered viable in the recording yield calculation and were analyzed further using the bipolar detection method described below.

The second method of neural data analysis identified bipolar waveforms of un-referenced data at a set voltage cut off on viable electrodes identified using the previous cluster sorting method. After high-pass filtering, 50 s of clean data from each intact fiber was thresholded at −45 μV. The fibers that did not detect identifiable units in the OFS technique were not included in this analysis. The resultant waveforms from the threshold crossing were then determined to be bipolar using several constraints: the minimum peak must occur within the 0.33 ms of the negative threshold crossing, followed by the maximum peak within 0.53 ms, and the rising edge following the minimum peak must pass a +40 μV threshold within 0.49 ms of the negative threshold crossing. The peak-to-peak voltage amplitudes of the bipolar waveforms were then grouped by size and the percentage of channels that detected waveforms of set amplitude were determined. A minimum of 10 waveforms within 50 s were needed in order for the channel to be counted at that threshold.

2.3.13 Statistical analysis

One kilohertz impedance magnitudes were compared between cut and coating groups using a Welch's two-sample, one-tailed t-test using 0.01 alpha level. The increase in 1 kHz impedance during the accelerated soak test was compared between groups using a Welch's two-sample, one-tailed t-test using a 0.01 p-value. All calculations were carried out in MATLAB.

2.4 Results

2.4.1 Improved electrode tip fabrication with laser cutting

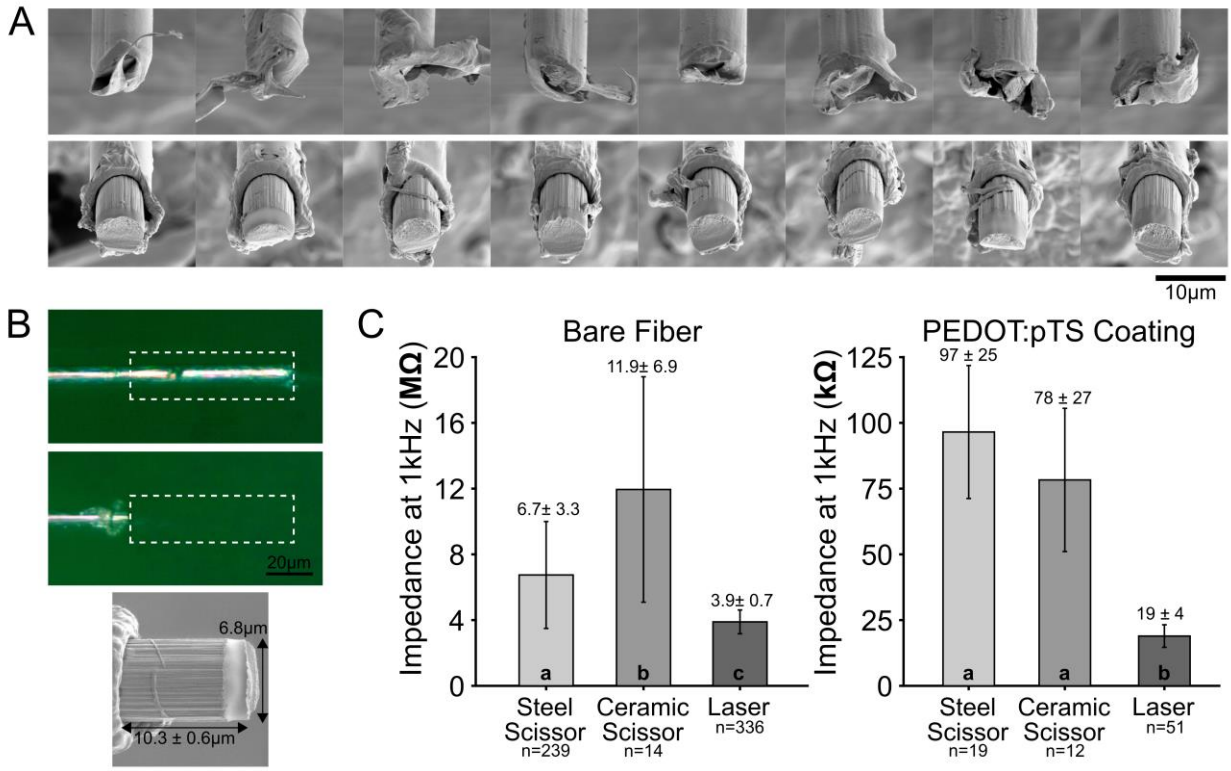

Figure 1 Comparison of scissor and laser cutting methods. (A) Scanning electron microscopy (SEM) images of parylene-c insulated carbon fibers cut with stainless steel microsurgical scissors (top) and with a pulsed green light laser (bottom). Exposed electrode sites at the end of the steel scissor cut fibers are inconsistently exposed from surrounding parylene-c and appear jagged, while the amount of removed parylene-c is more consistent between laser cut fibers. (B) Images of a parylene-c coated fiber before (top) and after (middle) laser cutting. Roughly 75 μm of the fiber is removed by the laser within the window outlined by the white dashed box. A representative laser cut fiber (bottom) shows a clear melted edge of parylene-c above the cleaned carbon fiber surface (10.3 ± 0.6 μm from the tip with a 6.8 μm diameter). (C) 1 kHz impedance plots for fibers cut by steel scissors, ceramic scissors, and the laser. Left: 1 kHz impedance values of bare fibers following each cutting method. Right: 1 kHz impedance values after electrochemical deposition of PEDOT:pTS. Note the difference in units between plots. Bars in a group labeled with different letters are statistically different ($p < 0.01$). All values are listed as mean ± standard deviation.

The basis for this work was to investigate the underlying limitation of previous chronic implants of carbon fiber arrays in which a low percentage of implanted carbon fiber electrodes was able to record neural units, despite immediate healthy neuronal tissue adjacent to recording sites at time of euthanasia. Firstly, we hypothesized that the problem could lay in our fabrication process, and began by evaluating the method used to create the recording site at the carbon fiber tip. Specifically, in our previous studies, carbon fibers were cut using microsurgical stainless steel scissors immediately after insulating the device with parylene-C as previously explained in Patel *et al* 2015 [62].

We evaluated this approach using SEM images of carbon fiber tips after being cut with steel scissors (N = 8 fibers). As shown in Figure 1A, steel scissor cutting often caused the parylene-C to fold over the electrode recording site, partially or completely enclosing the recording active surface. Out of eight fibers viewed, the over folding was qualitatively observed in seven cases. Fibers also exhibited a jagged and irregular carbon surface, often depressed from the parylene-C edge. Seeking more consistency, we also tried cutting fibers with scissors of a harder ceramic material. However, these scissors had similar difficulties when qualitatively evaluated. While we achieved a near perfect cut using a focused ion beam with gallium ions, this approach required tens of minutes per fiber on a high cost tool and was not further pursued.

We then sought a heat based cutting method that would allow for rapid cutting of many fibers with high fiber-to-fiber consistency and controllable amounts of parylene-C removal. We tried multiple laser-based approaches and chose a 532 nm Nd:YAG pulsed laser to ablate sections of parylene-C along the carbon length to create electrode sites. By increasing the laser power to 900 mW, it was possible to cleanly cut the carbon fiber tip with several pulses (3 pulses, N = 184 fibers). As qualitatively shown in Figure 1A, this method reliably revealed more surface area at the electrode method reliably revealed more surface area at the electrode tip compared to mechanical cutting techniques. Parylene-C was burned back an average of 10.3 ± 0.6 μm from the tip (N = 8 fibers), for an average surface area of 257 ± 0.6 μm^2, assuming a 6.8 μm diameter (Figure 1B). Predictably, this had large implications for electrode impedance. Figure 1C shows the 1 kHz impedance for bare fibers cut by both scissor methods and the laser. Impedance is significantly different between traditional steel scissor cut fibers (N = 239 fibers) and laser cut fibers (N = 336 fibers), with impedance values decreasing from 6.7 MΩ to 3.9 MΩ ($p < 0.01$). The standard deviation of laser cut fibers is also lower than steel cut fibers, 720 kΩ and 3.3 MΩ,

respectively. Unexpectedly, cutting with ceramic scissors (N = 14 fibers) resulted in a high average impedance of 11.9 ± 6.9 MΩ, significantly different than steel scissor ($p < 0.05$) and laser cut fibers ($p < 0.01$).

To transform these fibers into functional recording sites, we applied an additional conductive coating of PEDOT:pTS that has been used in our previous carbon fiber work [5], [61], [62]. As expected, the PEDOT:pTS coating lowered the 1 kHz impedance dramatically in all cases (Figure 1C). The resulting 1 kHz impedance of cut fibers was 97 ± 25 kΩ for steel scissors (N = 19 fibers), 78 ± 27 kΩ for ceramic scissors (N = 12 fibers), and 19 ± 4 kΩ for the laser (N = 51 fibers). This difference was significant between steel scissors and laser ($p < 0.001$), ceramic scissors and laser ($p < 0.001$), but not between the two scissor types ($p > 0.05$). All results hereafter referencing scissor cutting utilize steel scissors. Given the visual consistency of the laser cut fibers and the reduced impedance value and variability between laser cut fibers, we continued our testing with laser cut fibers *in vivo*.

2.4.2 Recording yield increase for laser cut fibers coated with PEDOT:pTS

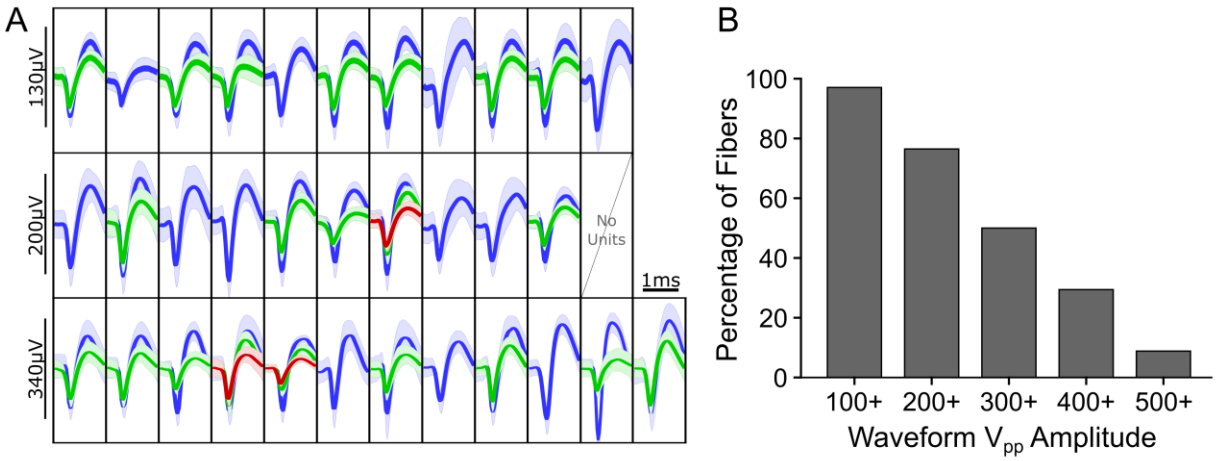

Figure 2 Acute electrophysiology data from laser cut PEDOT:pTS fibers. (A) Neural units sorted using semi-automated clustering methods with a fixed threshold level of −3.5*RMS in N = 3 rats with N = 34 fibers. Multiple units recorded on the same fiber are represented by multiple colors and shown as a mean ± standard deviation. Fibers are grouped by approximate size of the amplitude of the largest recorded unit. One fiber did not record clusterable units. (B) Percent of implanted fibers from (A) that detected bipolar waveforms greater than set peak-to-peak amplitude voltage levels.

Given the extremely small cross section of cellular-scale electrodes, including carbon fibers, and the very high density of neurons in cortex, it has been unclear why the unit yield has not been near 100%, at least in a short chronic setting before any material failures. While this could be related to insertion damage, silent neurons, or anesthesia, we evaluated here whether these lower impedance and more consistent electrode tips could enable the acute recording of neural activity on every channel. We tested this by acutely implanting 34 laser cut PEDOT:pTS-coated fibers into the layer V of the motor cortex at a 1.2 mm depth in three rats. To quantify these waveforms in an objective manner, we took several different approaches. First, we evaluated the number of clusterable units detected on each electrode using a semi-automated sorting method. With a set threshold of −3.5*RMS, we used principal component analysis and both K-means and a mixture of Gaussians sorting methods on this data. The resulting spike panel is shown in Figure 2A. While many of these units encompassed waveforms across a range of amplitudes, 97% of PEDOT:pTS-coated laser cut electrodes recorded clusterable units in this acute setting. We recorded a total of 57 units across the 34 electrodes, averaging 1.7 units/electrode, with an average unit amplitude of 150.6 ± 80.2 μV_{pp} (mean ± sd).

Second, we broadly evaluated the range of bipolar waveforms amplitudes that the electrodes could detect from any nearby neural activity. Based on the noise level of our setup, we set a threshold at −45 μV and checked for clear bipolar 1 ms long waveforms. Under ketamine, bipolar waveforms of at least 85 μV_{pp} amplitude appeared on 97% of all carbon fiber electrodes, consistent with healthy firing neurons within recording range of almost every electrode tip. A histogram of the percent of electrodes with recorded waveforms larger than increasing amplitude values is shown in Figure 2B. A total of 97% of electrodes recorded waveforms of amplitudes larger than 100 μV, 76% had waveforms greater than 200 μV, 50% had waveforms greater than

300 µV, 29% of electrodes had waveforms greater than 400 µV, and 9% had waveforms greater than 500 µV. We found from these acute tests that PEDOT:pTS-coated laser cut carbon fiber electrodes have a high recording yield of clusterable single units and record high amplitude bipolar waveforms.

The results from our acute tests prompted us to further evaluate the long-term effectiveness of laser cut PEDOT:pTS carbon fibers. We therefore chronically implanted 4 rats with a total of 45 laser cut carbon fibers and compared the chronically recorded neural activity from laser cut fibers to our previous work using scissor cut fibers at days 7 and 63/64. Within the first week of implant, biofouling and the associated impedance increase [108], tissue swelling, and fluid build up cause low and inconsistent recording yields [117]. We chose to examine day 7 when biofouling and tissue recovery have stabilized and PEDOT:pTS aging is likely not to have occurred by that

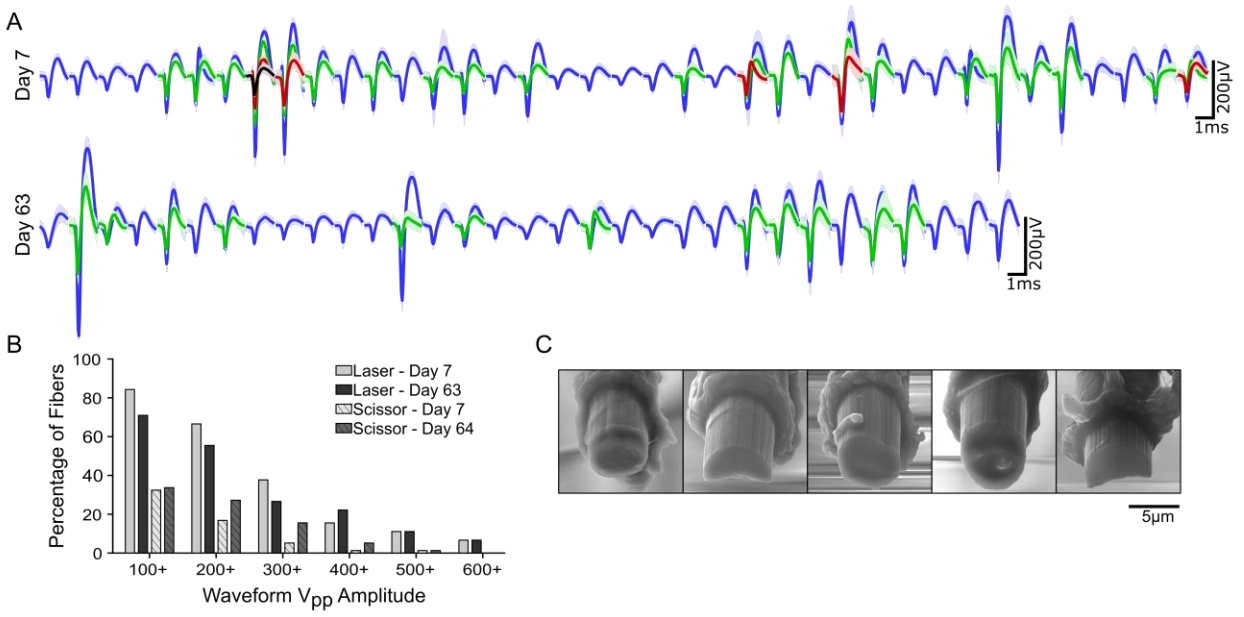

Figure 3 Chronic electrophysiology data from laser cut PEDOT:pTS fibers. (A) Neural units sorted using a semi-automated clustering method with a fixed threshold level of −3.5*RMS, recorded 7 days (top) and 63 days (bottom) after implantation in N = 4 rats with N = 45 fibers. Multiple units recorded on the same fiber are overlaid and represented by multiple colors, shown as a mean ± standard deviation. Fibers that did not record units are not shown. (B) Percent of laser cut fibers from (A) and previous scissor cut fibers from Patel et al 2016 that recorded bipolar waveforms greater than set peak-to-peak amplitude voltage levels. The recording yield of laser cut fibers was statistically higher than that of scissor cut fibers at both day 7 and 63/64 across all waveform amplitudes ($p < 0.01$). (C) SEM images of explanted laser cut carbon fiber electrodes (N = 1 rat, 5 fibers) after 94 days of implant. There is a lack of apparent roughness from PEDOT:pTS coating.

point. After two months of implant, however, any mechanical failures or PEDOT:pTS degradation may have occurred.

Chronically recorded neural activity is shown in Figure 3. We analyzed the data using the same methodology as the acute recordings. A semi-automated spike sorting showed a 84% recording yield of laser cut PEDOT:pTS coated fibers on day 7 (N = 45 fibers) with an average amplitude of 172 ± 96 µV on day 7 (Figure 3A). Viewing 50 s of artifact-free data, the same −45 µV and +40 µV thresholds with minimum peak constraint were applied (Figure 3B). Similar to the acute data, 84% of electrodes had units larger than 100 µV, 67% of electrodes had units larger than 200 µV, 38% of electrodes had units larger than 300 µV, 16% of electrodes had units larger than 400 µV, 11% of electrodes had units larger than 500 µV, and 7% of electrodes had units larger than 600 µV. We applied these same semi-automated sorting techniques to reanalyze the day 7 neural data collected on steel scissor cut fibers from Patel *et al* 2016 and found a 180% increase in recording yield from this previous study [62]. For the same waveform amplitudes values, the recording yield of implanted scissor cut PEDOT:pTS coated fibers on day 7 was 32%, 17%, 5%, 1%, 1%, and 0% (N = 77 fibers).

By day 63, the recording yield of laser cut fibers remained high at 71% (N = 45 fibers), shown in Figure 3. The average amplitude of units on day 63was observed as 171 ± 109 µV (Figure 3A). Analyzed in the same manner as previous data, 71% of electrodes had units larger than 100 µV, 56% of electrodes had units larger than 200 µV, 27% of electrodes had units larger than 300 µV, 22% of electrodes had units larger than 400 µV, 11% of electrodes had units larger than 500 µV, and 7% of electrodes had units larger than 600 µV (Figure 3B). The scissor cut recording data from Patel *et al* 2016 followed a similar pattern on day 64 as on day 7 [62]. For the same waveform amplitude values, the recording yield of implanted scissor cut fibers on day 64 was 34%, 27%,

16%, 5%, 1%, and 0%. The recording yield of laser cut fibers was statistically higher than that of scissor cut fibers at both day 7 and 63/64 across all waveform amplitudes ($p < 0.01$). This suggests that not only do laser cut fibers have higher chronic recording yield, but also larger amplitude units. After 3 months, two of the four rats exhibited complete failure due to grounding or breakage, while the remaining two rats maintained a recording yield of 79% (N = 24 fibers).

We performed histology on tissue slices several hundred microns dorsal from the recording tip on two animals with laser cut electrodes. Arrays were implanted roughly 2 mm lateral from midline in the anterior half of the brain. Similar to Patel *et al* 2016, it was difficult to identify holes in the tissue corresponding to the location of implanted fibers, however the similarity between hemispheres points to minimal damage from the 8 µm carbon fiber electrodes. Images of explanted fibers for one rat are shown in Figure 3C. Fibers appear intact without any attached biological debris, which may be due to enzymatic cleaning after explant, but do not appear to have obvious PEDOT:pTS coating.

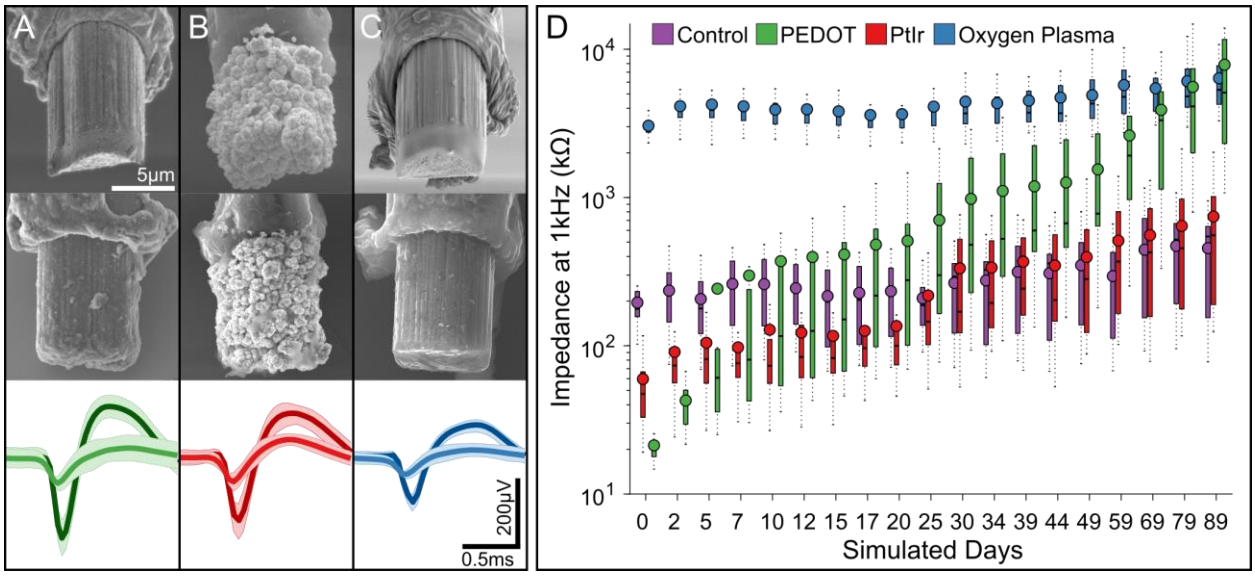

Figure 4 Comparison between PEDOT:pTS and alternative coatings, PtIr and O2P. (A–C) Representative SEM images and example neural recordings of PEDOT:pTS (A), PtIr (B), and O2P (C) coated laser cut fibers. SEM images are shown before (top) and after (middle) the accelerated soak test. Neural recordings from coated fibers that obtained the largest V pp amplitude single units (bottom) are shown as mean ± standard deviation. (D) 1 kHz impedance values obtained during the accelerated soak test over 89 simulated days presented as box-and-whisker plots with the mean plotted as a circle. Original 1 kHz impedance values for each coating are plotted on Day 0. Colors here correspond to the coating type that obtained the single units in A–C.

Table 1 Accelerated soak test trends. Summary of linear regression coefficients, standard error, p-value, and coefficient of determination for the mean 1 kHz impedance values for each coating type during the accelerated soak test over 89 simulated days.

Coating	Slope (kΩ/Day)	SE	p-value	R^2
PEDOT:pTS	71.5	7.6	3.7^{-8}	0.8390
PtIr	7.7	0.3	2.0^{-15}	0.9773
O_2P	30.7	2.9	7.0^{-9}	0.8675
Control	2.9	0.3	2.3^{-8}	0.8482

2.4.3 Impedance increase associated with PEDOT:pTS degradation

Laser cut carbon fibers coated with PEDOT:pTS facilitated promising neural recording results and increased the overall recording yield of our electrode arrays to 97% and 84% in acute and 7day chronic time frames. However, within weeks of chronic implant, the laser cut PEDOT:pTS electrodes exhibited a decrease in recording yield and an increase in 1 kHz impedance, similar to that of our previous scissor cut PEDOT:pTS electrodes [62]. The 1 kHz impedance of the chronically implanted laser cut electrodes began at 107 ± 139 kΩ on day 1 and increased to 1.2 ± 1.0 MΩ on day 7, 2.5 ± 2.0 MΩ on day 63, and 2.7 ± 1.8 MΩ on day 91/94 (N = 45 fibers, mean ± sd). This increase of roughly 2.6 MΩ was similar to that of previous chronic scissor cut PEDOT:pTS experiments. The chronic 1 kHz impedance values from Patel *et al* 2016 at the same time points were 670.8 s ± 540.7 kΩ, 1.7 ± 1.3 MΩ, 2.8 ± 1.7 MΩ, and 2.9 ± 1.8 MΩ (N = 77 fibers, mean ± sd). While recording systems with high input impedance amplifiers, as are often used in neuroscience research, can partially mitigate the noise generated by the high impedance electrodes, it may be critical for other applications, such as multi-year implantable medical devices, that lower 1 kHz electrode impedance be maintained.

It was unclear, however, if the increase in impedance *in vivo* was driven by PEDOT:pTS degradation, biofouling, or some other factor. Characterizing the electrode coating in an accelerated soak test removes the complications of biofouling and tissue thermal noise, allowing for a direct comparison of long-term impedance changes between recording site treatments. Therefore, we submerged the PEDOT:pTS-coated fibers in PBS solution heated to 50 $^{\circ}$C for 36 days, equivalent to a simulated 88.64 days [62]. Similar to our previous work, the impedance of PEDOT:pTS laser cut fibers increased dramatically over the 36 day accelerated soak test, seen in Figure 4D. Before testing, the average PEDOT:pTS 1 kHz impedance was 21 ± 5 kΩ, as expected (Figure 4D day 0, N = 23 fibers). SEM images of PEDOT:pTS coated fibers immediately after electrodeposition appear characteristically roughened by the thin layer of PEDOT:pTS coating (Figure 4A, top row). After approximately 7 simulated days in the accelerated soak test, the impedance rose by 1300% to 297.4 ± 459 kΩ (N = 23 fibers). By the end of the soak test, the average PEDOT:pTS 1 kHz impedance was 7.9 ± 7.6 MΩ (N = 21 fibers), indicating substantial PEDOT:pTS loss or degradation. Figure 4D shows this increasing trend in the 1 kHz impedance values of the PEDOT:pTS coated fibers. SEM images collected after the accelerated soak test showed a smoothed carbon fiber surface with little to no roughness from PEDOT:pTS coating and some visible dried saline debris (Figure 4A, middle row). We characterized the integrity of the PEDOT:pTS coating after the soak test using energy dispersive x-ray spectroscopy (EDS). We observed a decrease in sulfur composition from 6.6% (N = 2 fibers) to 1.6% ± 0.75% (N = 20 fibers).

The observed impedance increase and apparent PEDOT:pTS degradation led us to explore other potential coating options in a preliminary study. We explored both platinum iridium (PtIr) and patterning of the carbon itself with oxygen plasma. PtIr is commonly used in long-term

medical devices [119] and has been shown to be an effective coating of microelectrodes for neural recording [112]. Coating carbon fibers with approximately 2 µm of PtIr (B) resulted in a 1 kHz impedance of 71.0 ± 82.5 kΩ (Figure 4D day 0, N = 137 fibers). We attribute the decreased impedance to the rough surface of the PtIr and the electroactive nature of the PtIr alloy [120]. We also evaluated carbon-only uncoated laser cut tips that had been roughened with oxygen plasma (O_2P), seen in Figure 4C. The O_2P treatment pits the surface of the carbon, reducing the 1 kHz impedance to 3.0 ± 1.0 MΩ (Figure 4D day 0, N = 119 fibers), within range capable of recording neural activity using a high impedance amplifier.

We qualitatively checked that the coatings thoroughly covered the surface of the carbon recording site without increasing the volume of the electrode. The SEMs showed that both PEDOT:pTS and PtIr conformally coated the recording site with some over plating up the shank, as shown in Figure 4A-B. PtIr did appear to result in a slight volumetric increase, which was deemed acceptable. As expected, the O_2P treatment smoothed the overall shape of the carbon. In a single acute test to check the viability of the coated electrodes, isolated single units were detected on both PtIr-coated and O_2P-treated fibers, seen in Figure 4B-C. We used the automatic OFS sorting technique described above and determined the maximum peak-to-peak amplitude of each coating type in this single acute recording session to be 396 µV, 324 µV, and 233 µV for PEDOT:pTS, PtIr, and O_2P, respectively (Figure 4A-C).

To evaluate longevity, we quantitatively compared the change in 1 kHz impedance values of PtIr and O_2P fibers in an accelerated soak test against our PEDOT:pTS results (Figure 4D). Control boards of uninsulated bare fibers were placed with the coated fibers in the soak test to indicate degradation of the PCB. We found that the 1 kHz impedance of PtIr fibers increased by 684 kΩ (N = 24 fibers) during the course of the soak test, a significantly lower increase than the

7.8 MΩ (N = 21 fibers) increase of PEDOT:pTS fibers ($p < 0.001$, Figure 4D). The PtIr coating was intact on the majority of fibers after the soak test with a minimal amount of saline debris (Figure 4B, middle row), but in one third of the cases the PtIr appeared partially detached (N = 8 of 24 fibers). The O_2P fibers increased by 3.3 MΩ (N = 24 fibers, Figure 4D) and showed minimal saline debris (Figure 4C, middle row). Control circuit boards showed slight degradation, accounting for 260 kΩ of the overall 1 kHz impedance increase (N = 24 fibers, Figure 4D). A linear regression model was fit to the daily average 1 kHz impedance values for each coating type, the slope, standard error, p-value, and correlation coefficient of which are shown in Table 1. We found that the slope of the 1 kHz impedance data of PEDOT:pTS coated fibers was 9 times steeper than that of PtIr.

2.5 Discussion

Here, we validated a laser cutting technique that produced electrodes of approximately 257 μm^2 surface area, achieving a much larger apparent neuron recording yield than our previous carbon fiber work [62]. We believe that the increase in recording yield is in part due to more consistent exposure of carbon at the tip, a volumetrically compact geometry with increased surface area, and a reduction in 1 kHz impedance. The recording site created by laser cutting may provide a stable platform for any impedance reducing coating or treatment and result in a high recording yield. Our results here suggest that it may be possible for low damage, cellular scale electrodes to achieve high recording yield with sufficiently reliable manufacturing and materials.

The high recording yield may be a result of the more consistent, less variable laser cut electrode site. This is supported by SEM inspection and reduced variance in impedance measurements (Figure 1). The yield may also be a product of the cylindrical geometry and increased surface area of the laser cut recording site. The surface area increased to 257 μm^2 from

the previous 36 μm^2 when the electrode shape changed to a cylinder from a disc. The large exposure of the laser cut electrode site may increase access to more neurons in the surrounding tissue in three dimensions, whereas the scissor cut electrode may be more limited to neurons beneath the disk electrode. Yet, the laser cut electrode design is still volumetrically compact, with the longest dimension extending just 10 µm across the voltage field. This compactness may lend itself to sampling from a smaller portion of the electrical field, which may enable the recording of overall larger amplitude signals [92].

The high yield we observed may also be explained by the low 1 kHz impedance produced from the laser cut, which resulted in a larger surface area. Previous carbon fiber recording electrodes have also benefited from an increased surface area, most notably those that use fire sharpening [63], [102], [104]. In one such study, approximately 90 µm of uninsulated fiber was exposed in order to reduce the impedance into a recording-capable range of roughly 1 MΩ without the use of additional coatings [102]. However, the relationship between impedance and yield is not well understood and the large increase in impedance over the roughly two months of implant may have accounted for the small but noticeable yield decrease from 84% to 71% over two months [121]. This may indicate that recording yield may be steadily maintained if impedance is below the input impedance of the recording system amplifier [121]. Examples of silicon electrodes without additional conductive coatings have reported negligible recording yields, showing the need for lower impedance [62], [87]. Recording from neurons smaller than pyramidal cells found in layer 5 of the cortex may require the smaller surface area, lower impedance electrodes developed in this work. While further improvements are desired in tip stability, laser cut PEDOT:pTS coated carbon fiber electrodes may already provide a good alternative to traditional silicon electrodes in terms of neuronal yield for multi-month neuroscience animal studies.

There is a large shift in electrode design specifications between short-term neuroscience experiments and long-term clinical implants. Our work points to a degradation of the polymer-based PEDOT:pTS coating when immersed in a heated saline environment, both on the benchtop and *in vivo*. This degradation was initially seen by a substantial increase in 1 kHz impedance and further confirmed by a visible lack of PEDOT:pTS coating. Additionally, we found a decrease in sulfur composition in the PEDOT:pTS coating after an accelerated soak test(figure3), a common result of PEDOT:pSS decomposition in heated, moist environments [122]. Previous work exploring the decohesion rate of PEDOT:PSS demonstrated the highly sensitive nature of the polymer to both increased moisture content and temperature [122]. This suggests that degradation of PEDOT:pTS is driving impedance increases across weeks and months.

Degradation of the electrode material is an unacceptable failure mode in a clinical BMI. Notably, our recording system with high input impedance amplifiers was able to record units with a 3 MΩ electrode, but this is not ideal for all applications. The O_2P treatment lowers the impedance into a range suitable for our recording system, but increasing the strength of the plasma bombardment may increase surface roughness and slow the impedance increase during experimentation. The PtIr coating tested here fared much better than PEDOT:pTS in accelerated soak tests, despite the mechanical detachment of PtIr on some fibers. This PtIr coating has shown promising *in vivo* results when deposited on PtIr microwire arrays [112], indicating that increasing the surface roughness of carbon prior to PtIr electrodeposition may increase coating adherence. Similar results may also be achieved with sputtered [119] or electrodeposited iridium oxide [123], [124]. It may also be possible to maximize the highly biocompatible nature of carbon [125] and use carbon-based coatings, such as two dimensional Ti_3C_2 MXene [126] or carbon-nanotube doped PEDOT [127], [128]. With greater improvements in device manufacturing, carbon fibers

electrodes may ultimately provide the means to create a stable, high density interface to the nervous system.

Chapter 3: Sharpened and Mechanically Durable Carbon Fiber Electrode Arrays for Neural Recording

A version of this chapter has been accepted for publication in IEEE Transaction on Neural Systems and Rehabilitation Engineering.

Elissa J. Welle, Joshua E. Woods, Ahmad A. Jiman, Julianna M. Richie, Elizabeth C. Bottorff, Zhonghua Ouyang, John P. Seymour, Paras R. Patel, Tim M. Bruns, and Cynthia A. Chestek

3.1 Abstract

Bioelectric medicine treatments target disorders of the nervous system unresponsive to pharmacological methods. While current stimulation paradigms effectively treat many disorders, the underlying mechanisms are relatively unknown, and current neuroscience recording electrodes are often limited in their specificity to gross averages across many neurons or axons. Here, we develop a novel, durable carbon fiber electrode array adaptable to many neural structures for precise neural recording. Carbon fibers (6.8 µm diameter) were sharpened using a reproducible blowtorch method that uses the reflection of fibers against the surface of a water bath. The arrays were developed by partially embedding carbon fibers in medical-grade silicone to improve durability. We recorded acute spontaneous electrophysiology from the rat cervical vagus nerve (CVN), feline dorsal root ganglia (DRG), and rat brain. Blowtorching resulted in fibers of 72.3 ± 33.5 degree tip angle with 146.8 ± 17.7 µm exposed carbon. Observable neural clusters were recorded using sharpened carbon fiber electrodes from rat CVN (41.8 μV_{pp}), feline DRG (101.1 μV_{pp}), and rat brain (80.7 μV_{pp}). Recordings from the feline DRG included physiologically relevant signals from increased bladder pressure and cutaneous brushing. These results suggest that this carbon fiber array is a uniquely durable and adaptable neural recording device. In the

future, this device may be useful as a bioelectric medicine tool for diagnosis and closed-loop neural control of therapeutic treatments and monitoring systems.

3.2 Introduction

Bioelectric medicine therapies use electrical stimulation to treat disorders of the nervous system [11]. Well-established uses of bioelectric medicines include sacral nerve stimulation for bladder diseases [129], cervical vagus nerve (CVN) stimulation for epilepsy [130], and deep brain stimulation for Parkinson's disease [131]. More recently, CVN stimulation has been used to treat inflammation [132] and therapy-resistant depression [25]. In order to precisely modulate the function of target organs, devices incorporate unique electrode configurations, materials, stimulation patterns, and closed-loop control [23], [24]. Current electrode interfaces for neural stimulation are large extraneural leads [133] or nerve cuffs [134], [135]. These interfaces are generally effective for stimulation but are limited in selectivity, often leading to side effects [136]. Furthermore, these interfaces have minimal utility for monitoring neural signals, which requires specific, multi-channel recording of the nerve or target organ. Current open-loop bioelectric medicine therapies may increase in efficacy if recording devices delineate the mechanisms of organ control or obtain organ-state signals.

Towards that end, intraneural interfaces offer greater recording signal-to-noise ratio and stimulation selectivity than extraneural interfaces [9], [44]. Clinical intraneural interfaces include the Utah Slanted Electrode Array (USEA) [35], [137] and the longitudinal and transverse intrafascicular electrode arrays [50], [138], [139]. The selective access to axons and fascicles enabled by conventional intraneural interfaces has facilitated clinical research of nerve-machine interfaces [33], which connect peripheral nerves to an external robotic device, allowing the nervous system to send motor commands to [140], and receive sensory input from the device [141].

However current interfaces have limited long-term viability due to electrode material failure [4], [142] and significant scarring [32], [41]. Additionally, their size (2–4 mm footprint for the USEA) [41] is not appropriate for the small nerves of the autonomic nervous system (0.3–0.5 mm diameter), which provide primary organ innervation. An ideal interface with autonomic nerves would maximize recording specificity while minimizing scarring, maintain a high channel count of small-footprint electrodes, and contain durable, biocompatible electrode materials.

Some recent interfaces are nearing these design criteria. Novel electrode development often starts with cortical applications that may later undergo translation to peripheral target locations. An injectable mesh-style SU-8 array with 10 μm-diameter elements prompted minimal histological scarring and maintained long-term recording in the brain [54]. However, the injection method of insertion would be difficult to use in peripheral applications. Flexible carbon nanotube "yarn" electrodes recently demonstrated physiologically-relevant recordings in the rat CVN and glossopharyngeal nerves for up to 16 weeks with minimal scarring [55]. This suggests that ultra-small electrodes may be similarly biocompatible with nerves, as has been shown in the brain [5], [48], [62]. While capable of recording from awake animals, the fragile "yarn" material and manual insertion of each electrode with a shuttle or suture may limited the channel count of this design [56].

Neural interfaces constructed of rigid components at micron size scale may ease surgical implementation while still minimizing tissue response. A novel design uses carbon fiber electrodes, which have been primarily used for brain recordings [6], [61], [102], as a method to record from nerves [63]. The carbon fiber electrodes reported in Gillis et al., 2017 successfully recorded acute spontaneous spiking activity [63]. However, the majority of their recordings were evoked responses to electrical stimulation, which are not as indicative of chronic in-dwelling

performance as smaller-amplitude spontaneous neural signals. Additionally, the architecture of their array would be difficult to translate from acute to chronic implantation. The carbon fibers' rigid junction to the substrate provides a likely breakage point. An array with sub-cellular carbon fiber electrodes that is compatible with peripheral geometry and capable of spontaneous neural recording is needed for neural interfacing.

Here, we develop and demonstrate a carbon fiber array comprised of several novel components: sharpened carbon fibers (SCFs, 6.8 μm diameter), silicone-embedded carbon fibers, and a small (< 2 mm) device architecture. Our sharpening method exhibits the carbon fibers of smallest known length to be sharpened, making carbon fibers suitable for chronic interfacing with small diameter autonomic nerves. We also show that long, sharpened, individuated carbon fibers are capable of self-insertion to depths of the brain previously only reached with insertion assistance. Our *in vivo* tests of SCFs show insertion into neural structures of varying stiffness and depths. Our benchtop experiments test the durability of carbon fibers embedded in silicone and the capability to survive many repeated cycles of bending. This suggests that subcellular carbon fiber electrodes with a stress-relieving backplane are a suitable electrode material for chronic residence in peripheral structures. We test the unique components of the array in the rat CVN, feline dorsal root ganglia (DRG), and rat motor cortex. We demonstrate that SCF arrays record spontaneous and physiologically relevant neural clusters. Additionally, we verify that the small device architecture enables surgical handling while accessing neural structures of differing geometries. This work displays a versatile, unique set of capabilities for carbon fiber arrays in neural interfacing and indicates the potential for chronic use.

3.3 Methods

3.3.1 Fabrication of Carbon Fiber Flex Array

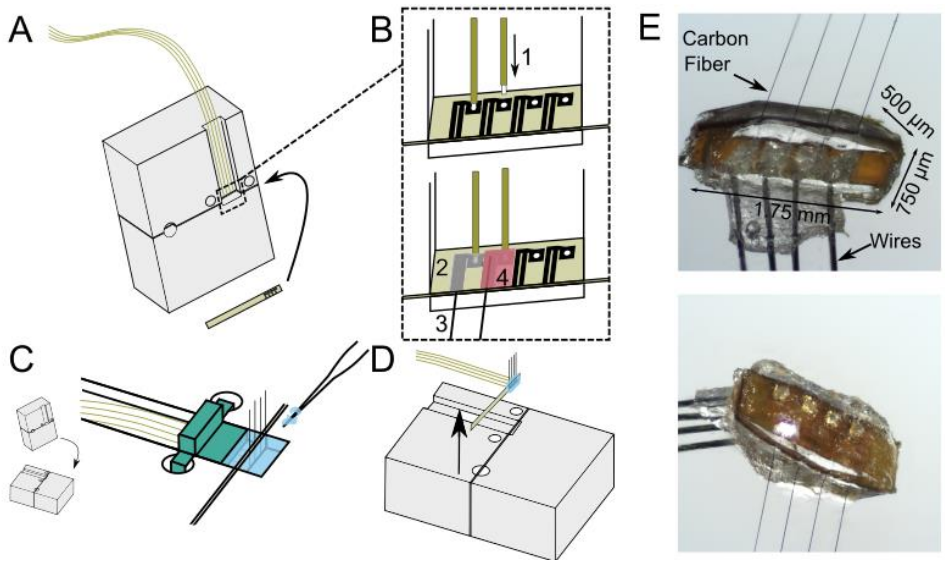

Figure 5 Fabrication steps of carbon fiber silicone array (CFSA). A) A custom polyimide PCB (gold) is slotted into a custom aluminum holder (grey) and four polyimide insulated wires (gold) are positioned above the area of interest on the polyimide PCB. B) The wires and carbon fibers are electrically connected and secured to the polyimide PCB. B1) The tip of each wire is exposed from polyimide insulation and placed into the gold plated vias in the polyimide PCB. B2) Silver epoxy is applied to the pair of connected gold traces and the adjoining gold plated via. B3) Bare carbon fibers are placed in the silver epoxy between the pair of gold traces, and then cured. B4) Insulating epoxy is applied over the electrical connections, and then cured. C) The aluminum holder is laid flat and a 3 D printed device (green) is placed over the wires to create a well for the silicone. Silicone (blue) is applied with pulled glass capillaries and then cured. D) The polyimide PCB with attached wires, carbon fibers, and silicone is lifted from the holder. E) Pictures of the CFSA with the excess tails of polyimide PCB removed, seen from the front (top) and back (bottom)..

Acute neural recordings from the rat CVN and feline DRG were collected using carbon fiber electrode arrays previously detailed in Patel et al., 2020 [8]. In this application, the carbon fibers were cut to 150–200 µm prior to sharpening.

3.3.2 Fabrication of Carbon Fiber Silicone Array (CFSA)

This study exhibits a novel carbon fiber silicone array (CFSA) featuring carbon fibers (6.8 µm diameter) partially embedded in silicone (Figure 5). The overall array size is 1.75 mm x 500 µm x 750 µm (length x width x thickness). The array is built on a custom polyimide PCB (MicroConnex, Snoqualmie, WA, USA), 450 µm x 6.81 mm x 50 µm in size. A 1.5 mm long exposed section of the PCB contains 4 pairs of 430 µm-long gold traces with 65 µm pitch that are positioned 310 µm apart (Figure 5B). Each trace pair is electrically connected to a 90 µm-diameter gold-plated via. During fabrication, the polyimide PCB is slotted into a custom aluminum holder (Figure 5A) (Protolabs, Maple Plain, MN, USA) and secured with tape.

A custom interface PCB was designed to interface with either a 32 or 16-channel Omnetics connector (A79024-001 or A79040-001, Omnetics, Minneapolis, MN, USA) and four 10 cm-long wires (50.8 μm diameter 35N LT, coated with polyimide to 60.9 μm, Fort Wayne Metals, Fort Wayne, IN, USA). The Omnetics connector and four wires were soldered to the interface PCB and secured with 2-part quick curing epoxy. The other wire end, with 75 μm uninsulated, was slotted into a gold-plated via in the polyimide PCB (Figure 5B-1). Silver epoxy was applied to the junction of the PCB and wire and the adjoining pair of gold traces (Figure 5B-2). Individual carbon fibers were placed in the silver epoxy between the paired gold traces (Figure 5B-3). After the silver epoxy was cured, a layer of insulating epoxy (353ND- T, Epoxy Technology, Inc., Billerica, MA, USA) was applied over traces and wire junctions and cured (Figure 5B-4).

A custom 3D-printed piece was attached to the aluminum holder to create a well around the CFSA for the silicone molding (Figure 5C). Pulled glass capillaries shuttled the degassed medical grade silicone (A-103, Factor II, Lakeside, AZ, USA) into the 200 μm-wide areas on either side of the polyimide PCB and across the sides between the fibers. The silicone was cured at 110° C for 20 minutes and the 3D printed wall was removed. The device was coated with approximately 800 nm of parylene-C (Specialty Coating Systems, Inc., Indianapolis, IN, USA). The polyimide PCB, with attached silicone, fibers, and wires, was removed from the aluminum holder with forceps (Figure 5D). Once removed, the carbon fibers were trimmed to length (500–1100 μm based on application) with microsurgical scissors prior to electrode tip processing (Figure 5E).

3.3.3 Sharpening of Carbon Fiber Electrode Tip

We adapted a heat-based sharpening method using a butane torch, seen in previous demonstrations of carbon fibers in long fiber bundles [102] or relatively long individuated fibers [63], to work with short individuated fibers (200–250 μm) suitable for dwelling within 300–500

μm-diameter nerves. Our method uses the reflective properties of water to precisely align short fibers with the water's surface for sharpening while the body of the array is kept safely under water (Figure 6).

Flex Arrays and CFSAs underwent a similar sharpening procedure using different holding mechanisms. The Flex Array was secured with putty to the base of a glass dish (Figure 6A). The water level was adjusted with a pipette until the array was completely submerged. The small, lightweight nature of the CFSAs required it be held by nerve forceps (ASSI.NHF0.5, Accurate Surgical & Scientific Instruments Corp., Westbury, NY, USA) during sharpening (Figure 6B). The tail of the CFSA was held at a 45 degree angle by forceps, which was secured to a stereotactic frame. The surface of the CFSA was parallel to the water surface with carbon fibers pointing up as it was lowered into the water until submerged. An endoscopic camera (MS100, Teslong, Shenzhen, China) aligned outside the glass dish was used to view the carbon fibers. The camera was tilted up beneath the water level to visualize the reflection of the fibers on the underside of the water surface. The water level was adjusted until fibers appeared to touch the reflection on the underside of the water surface (Figure 6A, B insets), at which point a microtorch (3 mm diameter flame, MT-51B, Master Appliance, Racine, WI, USA) was passed over the fibers for 10–20 s (Figure 6C). Sharpened carbon fibers (SCFs) were confirmed by visual inspection. Multiple passes of the microtorch were occasionally necessary.

3.3.4 Scanning Electron Microscopy (SEM) Imaging

Scanning electron microscopy (SEM) images were used to characterize SCFs. Images were collected in either a Nova Nanolab 200 DualBeam SEM (FEI, Hillsboro, OR, USA) or a MIRA3 SEM (Tescan Orsay Holding, Brno-Kohoutovice, Czech Republic). An accelerating voltage of 2 kV or 3 kV and a current of 0.21 nA or 24 pA was used on the Nova or MIRA3, respectively. Both

SEMs used an Everhart-Thornley detector for high-vacuum secondary electron imaging. Arrays were mounted on standard SEM pin stub mounts using carbon tape and gold sputtered for 60–120 seconds.

3.3.5 Electrochemical Deposition of Polymer Coating

To lower impedance, a solution of 0.01 M 3,4-ethylenedioxythiophene (483028, Sigma-Aldrich, St. Louis, MO, USA) and 0.1 M sodium p-toluenesulfonate (152536, Sigma-Aldrich, St. Louis, MO, USA) was electrodeposited onto the exposed carbon of the SCFs by applying 600 pA/channel for 600 s to form poly(3,4-ethylene-dioxythiophene):sodium p-toluenesulfonate (PEDOT:pTS) [5], [61].

3.3.6 Electrochemical Impedance Spectroscopy (EIS) and Cyclic Voltammetry (CV) Analysis

EIS and CV measurements were collected to characterize electrode fabrication steps and post-surgery viability. Three-electrode measurements were performed with a PGSTAT12 Autolab potentiostat (Metrohm / Eco Chemie, Utrecht, Netherlands) and vendor-supplied Nova software using the same setup and analysis methods described in Welle *et al*., 2020 [6]. Fibers were rinsed in deionized water after measurement.

3.3.7 Bend Testing of Silicone-Embedded Carbon Fibers

Carbon fibers were embedded in medical grade silicone to test their bending characteristics. Silicone was held in oval depressions milled into an aluminum baseplate (Protolabs, Maple Plain, MN, USA) and degassed in a vacuum chamber for 20 minutes at -0.09 MPa. Eight bare carbon fibers at a 152.4 µm pitch were aligned and submerged into silicone by 300–400 µm. After curing on a hotplate for 20 minutes at 110° C, the silicone-CF testing devices were gently removed with forceps. The silicone surface of some devices was slightly curved, but this was deemed

insignificant for our purposes. In a small number of experiments, CFSAs were tested to verify the amount of silicone needed above the edge of the polyimide PCB to exhibit the same properties as CFs embedded purely in silicone [143].

A 0.75 mm diameter glass capillary (M-235.5DD, PI, Auburn, MA, USA) attached to a linear actuator was repeatedly passed over the carbon fibers for bend testing. The glass capillary was 40–60 µm above the silicone surface and moved at a velocity of 17.09 mm/s and acceleration of 4.88 mm/s^2. One pass was the movement of the glass capillary from one end of the line of carbon fibers to another in a single direction. The percent of broken fibers on each device was collected at some combination of the experimental increments of 200, 1k, 2k, 6k, 8k, 10k, 20k, 30k, 40k, and 50k passes.

3.3.8 Animal Surgery

All animal procedures were approved by the University of Michigan Institutional Animal Care and Use Committee (PRO00009525). Electrophysiological recordings were collected from three locations in non-survival surgical procedures: rat CVN, feline DRG, and rat brain motor cortex. Prior to all surgeries, ground and reference wires (AGT05100, World Precision Instruments, Sarasota, FL, USA) were soldered to the interface PCB and the insulation was exposed up to 1 cm on the other end. The polyimide PCB tail was clamped by nerve forceps such that the fibers pointed away from the forceps toward down the cavity.

3.3.9 Acute Rat CVN Surgery

The non-survival CVN procedures were performed on male Sprague-Dawley rats (0.36–0.62 kg, Charles River Laboratories, Wilmington, MA, USA), as detailed in Jiman et al., 2020 (N=22 for companion study, +1 additional animal in current study), using Flex Arrays (150–250 µm length SCFs). Isoflurane (Fluriso, VetOne, Boise, ID, USA) was used for anesthetic induction

(5%) and maintenance (2–3%). Rats were placed on a heating pad and vitals were monitored. The CVN was accessed through a midline ventral cervical incision. Approximately 10 mm of CVN was isolated from the carotid artery and surrounding tissue. The CVN was lifted (~2 mm) on to a custom 3D-printed nerve-holder. The Flex Array was positioned over the elevated CVN using a 3-axis micromanipulator (KITE-R, World Precision Instruments, Sarasota, FL, USA) secured to an optical breadboard. The ground wire for the Flex Array was inserted subcutaneously in the cervical area and the reference wire was placed in the tissue of the cervical cavity. An endoscopic camera was aligned at the edge of the nerve-holder to visualize the carbon fibers during insertion. The heating pad and dissection microscopy were disconnected to reduce electrical noise. The nerve was rinsed with saline (0.9% NaCl, Baxter International, Inc., Deerfield, IL, USA) and the Flex Array carbon fibers were lowered and inserted into the CVN.

3.3.10 Acute Feline DRG Surgery

Three adult, domestic, short-hair male felines (4.0–5.6 kg, 1.3–1.4 years, Marshall BioResources, North Rose, NY, USA) were used for the DRG experiments with Flex Arrays (150–250 µm length SCFs). One feline (5.2 kg, 1.2 years) was used for the DRG experiment with a CFSA (375–475 µm length SCFs). Flex Arrays were previously used in CVN experiments. The animals were anesthetized with an intramuscular injection of ketamine (6.6 mg/kg), butorphanol (0.66 mg/kg), and dexmedetomidine (0.011 mg/kg). Animals were intubated and maintained on isoflurane (0.5–4%) and vitals were monitored (respiratory rate, heart rate, end-tidal CO_2, O_2, perfusion, temperature, and intra-arterial blood pressure). For fluid infusion and pressure monitoring, a 3.5 Fr dual-lumen catheter was inserted to the bladder through the urethra. A midline dorsal incision was made to expose the L7 to S3 vertebrae. A laminectomy was performed to access the S1–S2 DRG. After experimentation, animals were transitioned from isoflurane to

intravenous alpha-chloralose (70 mg/kg induction and 20 mg/kg maintenance) for the remainder of the experiment. Buprenorphine was provided subcutaneously every 8 to 12 hours as analgesia.

The Flex Array or CFSA was held in place with a clamp or nerve forceps and manually lowered into the surgical site using a micromanipulator. The ground wire was placed subcutaneously at a distant location and the reference wire was placed near the spinal nerve. Insertion into the S1 or S2 DRG was visualized with an endoscopic camera. After insertion, impedances were recorded at 1 kHz. Brushing trails with the Flex Arrays consisted of brushing of the scrotum with a cotton-tip applicator for 10 seconds following a period of no brushing for 10 seconds, for 60 seconds total. For bladder trials with the Flex Array, saline was infused into an empty bladder at 2 mL/min until either an elevated bladder pressure occurred, or urine leaking was observed. CFSA trials consisted of exploratory perineal brushing and baseline recordings.

3.3.11 Acute Rat Cortical Surgery

Four adult male Sprague Dawley rats (0.3–0.4 kg, Charles Rivers Laboratories, Wilmington, MA, USA) were used for the acute cortical experiments with CFSAs (75–1075 µm length SCFs). Two animals were excluded due to surgical complications unrelated to device features. Animals received carprofen (5 mg/kg) and were anesthetized with ketamine/xylazine (90/10 mg/kg) and maintained with ketamine (30 mg/kg). Rat vitals were monitored during surgery. Surgical preparation is detailed in Welle et al., 2020. A 2.5 mm by 2.5 mm craniotomy was drilled over the right hemisphere motor cortex. The CFSA was attached to a stereotactic manipulator and aligned over the craniotomy along the anterior-posterior axis. The ground and reference wires were wound around the grounding bone screw. A dural slit was made in the center of the craniotomy. The CFSA was manually lowered and the fibers were driven into the brain until the final target depth (0.775–1.180 mm) in layer V was reached [116].

3.3.12 Tip Electrophysiology Recording

Neural recordings from the rat CVN and feline DRG were collected using a Grapevine Neural Interface Processor (Ripple LLC, Salt Lake City, UT, USA). Electrophysiological signals were recorded at a sampling rate of 30 kHz. Impedances were measured during rat CVN experiments at 1 kHz in saline before the procedure and in the nerve immediately after insertion. Impedances were measured during the majority of feline DRG experiments at 1 kHz immediately after insertion. At least 5 minutes, 10 minutes, or 1 minute of recordings were obtained for the rat CVN, feline DRG bladder experiments, and feline DRG brushing experiments.

Brain electrophysiology recordings were collected using a ZC16 headstage, RA16PA pre-amplifier, and RX5 Pentusa base station (Tucker-Davis Technologies, Alachua, FL, USA). Data was sampled at a rate of 25 kHz, high pass filtered at 2.2 Hz, and anti-alias filtered at 7.5 kHz. Each recording session lasted at least 3 minutes.

3.3.13 Analysis of Neural Recordings

Principle component analysis of neural recordings was conducted in Offline Sorter (OFS, Plexon, Dallas, TX, USA) to isolate neural clusters. The electrophysiology signals were filtered with a band-pass filter at 300–10,000 Hz and manually thresholded below the noise floor. A trained operator manually identified neural clusters from the CVN and DRG recordings. Clusters from the brain were identified in OFS using the semi-automated method described in Welle et al., 2020. Sorted clusters were identified by unique amplitude, waveform shape, inter-spike interval, and response to physiological signals, such as breathing rate. MATLAB was used to analyze the sorted clusters. Firing rates of bladder clusters were calculated with a bin duration of 1 second and correlated to bladder pressure until the maximum bladder pressure [29]. The signal-to-noise ratio (SNR) was calculated using the mean peak-to-peak amplitude (V_{pp}) of a sorted cluster and the

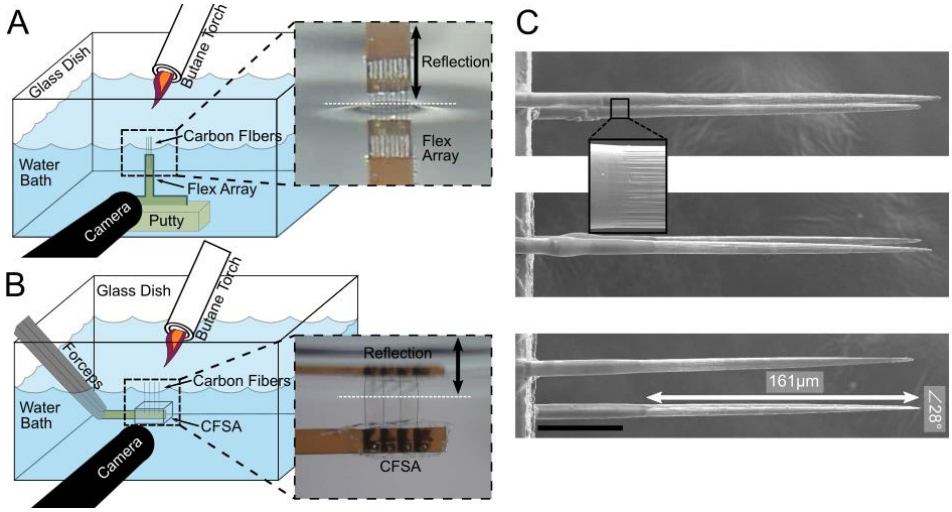

Figure 6 Blowtorch schematic and sharpened fibers. A) Flex Arrays are secured with putty to the water dish base. The water level is adjusted until the carbon fiber tips touch their reflection on the underside of the water surface (inset, black arrow denotes reflection). B) CFSAs are held with forceps and lowered into the water dish until the carbon fiber tips touch their reflection on the underside of the water surface (inset, black arrow denotes reflection). With both arrays, a pen camera located outside the water dish views the carbon fiber reflection under the water surface to confirm alignment at the water surface. A butane flame is passed over the water surface to sharpen the carbon fibers. C) Sharpened fibers have a smooth transition from p arylene C to bare carbon (inset). A representative SCF has 161 µm of carbon exposed from p arylene C (white arrow) and a tip angle of 28 degrees. Scale bar is 50 µm.

standard deviation of at least 500 ms of noise from the respective recording [SNR = V_{pp} / (2 * standard deviation of noise)]. When appropriate, values are presented as mean ± standard deviation (SD).

3.4 Results

3.4.1 Analysis of Sharpened Carbon Fibers

A blowtorch method for sharpening <500 µm linear carbon fiber arrays was developed to facilitate consistent insertion success in peripheral targets (Figure 6A, B). Example SCFs attached to Flex Arrays are shown in Figure 6C. Prior to blowtorching, carbon fibers were manually cut using microsurgical scissors to roughly 200 µm in length. After blowtorching, SEM analysis confirmed the average length of SCFs as 223.7 ± 18.9 µm (N=32 fibers). SCFs exhibited an average tip angle of 72.3 ± 33.5 degrees with a 146.8 ± 17.7 µm length of carbon exposed from parylene-C insulation, constituting an active recording site of 2734.5 ± 402.5 μm^2 surface area

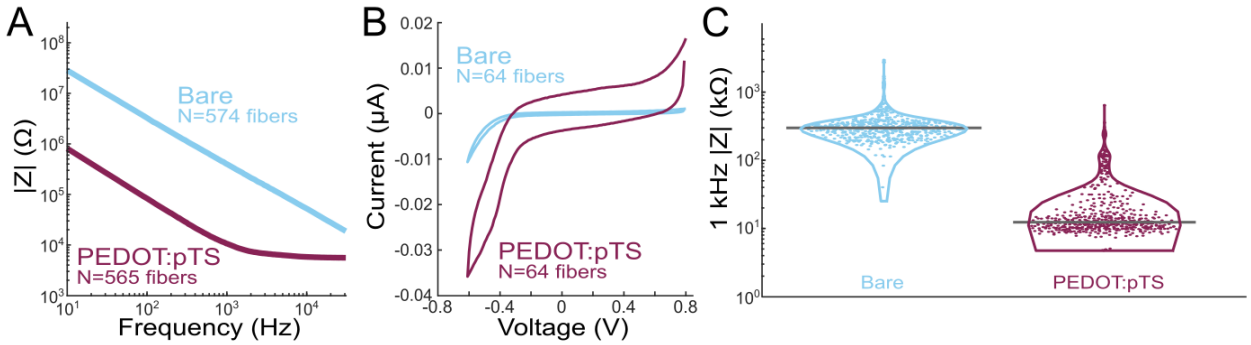

Figure 7 Electrochemical impedance spectroscopy and cyclic voltammetry analysis of SCFs. A) Impedance magnitude frequency spectrogram of bare SCFs (blue, N=574) and PEDOT:pTS coated SCFs (magenta, N=565). B) CV curves of bare (N=64) and PEDOT:pTS coated (N=64) SCFs. The cathodal charge storage capacity increased from 15.2 ± 5.4 µC/cm2 to 2 55.0 ± 148.6 µC/cm^2 once SCFs were coated with PEDOT:pTS . C) Violin plot of 1 kHz impedance magnitudes of bare (N=574) and PEDOT:pTS coated (N=565) SCFs. Mean 1 kHz impedance magnitude was 334.8 ± 243.2 kΩ and 32.3 ± 55.7 kΩ for bare and PEDOT:pTS coated SCFs.

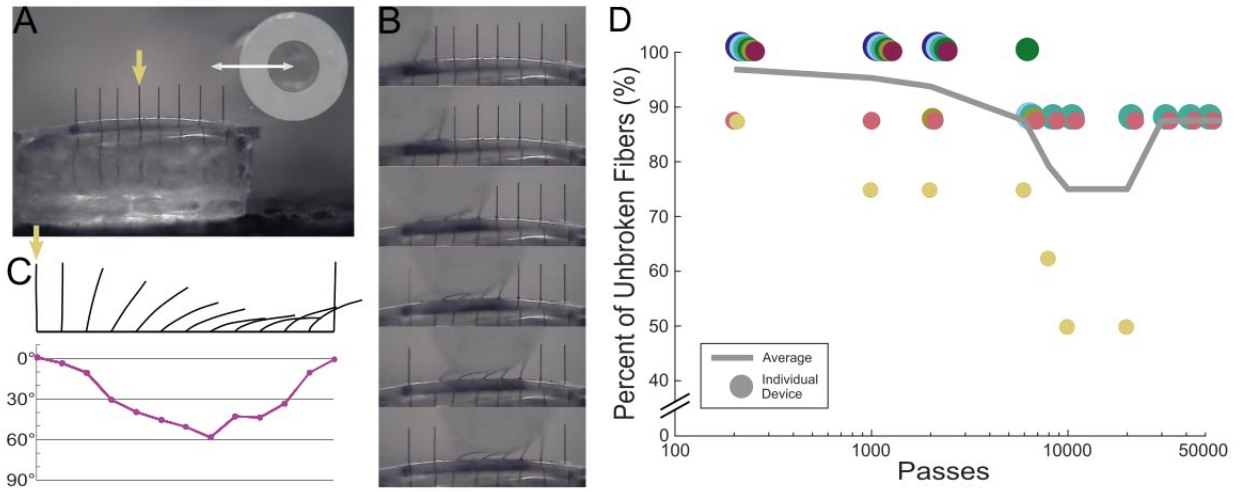

Figure 8 Bend test of silicone embedded carbon fibers. A) Bend test setup with a silicone carbon fiber testing device and a 0.75 mm diameter glass capillary (outlined in light grey). The glass capillary passes over the carbon fibers. A complete run from end to end counts as one pass. B) Still images of bent carbon fibers from a video shown in (A) during one pass. C) Top: Outlines of a single fiber, indicated in (A) by the yellow arrow, bending under the glass capillary. Bott om: Corresponding angle measurements from the outline of the fiber in each still image. On average, carbon fibers deflected 50.9 ± 6.2 degrees from the vertical position (N=23 fibers, 3 devices). D) Bend test data showing the percent of unbroken fibers plotted against the number of glass capillary passes. Each device contains 8 fibers and is shown as an individually colored circle. The average across all devices is shown as the solid line. After 50,000 passes, 87.5% of fibers remained unbroken.

(Figure 6C). The parylene-C transition between the exposed and insulated carbon appeared smooth on all imaged fibers (Figure 6C inset).

After sharpening, the electrodes were coated PEDOT:pTS [61]. The SCFs coated with PEDOT:pTS showed a large shift in impedance magnitude at lower frequencies (Figure 7A). SCFs of 200 µm length without PEDOT:pTS coating exhibited an average 1 kHz impedance ($|Z|_{1kHz}$) of

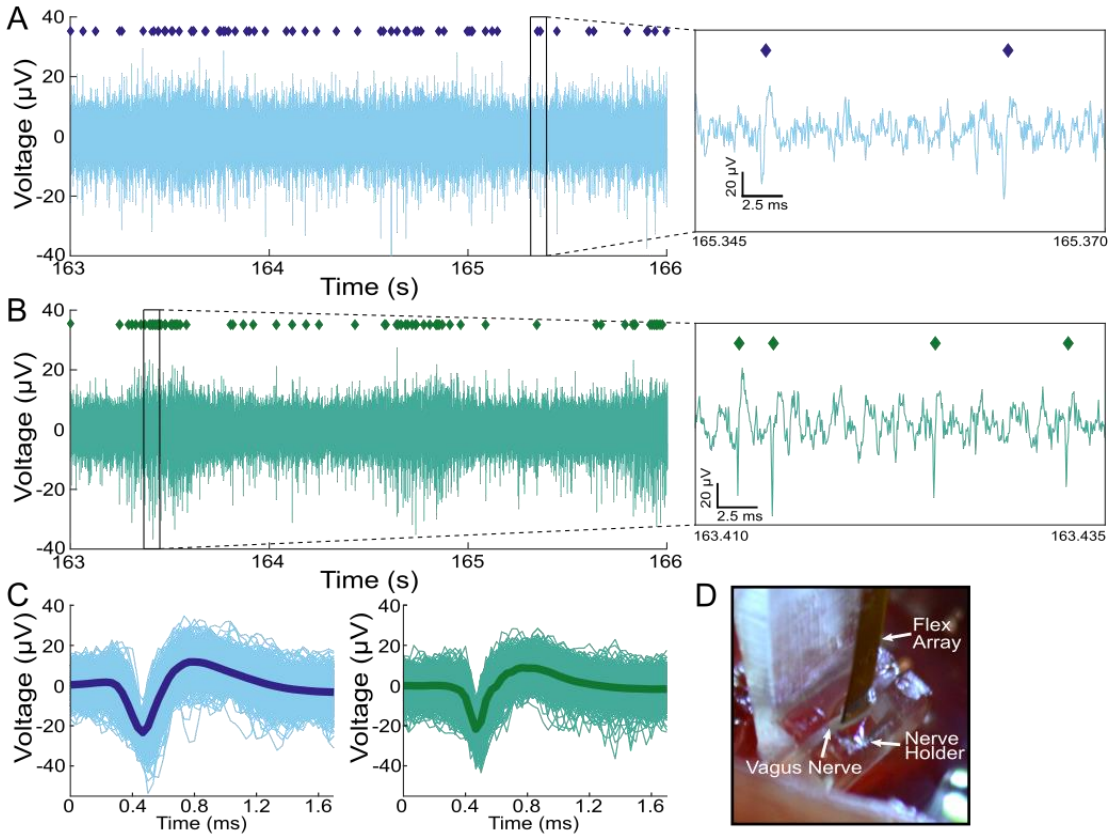

Figure 7 Neural activity recorded from a rat CVN with SCFs on a Flex Array. This is representative of the data set in Jiman et al., 2020. A and B) Three seconds of filtered data recorded on two SCFs. An inset of each raw trace shows 25 μs of data. C) Corresponding neural cluster indicated in (A), left, and (B), right, by diamond markers. The cluster in (A) has a mean Vpp=139.9 ± 26.4 μV. The cluster in (B) has a mean Vpp=122.8 ± 24.3 μV. D) Surgical setup showing the CVN lifted by the nerve holder with the Flex Array aligned above it.

334.8 ± 243.2 kΩ and a median $|Z|_{1kHz}$ of 298.6 kΩ (N=574 fibers). Once coated with PEDOT:pTS, SCFs exhibited an average $|Z|_{1kHz}$ of 32.3 ± 55.7 kΩ and a median $|Z|_{1kHz}$ of 12.4 kΩ (N=565 fibers) (Figure 7B). Therefore, coating the active SCF recording site with PEDOT:pTS contributed to a 90% decrease in average $|Z|_{1kHz}$ (Figure 7B). Correspondingly, the cathodal charge storage capacity of SCFs increased from 15.2 ± 5.4 μC/cm^2 to 255.0 ± 148.6 μC/cm^2 (N=64 fibers), calculated at a sweep rate of 1 V/s, after PEDOT:pTS deposition (Figure 7C).

3.4.2 Durability Testing of Silicone-Embedded Carbon Fibers

We harnessed the intrinsic compliance of carbon fibers through partial embedding in medical grade silicone [5], [143] to relieve strain at the SCF-polyimide PCB junction, therefore minimizing the eventual breakage seen on Flex Arrays after repeated insertions. Bend tests were

conducted on silicone-embedded carbon fibers, with and without attachment to an embedded polyimide PCB, using a 0.75 mm diameter glass capillary (Figure 8A, C). On average, carbon fibers deflected 50.9 ± 6.2 degrees from the vertical position (N=23 fibers, 3 devices), representatively shown in Figure 8B. The maximum measured fiber deflection from vertical without fracture was 71.6 degrees. We observed that an average of 93.8% fibers (N=58/62) did not break after 2,000 bends (passes of the capillary) during continuous fatigue testing (Figure 8D). After 50,000 passes, 87.5% of fibers remained unbroken (N=14/16). This durability was similarly observed on carbon fibers embedded in at least 150 µm of silicone when attached to an embedded polyimide PCB (Woods et al., 2020).

3.4.3 Acute Electrophysiology Recordings from Rat CVN

We tested the ability of SCFs to insert into and record from small diameter (300–500 µm) rat CVN. Six Flex Arrays with SCFs of 200–250 µm length, as represented in Figure 5C, were inserted into the left CVN of 22 Sprague-Dawley rats (Figure 9E). Detailed characterization of the population recordings is presented in a companion study by Jiman *et al.* 2020 [144]. In all experiments, we visually observed successful insertion of all SCFs into the CVN after an average of 2.3 insertion attempts. The functional SCFs (defined as $|Z|_{1kHz} < 1$ MΩ) had an average $|Z|_{1kHz}$ of 70.8 ± 81.9 kΩ once inserted into the CVN (N=326 fibers). Neural activity was recorded on 51.2% of the functional SCFs. Manual sorting and a mixture of Gaussians sorting methods were applied in principal component space to classify neural activity into clusters of distinct bipolar waveform shapes. Across the 326 functional SCFs, 174 sorted neural clusters were detected. The neural clusters had a mean V_{pp} of 30.7 ± 11.43 µV and a mean SNR of 3.52 ± 1.0. We observed that 19.8% of functional SCFs recorded neural clusters with SNRs > 4. The maximum mean V_{pp} was found to be 91.72 µV.

Representative electrophysiological recordings of spontaneous CVN activity are shown in Figure 9. Sixteen SCFs were determined functional and had an average $|Z|_{1kHz}$ of 25.3 ± 10.9 kΩ after insertion into the CVN. Sorting analysis identified neural clusters on 3 of 16 functional SCFs in this example experiment. Neural data from 2 functional SCFs are shown in Figure 9A and C. The corresponding neural cluster from each functional SCF had a mean V_{pp} of 139.9 ± 26.4 µV and 122.8 ± 24.3 µV (Figure 9B, D). Across all 3 SCFs, we found that the waveform V_{pp} of clusters ranged from 18.5 µV to 108.5 µV. The sorted neural clusters had a mean V_{pp} of 41.8 ± 6.8 µV and an average median V_{pp} of 41.0 µV. Clusters from this representative experiment had a mean SNR of 4.1 ± 0.08.

3.4.4 Acute Electrophysiology Recordings from Feline DRG

We sought to discover whether it is possible to insert SCFs of short length (150–250 µm) into feline DRG with minimal external force during insertion. We inserted 16-channel Flex Arrays with 150–250 µm length SCFs into the S1 DRG of 3 felines (Figure 10A, B) and a 4-channel CFSA with 375–475 µm length SCFs into the S2 DRG of 1 feline (Figure 11A, B). In each experiment, the array was manually lowered with a micromanipulator until SCFs were visually inserted in tissue. Functional SCFs ($|Z|_{1kHz}$ < 1 MΩ) had an average $|Z|_{1kHz}$ of 26.9 ± 7.4 kΩ in the DRG immediately after insertion (N=30 fibers). Despite the large recording surface area, neural clusters were observed on 32 of 52 total inserted SCFs (N=4 felines; 3 Flex Arrays; 1 CFSA), and 27 of 30 functional ($|Z|_{1kHz}$ < 100 kΩ) SCFs (N=3 felines; 2 Flex Arrays; 1 CFSA). Impedance data was not recorded on one feline and excluded from the functional SCF count. Our offline sorting analysis of recorded neural activity identified 73 neural clusters across all feline

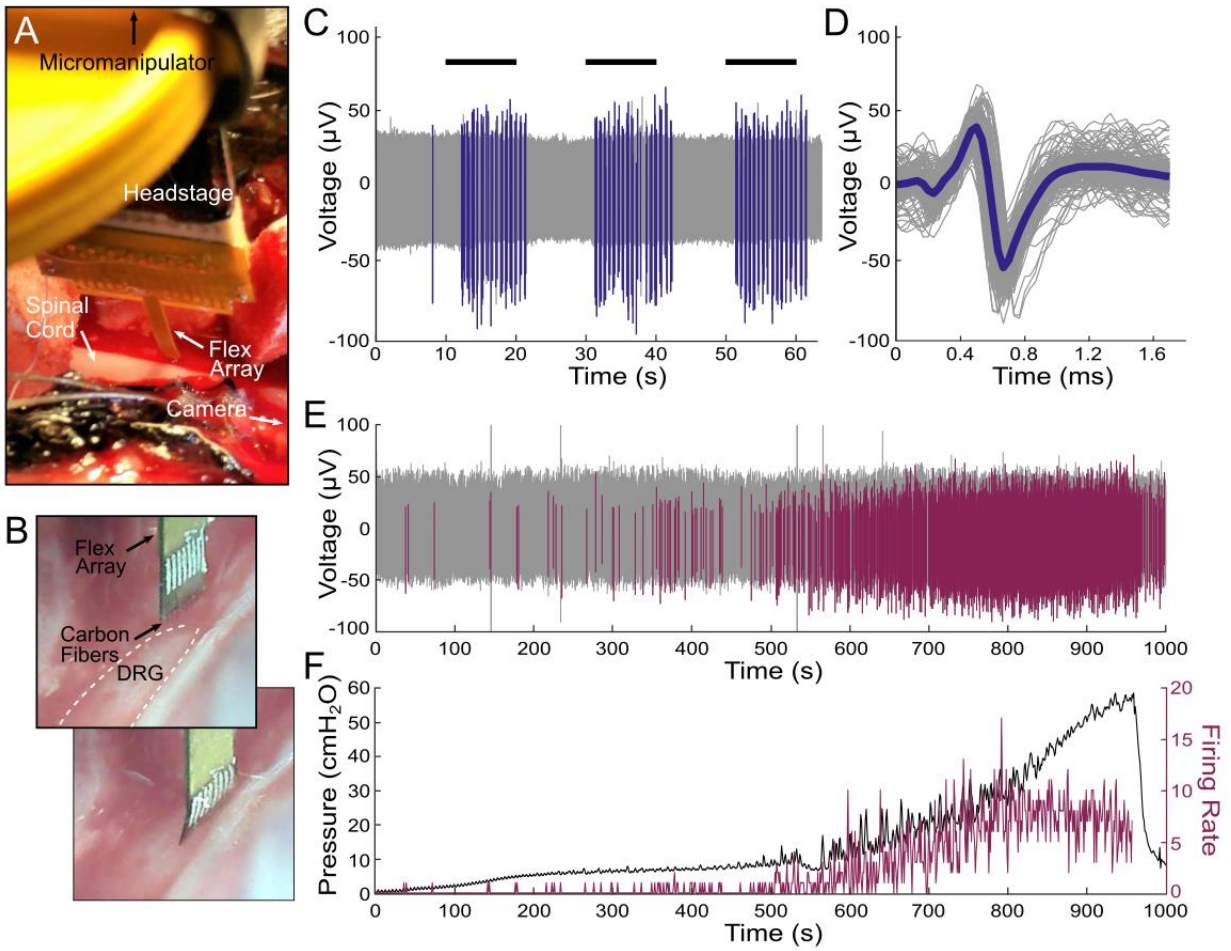

Figure 8 Flex Array experiments in feline DRG. A) Surgical setup showing the Flex Array connected to a headstage lowered to the DRG with a micromanipulator. The DRG is located above the spinal cord and the camera is positioned parallel to the DRG to the. B) Flex Array as seen by the camera before (top) and after (bottom) insertion into the DRG (white dashed lined). C) Neural waveforms in response to scrotal brushing (horizontal b lack lines) highlighted in blue. D) The brushing cluster from (C) with mean waveform shown by thick blue line (mean Vpp=108.7 ± 11.0 μV, SNR=6.0). E) Neural waveforms associated with bladder filling are colored purple. F) Bladder pressure (left axis) and firing rate (right axis) of bladder cluster in (E), with correlation coefficient of 0.83.

experiments with an average of 1.8 ± 0.9 clusters per SCF. Clusters were classified as either spontaneous or driven. Spontaneous neural activity was sorted into clusters associated with breathing (breathing clusters), clusters unlinked to obvious physiological signal (spontaneous clusters, Figure 11C), and clusters containing multiple units (multi-unit clusters). Driven clusters responded to the experimental variables of perineal or scrotal brushing (brushing clusters, Figure 10C, D) or saline-infusion of the bladder (bladder clusters, Figure 11E, F). Across all experiments,

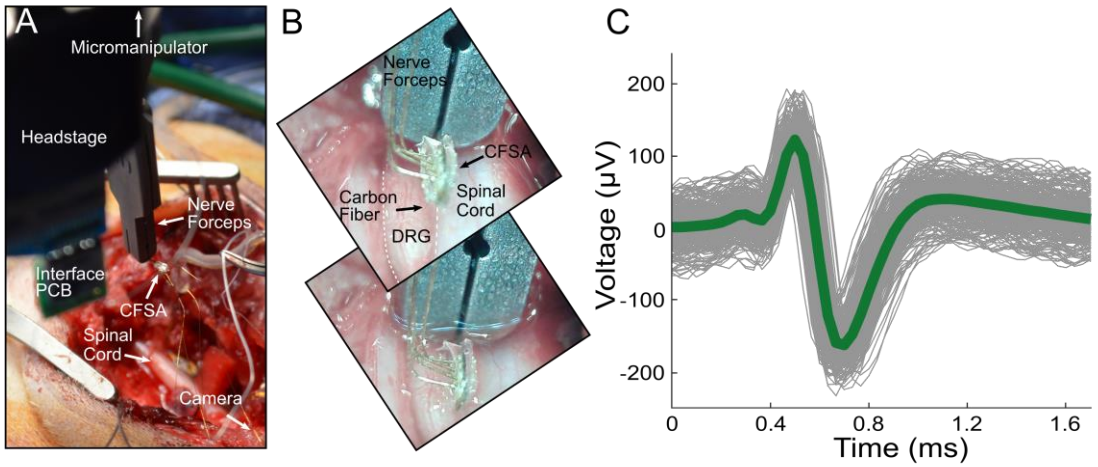

Figure 9 CFSA experiment in feline DRG. A) Surgical setup showing the CFSA, held by nerve forceps, and interface PCB connected to a headstage lowered to the DRG with micromanipulator. The DRG is located below the visible spinal cord. The camera is positioned parallel to the spinal cord to the right of the surgical cavity. B) CFSA, held by nerve forceps, as seen by the camera before (top) and after (bottom) insertion into the DRG (white dashed line). C) Spontaneous neural cluster and mean waveform shape (green line) recorded in the DRG with the CFSA (mean Vpp= 298.8 ± 15.5 µV, SNR=6.5).

we classified 16.2% of clusters as breathing, 43.2% as spontaneous, and 16.2% as multi-unit, 14.9% as brushing, and 9.5% as bladder clusters.

Breathing clusters depicted rising and falling amplitudes, in addition to bursting patterns. We believe the observed changes in amplitude were likely due to micromotion shifts in SCF position with respect to the neuron as the animal's body shifted slightly with each breath. The V_{pp} of breathing clusters ranged from 41.4 µV to 186.7 µV, with a mean V_{pp} of 84.4 ± 16.8 µV and a mean SNR of 7.0 ± 3.7 (N=12 clusters; 3 Flex Arrays). Spontaneous clusters did not obviously track with breathing or other physiological signals. The mean V_{pp} of spontaneous clusters was 115.9 ± 16.6 µV and a mean SNR of 7.9 ± 6.0 (N=32 clusters; 3 Flex Arrays; 1 CFSA). Figure 11C shows an example spontaneous cluster recorded from the CFSA with a mean V_{pp} of 298.8 ± 15.5 µV and SNR of 6.5. Multi-unit clusters contained clear neural activity, but we were unable to differentiate spontaneous clusters. Multi-unit clusters had a mean V_{pp} of 34.2 ± 6.3 µV and a mean SNR of 4.7 ± 1.2 (N=12 clusters; 1 Flex Array).

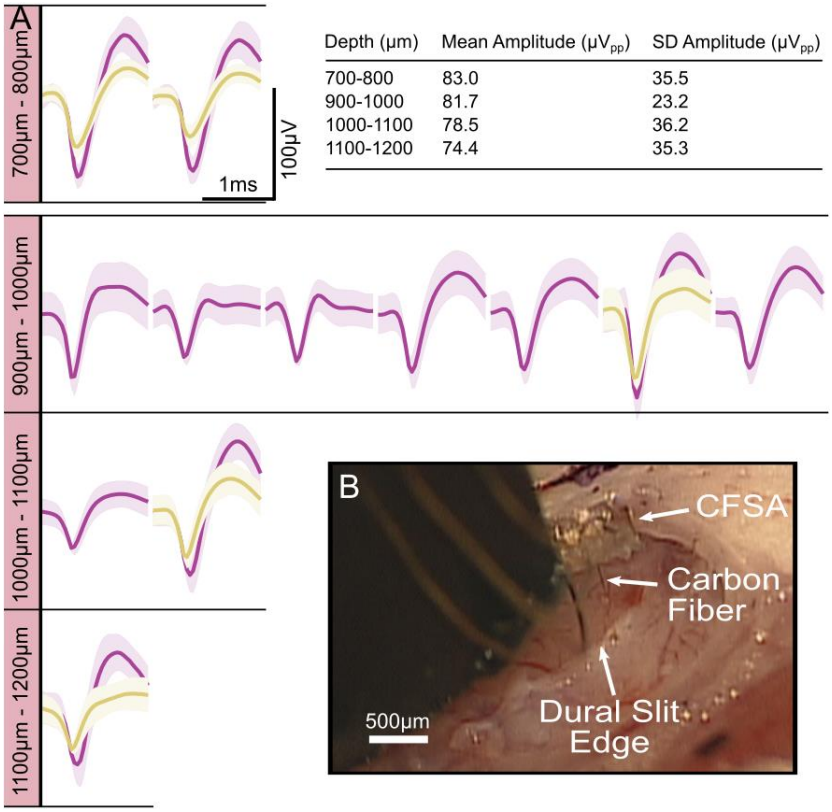

Depth (µm)	Mean Amplitude (μV_{pp})	SD Amplitude (μV_{pp})
700-800	83.0	35.5
900-1000	81.7	23.2
1000-1100	78.5	36.2
1100-1200	74.4	35.3

Figure 10 Electrophysiology recorded from SCFs on CFSAs in the rat motor cortex. A) Neural units recorded at varying depth increments. The units were recorded on six SCFs across three devices during seven independent insertions into the brain. Each unit, or overlapping units, was recorded from a single SCF during one insertion. The inset table shows a summary of the mean amplitude and standard deviation of neural unit s at each depth. B) Surgical setup of CFSA insertion into the brain through the dural slit.

To further verify that spikes were neural in origin, we recorded neural activity in response to cutaneous brushing and bladder filling. In 2 of 3 experiments with Flex Arrays recording from the S1 DRG, we recorded neural activity corresponding to the cutaneous response to scrotal brushing. We observed 10 clusters on 8 SCFs with bursting activity during the 10 second brushing intervals (Figure 10C). The corresponding brushing cluster, shown in Figure 10D, has a mean V_{pp} of 108.7 ± 11.0 µV and SNR of 6.0. The mean V_{pp} of all brushing clusters was 152.4 ± 13.5 µV and the mean SNR was 7.1 ± 4.5 (N=10 clusters; 2 Flex Arrays). We also recorded a single brushing cluster in response to perineal brushing on a CFSA in one experiment. The mean V_{pp} of the cluster was 219.5 ± 54.1 µV and the mean SNR was 18.9 (N=1 cluster; 1 CFSA)

We also observed neural activity that contained physiologically relevant signals of bladder pressure in response to bladder filling. Across all experiments, the firing rates of 7 neural clusters were found to correlate with bladder pressure during the bladder filling procedure. A representative bladder cluster is shown in Figure 10E and 10F. Correlation coefficients between bladder pressure and firing rate were calculated for each bladder cluster. The correlation coefficients were between 0.23 and 0.82, with a median of 0.70. The mean correlation coefficient of the 7 clusters with their respective bladder pressure was 0.61 ± 0.21. The V_{pp} of the bladder clusters were between 32.1 µV and 190.4 µV, with a mean V_{pp} of 86.8 ± 14.1 µV and a mean SNR of 10.3 ± 6.3 (N=7 clusters, 3 Flex Arrays).

We observed that several clusters recorded on the Flex Array appeared on multiple adjacent SCFs. These units fulfilled our metrics for being a sortable cluster in terms of amplitude, signal width, and inter-spike-interval, but appeared concurrently on multiple consecutive channels. In one instance, a breathing cluster was seen on four SCFs in a 2 x 2 geometry on a Flex Array, spanning a distance of 141 µm between diagonal SCFs.

3.4.5 Acute Electrophysiology Recordings from Rat Cortex

SCFs on CFSAs of length 750 µm to 1075 µm were found to self-insert into dura-free brain tissue from depths of 775 µm to 1180 µm (Figure 12B). In total, 17 sortable single units were recorded from 6 SCFs across 3 devices during 7 independent insertions into the brain (Figure 12A). The mean V_{pp} was found to decrease as cortical depth increased (Figure 12 table). The overall mean V_{pp} was 80.7 ± 27.5 µV and the largest recorded unit amplitude was 126 µV.

3.5 Discussion

Here, we demonstrate the capabilities of SCF arrays for interfacing with the central and peripheral nervous systems. This work represents, to our knowledge, the first stiff, penetrating, sub-cellular electrode array with a durable, stress-relieving backplane.

SCFs easily penetrate into multiple neural structures of varying stiffness and geometry. Initial insertion attempts in the small diameter (300–500 µm) rat CVN with conventional blunt-tipped carbon fiber electrodes [6] yielded unsuccessful insertion, and surgeons often resorted to slitting the epineurium. However, short (< 250 µm) SCFs consistently inserted into the CVN. Successful insertion was also achieved in the feline DRG, which has a thick epineurium layer of 50–100 µm [145], [146], without the assistance of the pneumatic inserter [137]. In the brain, blunt-tipped carbon fibers previously relied upon insertion assistors, such as temporary stiffening agents or a silicon backbone, to insert into dura-free brain at lengths greater than 500 µm [6], [61]. Despite a 6.8 µm diameter, SCFs inserted without assistance into brain at lengths of 1075 µm.

Silicone-embedded carbon fibers survived repeated bending, indicating a potential for robust surgical handling unlike what is often seen for silicon, glass-encapsulated, or other metal penetrating electrodes [143]. Slight instrument adjustments in the surgical space often translated into large movements at the Flex Array–nerve interface, extreme enough for total carbon fiber breakage if not mitigated by an experienced surgeon. Biological motion surrounding peripheral nerve interfaces is likely more significant to intraneural electrode breakage than brain motion is for chronic penetrating brain electrodes. This array demonstrates a capability to withstand the long-term fatigue that a peripheral interface is likely to experience by harnessing the intrinsic compliance of carbon fibers.

The blowtorch sharpening of carbon fibers resulted in a low-impedance electrode well within relevant electrophysiology recording range [92]. While SCFs had a 10.6 times larger surface

area than laser cut carbon fibers (2735 μm^2, 257 μm^2, respectively) from Welle et al., 2020, blowtorching resulted in only a 1.7 times increase in 1 kHz impedance (32 kΩ , 19 kΩ, respectively). Despite the low 1 kHz impedance, it was unclear if the larger surface area would affect recording ability. We looked to similar devices to indicate the impact of a large surface area, such as the carbon nanotube yarn electrode. The yarn electrode recorded neural clusters from small autonomic nerves with electrodes exhibiting both a larger diameter (10–20 µm) and larger exposed length (200–500 µm), resulting in a larger surface area electrode [55], [56].

In fact, we recorded clear neural clusters with SCFs in rat CVN, feline DRG, and rat cortex. The amplitudes of neural clusters recorded from small, myelinated A fibers and unmyelinated C fibers within the rat CVN were predictably often lower than those recorded from cell bodies and axons within the feline DRG or rat cortex. The mean amplitudes of spontaneous neural clusters from the rat CVN, feline DRG, and rat cortex were 41.8 µV, 115.9 µV, and 80.7 µV, respectively. In addition to spontaneous activity, we recorded neural activity from the feline DRG corresponding to cutaneous brushing (152.4 ± 13.5 µV) and bladder pressure (86.8 ± 14.1 µV). The bladder clusters correlated to bladder pressure with a mean correlation coefficient of 0.61. This encouraging preliminary work, although not exhaustive, is the first example of carbon fiber electrode recordings in feline DRG, to our knowledge.

Novel, miniature, and implantable devices are required as bioelectric medicines advances in precise deciphering and monitoring of neural signals [11], [24]. The neural interface presented here could benefit a broad range of medical applications, such as control of hypertension [147], or monitoring of the digestive system [148] or cytokines [149]. Recording high quality, single units may improve the precision of these medical applications, especially with the CVN [30]. Due to their small diameter, carbon electrodes are more likely to land closer to regions of high electric

field potential. This may lower stimulation thresholds below those used by other larger intraneural interfaces [150]. Promising preliminary stimulation results in other studies [63] enhance the prospect for this array in clinical peripheral nerve applications.

The array presented here uses stable, biocompatible materials appropriate for clinical use, such as carbon fiber [151] and medical-grade elastomer. Metal coatings traditionally used in medical devices, such as platinum iridium or iridium oxide [112], [119], could replace PEDOT:pTS to increase long-term stability. The large surface area of bare carbon electrode is favorable for neurotransmitter sensing [8], [103]. With this larger surface area, we recorded neural units. However, the smaller amplitude of neural clusters from the rat cortex recorded here as compared to our previous studies may be due to the larger surface area [6], [92]. A smaller surface area electrode might be achieved by electrochemical etching [152].

Additionally, this array's architecture may enable interfacing with difficult to access locations or small autonomic structures [24]. The ability to insert individuated, sharpened fibers as an array without assistance may enable larger channel count arrays of small stiff electrodes [106], [153]. The ability to penetrate DRG suggests that these probes may be useful for other vertebrate ganglia, such as the nodose ganglia [154], [155], and invertebrate ganglia, such as those in Aplysia [156]. The mechanical durability in a soft substrate makes these arrays ideal candidates for long-term studies in large animal models [157], [158]. Additionally, carbon fiber and carbon composite electrodes previously demonstrated a minimal chronic scarring response in brain [5], [8] and nerve [55].

There are, however, difficulties in deploying these devices for large-scale use. The manual fabrication of the carbon fiber arrays is a time-intensive process for an experienced fabrication technician. The application of silicone is limited by the small movements necessary to place the

silicone in the wells and not on the fibers. The polyimide PCB and holder would likely require modifications to expand beyond four channels. While whole arrays can be sharpened at once – an improvement from the previous individual lasering technique [6] – the amount of exposed carbon can not yet be pre-determined. A chronic attachment method is still needed, such as suturing or Rose Bengal photochemical tissue bonding [159]. Future studies will need to investigate the chronic histological response of carbon fibers in peripheral structures.

3.6 Conclusion

This work examines novel mechanical improvements to carbon fiber electrode arrays for interfacing with the nervous systems. SCFs can penetrate stiff substrates, such as feline DRG and rat CVN, and reach deeper layers of the rat cortex, verifying their use with various recording targets despite their small diameter. The carbon fiber arrays embedded in silicone demonstrated durability beneficial for surgical handling and chronic peripheral nerve interfacing. Our electrophysiology recordings from the DRG were the first reported recordings with carbon fiber electrodes, to the best of our knowledge. The ease of insertion and durability to movement make these arrays potentially viable candidates for future chronic *in vivo* use.

Chapter 4: Utah Array Characterization and Histological Analysis of a Multi-Year Implant in Non-Human Primate Brain

Elissa J. Welle, Autumn J. Bullard, Hao Shen, Paras R. Patel, Ciara M. Caldwell, Alexis Vega-Medina, Joseph G. Letner, Julianna M. Richie, Parag G. Patil, Dawen Cai, and Cynthia A. Chestek

4.1 Introduction

Brain machine interfaces (BMIs) offer patients living with neurological conditions or injuries that inhibit movement or sensation the chance to restore what was lost [13], [140], [160]. BMI studies have shown patients controlling computer cursors or robotic hands with their thoughts [64], [161]. The Utah Electrode Array (UEA), the only intracortical recording device approved for clinical BMIs, records the neural signals from the brain in these studies [162]. The basic architecture of the UEA has remained constant over its lifetime of three decades [16]. It features a silicon body composed of 100 electrodes arranged in a 10 x 10 layout with 400 μm electrode pitch for a total size of 4 mm x 4 mm [17]. While the longest running human clinical study of a UEA lasted approximately 5.4 years [163], the majority of studies using UEAs report a decrease in the signal amplitude and channel count within the first few months to one year of implant [19], [20], [164]. Sophisticated decoding algorithms and amplifiers with low power and low noise can extract some information from the remaining channels [22], [87]. However, in order to achieve high performing BMIs, we need a high channel count recording system capable of detecting high fidelity neural signals.

The reduction in recorded neural signal quality and quantity may be due to multiple failure mechanisms including a decreased neuron density near the UEA, nearby scarring, and a

degradation of the UEA itself [165]. While it is difficult to analyze histological results of implanted UEAs in human or non-human primate (NHP) experiments, studies have analyzed the inflammatory markers and neuron health in feline or rodent models [166]–[170]. One study determined that the neuron density is substantially decreased within an approximately 200 μm radius from the surface of a silicon shank electrode [90], a distance that would affect the entire recording region between two adjacent shanks on the UEA [171]. This study, and several others, have found a collection of inflammatory cells, including activated astrocytes, macrophages, and microglia, forming a scar surrounding the silicon implant [39], [42], [43], [166], [172]. Inside the scar, there is a heightened level of reactive oxide species [40], which has been linked to the degradation of electrical devices [119]. This scaring also appears in the peripheral nerve [137]. After several months of implantation in one study, UEAs appears to have been pushed out of the tissue by an accumulation of a dense network of fibrotic tissue [36], [41], although other studies using smaller diameter silicon electrodes show less fibrotic encapsulation [35], [38], [173]. In other studies, UEAs explanted after several months in the cat or rat sciatic and femoral nerves showed parylene delamination, cracking, and thinning, as well as tip metal cracking [165], [174]. Due to the sensitive and important nature of studies involving NHPs, just one other group has examined both UEA degradation and histological impact of long term UEA implant in NHP cortex [19], [175]. Roughly 80% of UEAs failed completely during the length of the study, the majority of which failed within the first year of implant [19]. Explanted UEAs showed overall signs of degradation, and histology showed substantial inflammatory markers and neuron density decrease near electrode holes [175]. However, a quantification of neuronal density near electrode holes or a quantification of the types of electrode failures has yet to be published.

Here, we add to the collective knowledge of changes in neuronal density and UEA integrity after multi-year implantation in the cortex of a NHP. We analyze the neuron density surrounding UEAs implanted in the motor and sensory cortices in both the left and right hemispheres for 1.6 and 2.3 years, respectively. We compare the neuron density around electrode holes to nearby healthy tissue. Portions of this work were previously reported in Bullard, 2019, such as the tissue images and preliminary manually-counted neuron density metrics [176]. Here, we expand this effort to analyze the neuron density of all electrode holes in multiple slices using a semi-automated counting methodology. We also analyze images of the UEAs under scanning electron microscopy (SEM) to determine degradation in the electrode surface. This study furthers our understanding of the result of long term UEA implantation in the cortex of a NHP.

4.2 Methods

4.2.1 Experimental set-up

Four Utah electrode arrays (UEAs, Blackrock Microsystems, Salt Lake City, UT, USA) were implanted in the sensory and motor cortices of a rhesus macaque NHP (Figure 13). The NHP was trained for individual finger dexterity tasks using brain control [21], [177]. The NHP also underwent sensory percept experiments under anesthesia. After sacrificing the NHP, the UEAs were extracted, cleansed, imaged, and analyzed for damage. The brain tissue under the UEAs was sliced, stained, imaged, and analyzed for changes in neuron density.

4.2.2 UEA implantation

All animal procedures were approved by the University of Michigan Institutional Animal Care & Use Committee. UEAs were implanted in the primary motor (M1) and sensory (S1) cortex of the left hemisphere on August 20, 2015 (Figure 13A-C), and the right hemisphere on May 4, 2016 (Figure 13D, E). Each UEA was composed of 1.5 mm length electrode shanks in a 10 x 10

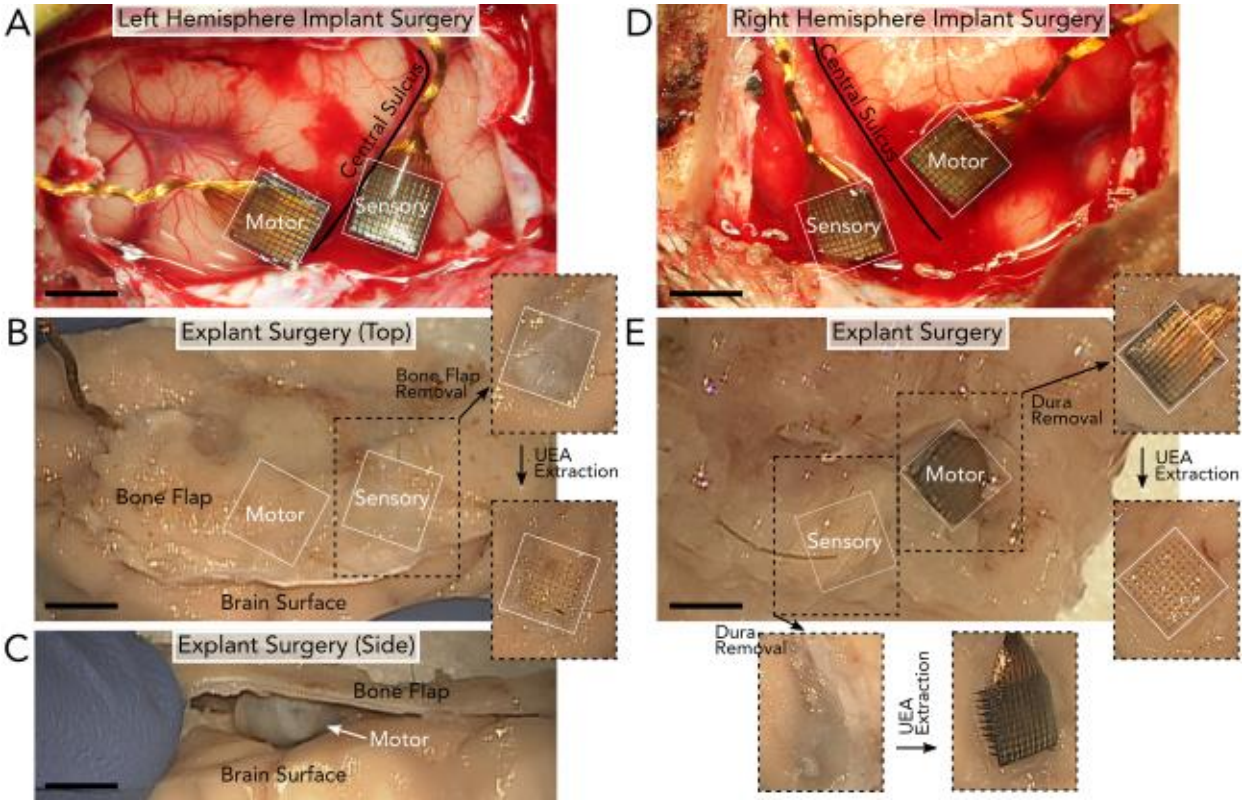

Figure 11 Surgical implantation and explantation of UEAs after 848 days in the left hemisphere (A-C) and 590 days in the right hemisphere (D-E) of the NHP. A) Left hemisphere surgical implantation of two UEAs in the motor and sensory cortices on either side of the central sulcus. B) Explantation of the UEAs in (A) involved removing the section of bone (bone flap) above the arrays. After the bone flap was removed, the UEAs could be extracted. Removing the left sensory UEA revealed clear holes in the tissue. C) However, the UEA in the left motor cortex was fully encapsulated by tissue and no longer implanted in the brain surface, as seen from the image taken of the side of the tissue. D) Right hemisphere surgical implantation of two UEAs in the motor and sensory cortices on either side of the central sulcus. E) Explantation of the UEAs in (D) involved removing the bone flap above the arrays to reveal the two UEAs. After the bone flap was removed, the UEAs could be extracted. Both UEAs were partially or fully implanted in the tissue at the time of explant. All scale bars are 4mm.

configuration with 400 µm pitch and a 6 cm length wire bundle. Three UEAs had iridium oxide coated electrode tips, except the right motor cortex UEA, which was coated with platinum. The UEAs in left and right sensory cortices were fabricated with an experimental aluminum oxide coating prior to parylene insulation [178].

For each surgical implantation, the NHP was placed in a stereotactic frame after induction with general anesthesia. The location of the craniotomy over the central sulcus was estimated using the stereotax. A craniotomy and durotomy were performed. The UEAs were positioned and then impacted into the cortical tissue using a pneumatic inserter (Blackrock Microsystems, Salt Lake City, UT, USA), seen in Figure 13A and 1D. The dura was closed over the UEAs and sealed with

PRECLUDE Pericardial Membrane (Gore, Flagstaff, AZ, USA) and DuraGen (Integra LifeSciences, Princeton, NJ, USA). The bone flap was replaced and fastened with titanium bone screws (DePuy Synthes, Paoli, PA, USA). Silicone elastomer (Kwik-Cast, World Precision Instruments, Sarasota, FL, USA) and dental acrylic (A-M Systems, Sequim, WA, USA) were applied to secure the wire bundles to the skull.

4.2.3 UEA and brain tissue extraction

All four UEAs were extracted on December 15, 2017 after 848 days of implantation in the left hemisphere (Figure 13B, C) and 590 days of implantation in the right hemisphere (Figure 13E). The terminal surgical extraction protocol required that perfusion not be performed under anesthesia, thus *ex vivo* perfusion began approximately 4 minutes after death, as confirmed by veterinarian staff. The NHP was anesthetized with ketamine and then sacrificed with euthanasia solution (VetOne, Boise, ID, USA). The NHP was transcardially perfused with 1X phosphate buffer saline (PBS) solution (BP3994, Fisher, Waltham, MA) with 10U heparin/mL until the exudate was clear, followed by approximately 1000 L 4% (w/v) paraformaldehyde (PFA) fixative (Electron Microscopy Sciences, Hatfield, PA, USA) in 1X PBS.

After perfusion, the dental acrylic and overlying bone flap were removed with a handheld drill. Dural growth on top of the UEAs was removed. The brain sections containing the UEAs were excised and placed in 4% PFA for 72 hours at 4 °C (Figure 13 B, E). At this point the UEAs were removed with fine forceps and immediately placed in a chemical disinfectant, Benz-All (Xttrium Laboratories, Inc., Mount Prospect, IL, USA), overnight. UEAs were switched to 1X PBS after approximately 24 hours to be preserved for future analysis. After UEA extraction, the brain sections were returned to 4% PFA for an additional 48 hours at 4 °C and then stored in 1X PBS at 4 °C.

4.2.4 Tissue slicing

Brain sections were trimmed of excess tissue and the implant portions were separated from each other. The implant sections were placed in 4% PFA for 5 days followed by 8 days in 1X PBS at 4 °C. Implant sections were cryoprotected in 30% sucrose (Sigma Aldrich, St. Louis, MO, USA) in 1X PBS at 4 °C for 26 days and then frozen at -80 °C in optimal cutting temperature compound (Tissue-Tek, Sakura Finetek USA, Inc., Torrance, CA, USA). The tissue was sliced perpendicular to the implantation sites in 100 µm thick sections at -16 °C. Slices were stored in 0.02% azide (DSS24080, Dot Scientific Inc., Burton, MI, USA) in 1X PBS at 4 °C until immunohistochemical labeling. Slices are labelled by their final depth in hundreds of microns from the surface of the brain. For example, slice 13 contains tissue 1200 – 1300 µm from the brain surface.

4.2.5 Tissue staining

Slices were selected for staining at varying depths along the electrode shank. Slices are referred to by the lowest depth that they reach, for example slice 13 contains tissue from 1200 µm to 1300 µm below the brain surface. Tissue slices were blocked and permeabilized with StartingBlock PBS Blocking Buffer (37538, Thermo Scientific, Waltham, MA, USA) with 1% Triton X-100 (9002-93-1, Sigma Aldrich, St. Louis, MO, USA) overnight at 4 °C followed by three washes (30 min per wash) in 1X PBS containing 0.5% Triton X-100 (0.5% PBST) at room temperature. The tissue was incubated with primary antibodies at a 1:250 dilution in 0.5% PBST with azide for 48 hours at 4 °C. Three primary antibodies were used: mouse anti-neuronal nuclei (NeuN) (MAB377, MilliporeSigma, Burlington, MA, USA) for neurons, rabbit anti-Iba-1 (019-19741, FUJIFILM Wako, Osaka, Japan) or guinea pig anti-Iba-1 (234004, Synaptic Systems, Göttingen, Germany) for microglia and macrophages, and rabbit anti-glial fibrillary acidic protein (GFAP) (Z0334, Dako, Santa Clara, CA, USA) for astrocytes. After washing (3x, 30 min per wash)

in 0.5% PBST at room temperature, the tissue was incubated in secondary antibodies at a 1:250 dilution in 0.5% PBST with azide for 24 hours at 4 °C. Three secondary antibodies were used: anti-mouse Alexa Fluor 647 (715-605-150, Jackson ImmunoResearch Laboratories, Inc., Carlsbad, CA, USA), anti-rabbit Alexa Fluor 546 (A10040, Invitrogen, Waltham, MA, USA), and anti-guinea pig Alexa Fluor 488 (706-545-148, Jackson ImmunoResearch Laboratories, Inc., Carlsbad, CA, USA). A stain for all cell nuclei, Hoechst (1:250, 33342, Thermo Fisher Scientific, Waltham, MA, USA) or DAPI (1:250, D1306, Invitrogen, Waltham, MA, USA), was added during the secondary antibody incubation. Finally, the tissue slices were washed in room temperature 0.5% PBST two times at two-hour intervals and kept in 1X PBS overnight. All slices were stored at 4 °C in 1X PBS with 0.02% azide until ready to image.

4.2.6 Tissue imaging

Tissue slices were imaged on a Zeiss LSM 780 Confocal Microscope with a 20X objective. Images were collected with an approximately 0.4-0.6 µm X and Y pixel size and 2 µm z-step. Stains were imaged at wavelengths of 543 nm or 488 nm (Iba-1), 405 nm (Hoechst or DAPI), 633 nm (NeuN), and 543 nm (GFAP). A 100 µm z-stack was acquired in 2 µm steps to visualize the depth of the slice. All laser intensities were adjusted manually to prevent pixel saturation and ranged from 1.2-80% laser power. The gain and contrast were altered during image processing in ImageJ. Analysis here relies solely on the NeuN stain.

4.2.7 Tissue analysis

Neuron density around electrode sites was calculated from the NeuN tissue images and compared to the density in non-implanted tissue (termed “healthy” tissue). Healthy tissue sites were selected in areas outside regions of visible damage. Electrode sites and healthy tissue regions were cropped to 400 µm by 400 µm sections in MATLAB (Mathworks, Natick, MA, USA). Each

electrode hole was centered in the cropped image. Images with a z-stack were also cropped to the center 70 µm of the 100 µm-thick slice for a total 3D volume of 11.2E6 μm^3. Each cropped image was pre-processed in ImageJ (U. S. National Institutes of Health, Bethesda, Maryland, USA). The pixel intensity was normalized across z-stacks using the histogram matching feature of the highest signal-to-noise ratio z-stack. The image was filtered with a mean 50-pixel filter and the background was subtracted to remove pixelated noise. The image was then despeckled with a 3D Gaussian 2-pixel radius filter to remove individual pixels with abnormally high intensity, followed by a 3D median filter of 2-pixel radius for further noise reduction.

Then, the pre-processed image was read into MATLAB for 3D visualization using the Volume Viewer application. A 3D view of the neurons was generated using the isosurface feature with a unique isosurface value for each slice, as determined by a trained operator. This image was imported back into ImageJ for cell counting. In ImageJ, the image was smoothed and converted to 8-bit grayscale. The range of particle sizes used to identify neurons was determined by measuring the smallest and largest neurons by a trained operator. The Analyze Particles program was run to locate neurons and a trainer operator reviewed the resultant identifications for misidentified or unidentified neurons. A region of interest manager counted the identified neurons. The neuron density was calculated by dividing the total neuron count by the total volume.

4.2.8 UEA scanning electron microscopy imaging

UEAs were removed from 1X PBS and rinsed in deionized water for 1 hour. Remaining brain tissue was visibly noticed detaching from the center of the UEAs. UEAs were air dried for 1 hour and then affixed to SEM stubs (16111, Ted Pella, Redding, CA, USA) with carbon tape (16073, Ted Pella, Redding, CA, USA). UEAs were imaged in a TESCAN Rise SEM (Tescan Orsay Holding, Brno–Kohoutovice, Czech Republic) at 20 kV using the low vacuum secondary

detector. UEAs were tilted to approximately 20 degrees for maximum visibility. Images were collected of the whole array and of each quadrant of electrode shanks. Backscatter mode images were also collected to detect cracks in the parylene insulation.

4.2.9 Electrode analysis

Images of each UEA quadrant were analyzed for six categories of degradation: electrode tip breakage (TB), electrode coating cracks (CC), shank fracture (SF), abnormal debris (AB), parylene cracks (PC), and parylene delamination (PD). Examples of each category are shown in Figure 15B. All categories were analyzed using secondary electron images, besides parylene cracks which used backscatter electron images. Three trained operators scored each shank as exhibiting (1) or not exhibiting (0) the degradation category. Scores were averaged across operators and then rounded to 0 or 1. For select categories, the outer three rows of electrode shanks were statistically compared in an ANOVA test to the inner 4x4 electrode shanks (alpha < 0.05). Analysis was conducted using MATLAB.

4.3 Results

4.3.1 Analysis of neuron density

We analyzed the tissue slices in the left sensory cortex at three depths along the length of electrode shanks: 800-900 µm, 1000-1100 µm, and 1200-1300 µm. Figure 14 depicts the electrode (Figure 14B) and healthy tissue (Figure 14C) regions of interest analyzed in slice 11. Representative images of the three main stages of the analysis are shown in Figure 14B and 2C: the original image (top), the image after filtering and processing (middle), and the image analyzed with Analyze Particles in ImageJ (bottom). Using this process, we determined a healthy tissue density of 40.36e-6 neurons/μm^3 for slice 9, 33.75e-6 neurons/μm^3 for slice 11 and 38.21e-6 neurons/μm^3 for slice 13. These values are on the same order of magnitude as those in previous

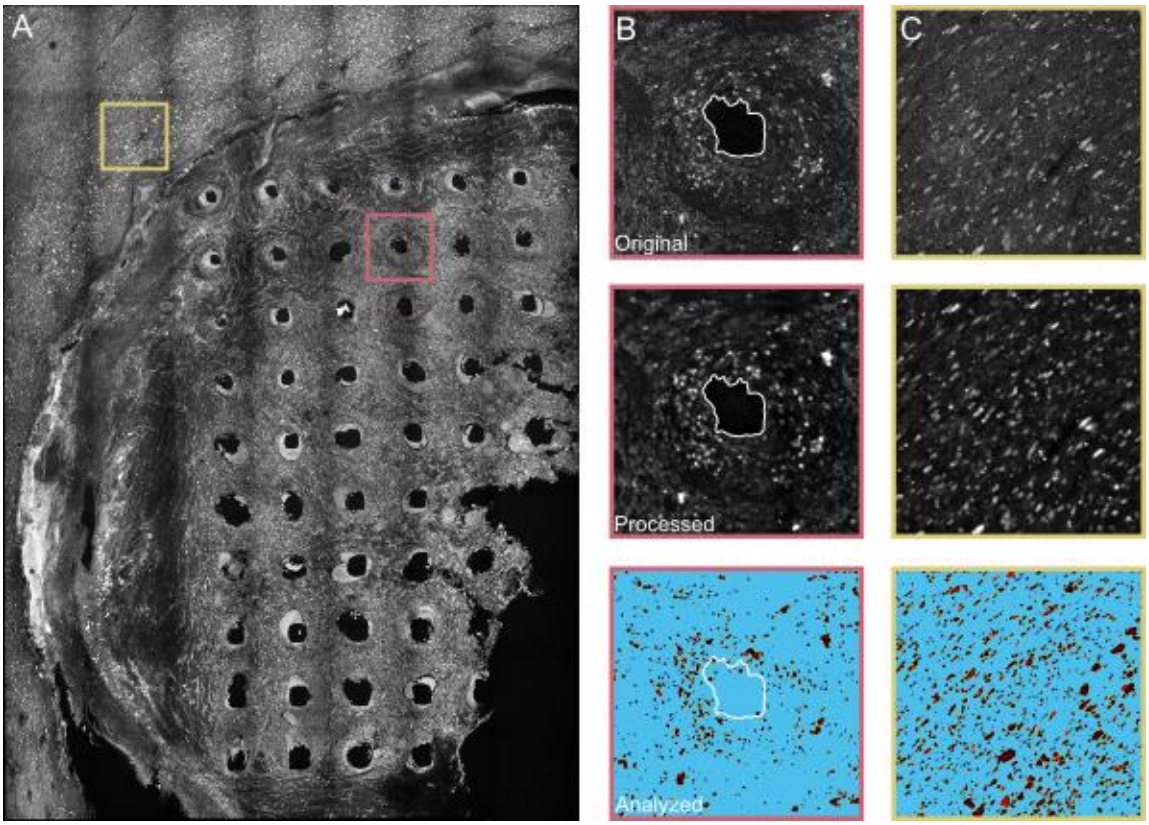

Figure 12 Tissue analysis of NeuN staining of slice 11 in the left sensory cortex. A) Confocal image of slice 11 (tissue 1000–1100 µm from brain surface) at a z-stack approximately in the center of the slice. Slice 11 shows 51 intact electrodes holes and nearby healthy tissue. The pink box (400 µm x 400 µm) outlines a representative electrode hole seen in (B) and yellow box outlines the healthy tissue seen in (C). The representative electrode hole (B) and healthy tissue (C) are depicted in original form (top), after filtering and other processing steps (middle), and after analysis in ImageJ with the Analyze Particles program (bottom). Images in (B) and (C) are 400 µm x 400 µm.

studies that found a healthy neuron density in the primary motor (66e-6 neurons/µm^3) and primary somatosensory (101e-6 neurons/µm^3) areas of the marmoset NHP cortex [179]. In comparison, there were fewer neurons in the tissue around the electrode holes. We calculated a mean neuron density surrounding the 232 electrodes holes of 9.95e-6 ± 5.68e-6 neurons/µm^3. The neuron density surrounding the electrode holes was reduced by 73.4% compared to the nearby healthy tissue. Table 2 contains a full listing of the mean neuron count and density for each tissue slice.

4.3.2 Analysis of UEA electrodes

SEM images were collected of the four Utah arrays to identify visible damage to the electrode shanks. Damage was categorized into six groupings: tip breakage, tip coating cracking, shank fracture, abnormal debris, parylene delamination, and parylene cracking.

Examples of each category are depicted in Figure 15B as a subset of the left sensory array. One experimental array implanted in the left motor region was excluded from the characterization study due to a lack of parylene and tip coating. We quantified the occurrence of the six damage categories over the three arrays (N=300 electrode shanks), shown in Figure 15C. When ranked from most to least present, the six categories were parylene cracks (40.3%), coating cracks.

Table 2 Neuron count and density of healthy and electrode tissue. Values are from the slices under the UEA in the left sensory cortex.

Tissue Slice	**Region of Interest**	**Mean Neuron Count**	**SD Neuron Count**	**Mean Neuron Density (*e-6 neurons/μm^3)**	**SD Neuron Density (*e-6 neurons/μm^3)**	**Number of Areas**
Left Sensory Slice 9	Healthy	452.00	-	40.36	-	1
	Electrode	107.16	60.53	9.57	5.37	85
Left Sensory Slice 11	Healthy	378.00	-	33.75	-	1
	Electrode	146.92	64.69	13.12	5.78	51
Left Sensory Slice 13	Healthy	428.00	-	38.21	-	1
	Electrode	80.26	65.91	7.16	5.68	96
Average	Healthy	419.33	-	37.44	-	1
	Electrode	111.45	63.71	9.95	5.68	232

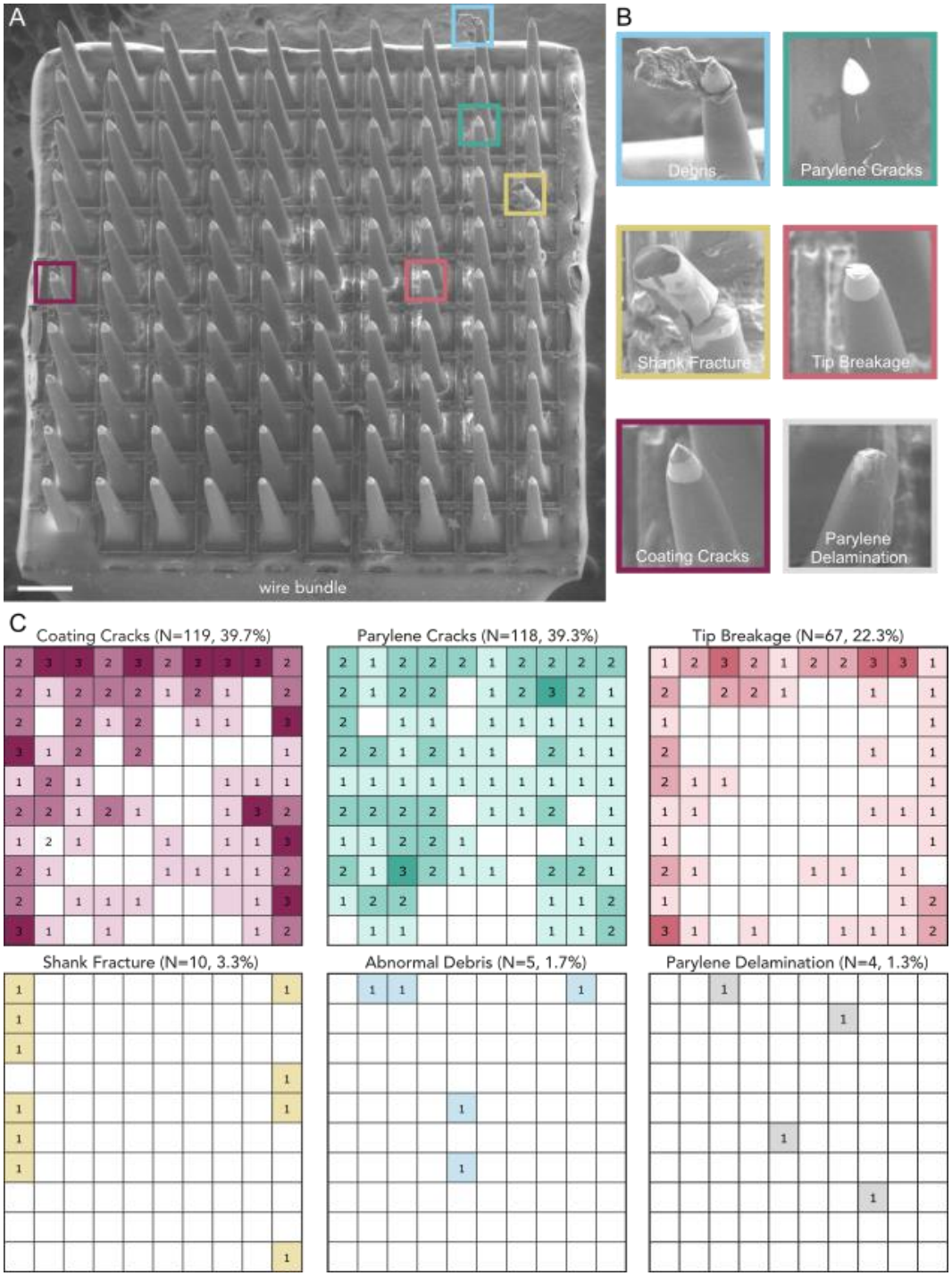

Figure 13 Explanted UEA SEM images and analysis for degradation. A) SEM image of the UEA implanted in the left sensory cortex for 848 days. The UEA is oriented with the wire bundle on the bottom edge. Boxes correspond to the categories of degradation in (B). Scale bar is 400 µm. B) Example images of the six categories quantified across three UEAs. Images of debris, parylene cracks, shank fracture, tip breakage, and coating cracks are from the UEA in the left sensory cortex in (A). The representative image of parylene delamination is from the UEA in the right motor cortex, as the UEA in the left sensory cortex did not exhibit parylene delamination. C) Heat maps of the summation of categorical occurrences in the three UEAs analyzed. The orientation of each heat map is that of the image in (A). Coating cracks occurred most frequently (N=119 electrode shanks, 39.7%). Parylene cracks occurred on 118 electrode shanks (39.3%) and tip breakage on 67 electrode shanks (22.3%). Coating cracks and tip breakage were significantly more frequent in the outer three rows of electrode shanks than the inner four rows (p-value < 0.05). Shank fracture (N=10, 3.3%), abnormal debris (N=5, 1.7%), and parylene delamination (N=4, 1.3%) occurred less frequently.

(39.7%), tip breakage (22.3%), shank fracture (3.3%), abnormal debris (1.7%), and parylene delamination (1.3%).

We analyzed the spatial arrangement of each of the most frequently occurring three categories – parylene cracks, coating cracks, and tip breakage – to determine location dependence (Figure 15C). We performed a 1-way ANOVA test comparing the occurrence of degraded shanks in the outermost three rows of electrode shanks to the innermost 4x4 square of electrode shanks. This was performed for each degradation category. There was a significant difference between the outer and inner electrode shanks for the coating cracks ($p=0.003$) and tip breakage ($p=0.004$). However, parylene cracks were not significantly different between outer and inner electrode shanks ($p=0.1601$).

4.4 Discussion

In the present study, we explored the question of UEA longevity in the brain. We analyzed the histological response to and the mechanical degradation of UEAs implanted in the cortex of an NHP for 1.6 and 2.3 years. The purpose of this study was to determine possible damage from implanted UEAs on brain tissue, and possible damage to UEAs after multiple years in the brain. This may enrich our understanding of the failure mechanisms in long term BMIs.

Here, we calculated the neuron density surrounding the electrode shank holes and nearby healthy tissue. We found a 73% decrease in neuron density, from a mean density of 37.44e-6 neurons/μm^3 in healthy tissue to a mean density of 9.95e-6 neurons/μm^3 around electrode holes. Many previous studies have examined the formation of a scar around chronically implanted UEAs [41]. However, few have quantified the effect UEAs have on the nearby neuron population in NHPs [19], [108], [175], [180], [181]. Our preliminary observations note a dramatic decrease in neurons within the immediate recording radius of the electrode, indicating that signal loss from

long term UEAs may be due to a lack of neurons. However, given that the tissue analyzed in this study did not capture the electrode tip, it may be possible that neurons migrated down along the shank to a location where the shank was thinner and perhaps caused less damage.

This study also evaluated SEM images of the extracted UEAs. We examined the UEAs for tip breakage, tip coating cracking, shank fracture, abnormal debris, parylene delamination, and parylene cracking. Tip breakage, coating cracking, and parylene cracking appeared on 20–40% of the electrode shanks, while shank fracture, abnormal debris, and parylene delamination appeared on fewer than 4% of shanks. A concentration of degradation at the smallest diameter, most vulnerable portion of the electrode shank, the tip, is not unusual. However, parylene cracking indicates a substantial decrease in electrical impedance, which we did not see from anecdotal evidence. The parylene cracks may be a result of the pressure within the SEM, despite being imaged under low vacuum. We found a significant difference in the number of electrode shanks on the outer perimeter of the UEA as compared to the innermost electrode shanks for tip breakage and coating cracks. This is likely due to lateral stresses placed on the outermost electrode arrays and is expected. Finally, our surgical notes indicate that some shank fracture may have occurred during extraction from the fixed tissue, although a precise number is not known.

While this study furthers our knowledge on the impact of chronic UEA implantation, it is also limited in a number of ways. The most obvious limitation is the single NHP used in this study. Higher-order animal models are invaluable to clinical research, and therefore studies are constructed to maximize the lifespan and usefulness of each animal [19], [175]. This study was also limited in the number of UEAs implanted in the single NHP. Four UEAs were implanted, one per cortex region of interest in each hemisphere. However, upon termination, one array was discovered to be fully encapsulated in fibrotic tissue. Previous studies have examined the fibrotic

tissue response to implanted silicon electrodes and found that fibrotic encapsulation is not an unusual outcome for long term implants [182]. Fibrotic encapsulation is particularly prevalent in chronic nerve studies [36]. However, few studies have examined the explanted UEA for damage or degradation [165]. This study found that the encapsulated UEA was devoid of metal tip coating material or parylene insulation, despite the silicon structure remaining otherwise intact. It is possible that the reactive oxide species in the fibrotic encapsulation caused severe degradation of the parylene and metal tip coating, while the fibrotic tissue provided a buffer against physical damage [40].

This study is also limited by the available stained tissue. Therefore, the location of the healthy tissue region is limited to an area just outside that of the UEA footprint. The healthy region neuron density that was found in this study does align with that of previous studies [179], but the region may still be impacted by the nearby UEA in ways unknown to us. Additionally, the depth of the tissue slices is not precisely known. The tissue depth is relative to the surface of the brain for that specific tissue section as the section is sliced in increments of 100 µm during the slicing process. However, the tissue surface can be irregular or cratered, making it difficult to know the exact depth of the tissue slice. Additionally, the tissue slices analyzed here do not encompass the UEA recording tips so it is difficult to know the distance between the recording region and the neurons in the slices analyzed here.

4.5 Conclusion

This study sheds light on the effects of chronically implanted UEAs in the motor and sensory cortices of an NHP. While mechanical damage occurred on 20–40% of electrode shanks, neuronal loss of nearly 73% near the electrode shanks likely contributes more to signal attenuation.

Therefore, this work indicates that BMI performance may be more limited by a lack of nearby neurons than material failures of UEAs.

Chapter 5: Discussion

5.1 Conclusion

Brain-machine interfaces and bioelectric medicine therapies rely on the development of increasingly small neural interfaces to seamlessly integrate with the central or peripheral nervous systems. The continual decrease in electrode size has resulted in the creation of sub-neuronal sized electrodes. However, such small devices are accompanied by problems relating to insertion capability, durability, and signal quality over time. Here, I propose a novel fabrication method of a neural interface, composed of carbon fibers, that overcomes many of these limitations. I also provide justification for this expansive use of carbon fiber electrodes in comparison to conventional silicon electrodes. I explore potential applications of this neural interface and discuss further research concerning its implementation.

In Chapter 2, I investigated the fabrication methods of carbon fiber arrays for improved brain recording yield and array longevity [6]. Upon the discovery that current carbon fiber construction methods resulted in irregular and inconsistent electrode surfaces, I developed a new method to create the carbon electrode using a laser. Laser cut carbon fiber electrodes resulted in consistent and less variable electrode surfaces. The electrodes also maintained a low 1kHz impedance and recorded large amplitude signals from the rat brain. Importantly, the recording yield of laser cut electrodes increased in both acute, short-term chronic, and long-term chronic settings. Over the course of a three-month study, conventional carbon fiber fabrication methods had a roughly 30% recording yield, while laser cut carbon fiber electrode arrays maintained a

greater than 80% recording yield. I also investigated electrode coatings to maintain a lower impedance over time. PEDOT:pTS, the conventional coating used in many neural implants, was compared against platinum iridium and bare carbon etched with oxygen plasma. While all recorded sizeable single units in the brain, PtIr and oxygen plasma did not degrade as rapidly as PEDOT:pTS in a heated saline soak test, highlighting how these alternative coatings may expand the lifespan of carbon fiber recording arrays.

Naturally, this work is useful for those who require the recording of isolated single units from neurons. Neuroscientists who specialize in electrophysiology, for example, would benefit greatly from the high SNR recordings [171]. Additionally, many neuroscience experiments examine small changes in neurological development, and require consistent, reproducible electrodes that do not add variability to an already complicated experimental system [183]. Research that couples electrophysiology with imaging modalities, like 3-photon microscopy [184] or fMRI [185], would benefit from the sub-cellular electrode diameter and non-metallic material of carbon fiber electrodes. Additionally, the precise localization of the electrodes after recording experiments is useful for studies in the field of connectomics, in which electrodes must remain in place as the brain tissue is sliced [8], [186]. Medical electrode uses require that brain tissue is healthy and undamaged [187]. Therefore, these electrodes will be useful for researchers who look to increase BMI yield [12], to monitor healthy brain tissue for epileptic seizures [188], and facilitate a closed-loop DBS implant when studying Parkinson's disease [189].

In Chapter 3, I developed a carbon fiber electrode array suitable for recording from neural structures in the peripheral nervous system, called the carbon fiber silicone array (CFSA) [7]. The novel CFSA uniquely combined carbon fiber electrode with a soft silicone backing. The silicone-embedded carbon fibers were resistant to breakage and durable, withstanding 50,000 bends. The

CFSA also featured sharpened carbon fiber electrodes that were created with a blowtorch. Carbon fibers of a length appropriate for insertion into the rat vagus nerve, roughly 200–250 μm in length, were sharpened and easily inserted into the rat cervical vagus nerve and feline dorsal root ganglia. We recorded spontaneous acute neural signals from the rat cervical vagus nerve and physiologically relevant signals from the feline dorsal root ganglia. Sharpened carbon fibers also penetrated the rat brain to a depth previously only reached by carbon fibers with insertion assistance. The work in this chapter illustrates the many features of carbon fiber electrodes and the range of possible avenues for carbon fibers to be integrated into bioelectric medicine technologies in the peripheral nervous system.

Research done in the periphery would benefit from this durable array of sub-cellular electrodes. In particular, the CFSA has the potential to replace Utah electrode arrays (UEAs) in long-term peripheral recording studies, in which most UEAs failed to obtain useful signals just weeks after implantation [10]. The periphery is a harsh environment, so a durable array that can withstand the torsion and compression of the moving musculature around it is needed [9]. Additionally, size precluded UEAs from interfacing with autonomic nerves of < 1 mm diameter [24]. This work can enable the exploration of the vast and interconnected autonomic nervous system, currently a relatively unknown part of the body [11]. Our companion paper further explores vagus recordings from sharpened carbon fiber electrodes in relation to blood glucose levels [144]. Understanding the autonomic nervous system may increase our ability to treat many systemic, chronic disorders, such as cardiac-related disease, PTSD, and diabetes [23]. This array may also prove useful for nerve machine interface studies, such as those connecting distal ends of amputated nerves to prostheses [190]–[194], or those using closed-loop control of the bladder with stimulation in paralyzed patients [28], [29], [195]. This work may be translated into studies

involving other small peripheral structures, such as the ganglia in sea slugs [156], [196] or spinal cord interfaces [197], [198].

In Chapter 4, I analyzed the histological outcomes of chronically implanted UEAs in the motor and sensory cortices of a non-human primate. This work identified possible repercussions of indwelling UEAs in the brain's cortex. One identified repercussion is the substantial decrease in neuronal density surrounding the electrode shanks. I found that the neuron density decreased by 73% within 200 μm of the center of the electrode shank hole, as compared to nearby healthy tissue. This result is similar to those in studies analyzing the long-term effects of UEA implants in nerves [36], [38], [41]. Here, I also identified a repercussion of damage on the electrode tip and shank after explant, similar to previous nerve implant studies [165]. After implantation for 1.6 or 2.3 years, I found that approximately 40% of electrode shanks exhibited coating cracks and 20% exhibited signs of tip breakage. Both of these damage types occurred more significantly in the peripheral edges of the UEA as compared to the central region of shanks. Evidence of parylene cracks, parylene delamination, shank fracture, and abnormal debris were also identified. This work offers insight into the outcomes of long-term UEA implantation in the cortex. While UEAs are still a useful tool for tetraplegic patient populations, whose motor signals are not transmitted from their brain without the assistance of a brain-machine interface [14], [72], [199], this work may caution the use of UEAs in healthy, useable brain tissue [200].

5.2 Future Directions

5.2.1 Innovative peripheral neural interfaces

The results shown here illuminate a variety of neural applications for carbon fiber electrodes, however future work should continue to explore and optimize modifications of these devices. First, carbon fiber electrodes can continue to be modified through fabrication and

packaging changes to match the needs of the target neural structure. To record spontaneous single neural units from unmyelinated axons, for example, the sharpened carbon fiber geometry may need to decrease in surface area. Second, chronic testing of carbon fibers in the periphery should also be a priority. While evidence from chronic brain studies suggest a minimal impact of carbon fibers in nerves or ganglia, long-term studies have yet to be conducted. Testing of non-functional devices can illuminate the histological response to chronically indwelling carbon fibers. Functional studies can detect failures and future improvements to the recording capabilities of the carbon fiber electrodes. Third, future work can also continue to apply carbon fiber technology to new neural systems or to other species. This work provides a template for how to adapt carbon fiber technology from one nervous system to another, within and between animal species. Durable, sub-neuronal sized electrodes may be helpful in the study of cardiac cells, which require an electrode that can withstand substantial movement in the nearby environment. CFSAs may be applicable to other species with neuroanatomies of interest, such as octopi or Aplysia. Lastly, future work should orient towards the creation of a carbon fiber array that can also stimulate neural tissue. The adaptability of the carbon fiber electrodes to multiple shapes and coatings gives future researchers many tools to choose from when optimizing carbon fiber electrodes for electrical stimulation. Only once carbon fiber electrodes have been shown to stimulate as effectively as they can record will they become an invaluable tool for neural researchers.

5.2.2 Progress toward advanced bioelectric medicine therapies

This work paves the way for bioelectric medicine therapies that are patient-specific, long-lasting, and easily modulated [11], [23], [201]. In the future, bioelectric medicine therapies could replace pharmaceutical interventions and diseases could be treated with a specialized electrical stimulation regime [201]. Additionally, with the advanced recording capabilities of carbon fiber

electrodes, these future therapies can rely on closed-loop control to small fluctuations in input signal [24]. As carbon fiber technologies progress through chronic animal studies of increasingly higher order, our knowledge of their therapeutic applications will grow and become more specific. Each application will further elucidate the features and limitations of carbons fibers. This thesis may guide researchers in the development of biocompatible, minimally damaging interfaces and pave the way for bioelectric medicines for the treatment diseases.

Bibliography

[1] N. G. Hatsopoulos and J. P. Donoghue, "The science of neural interface systems," *Annu. Rev. Neurosci.*, vol. 32, pp. 249–266, 2009.

[2] R. Chen, A. Canales, and P. Anikeeva, "Neural recording and modulation technologies," *Nat. Rev. Mater.*, vol. 2, no. 2, pp. 1–16, 2017.

[3] K. M. Szostak, L. Grand, and T. G. Constandinou, "Neural interfaces for intracortical recording: Requirements, fabrication methods, and characteristics," *Front. Neurosci.*, vol. 11, no. DEC, 2017.

[4] W. M. Grill, S. E. Norman, and R. V. Bellamkonda, "Implanted neural interfaces: biochallenges and engineered solutions," *Annu. Rev. Biomed. Eng.*, vol. 11, pp. 1–24, 2009.

[5] T. D. Y. Kozai *et al.*, "Ultrasmall implantable composite microelectrodes with bioactive surfaces for chronic neural interfaces," *Nat. Mater.*, vol. 11, no. 12, pp. 1065–1073, Dec. 2012.

[6] E. J. Welle *et al.*, "Ultra-small carbon fiber electrode recording site optimization and improved in vivo chronic recording yield," *J. Neural Eng.*, vol. 17, no. 2, 2020.

[7] E. J. Welle *et al.*, "Sharpened and mechanically durable carbon fiber electrode arrays for neural recording," *IEEE Trans. Neural Syst. Rehabil. Eng.*, vol. Accepted., 2021.

[8] P. R. Patel *et al.*, "High density carbon fiber arrays for chronic electrophysiology, fast scan cyclic voltammetry, and correlative anatomy," *J. Neural Eng.*, vol. 17, no. 5, 2020.

[9] C. E. Larson and E. Meng, "A review for the peripheral nerve interface designer," *J. Neurosci. Methods*, vol. 332, Feb. 2020.

[10] S. Wendelken *et al.*, "Restoration of motor control and proprioceptive and cutaneous sensation in humans with prior upper-limb amputation via multiple Utah Slanted Electrode Arrays (USEAs) implanted in residual peripheral arm nerves," *J. Neuroeng. Rehabil.*, vol. 14, no. 1, pp. 1–17, 2017.

[11] K. Birmingham *et al.*, "Bioelectronic medicines: A research roadmap," *Nat. Rev. Drug Discov.*, vol. 13, no. 6, pp. 399–400, 2014.

[12] M. A. Lebedev and M. A. L. Nicolelis, "Brain-Machine Interfaces: From Basic Science to Neuroprostheses and Neurorehabilitation," *Physiol. Rev.*, vol. 97, no. 2, pp. 767–837, 2017.

[13] J. L. Collinger *et al.*, "High-performance neuroprosthetic control by an individual with tetraplegia," *Lancet*, vol. 381, no. 9866, pp. 557–564, 2013.

[14] L. R. Hochberg *et al.*, "Reach and grasp by people with tetraplegia using a neurally controlled robotic arm," *Nature*, vol. 485, no. 7398, pp. 372–375, May 2012.

[15] S. N. Flesher *et al.*, "Intracortical microstimulation of human somatosensory cortex," *Sci. Transl. Med.*, vol. 8, no. 361, pp. 1–10, 2016.

[16] R. A. Normann and E. Fernandez, "Clinical applications of penetrating neural interfaces and Utah Electrode Array technologies," *J. Neural Eng.*, vol. 13, no. 6, 2016.

[17] R. A. Normann, E. M. Maynard, P. J. Rousche, and D. J. Warren, “A neural interface for a cortical vision prosthesis,” *Vision Res.*, vol. 39, no. 15, pp. 2577–2587, 1999.
[18] A. Branner and R. A. Normann, “A multielectrode array for intrafascicular recording and stimulation in sciatic nerve of cats,” *Brain Res. Bull.*, vol. 51, no. 4, pp. 293–306, 2000.
[19] J. C. Barrese *et al.*, “Failure mode analysis of silicon-based intracortical microelectrode arrays in non-human primates,” *J. Neural Eng.*, vol. 10, no. 6, 2013.
[20] A. J. Bullard, B. C. Hutchison, J. Lee, C. A. Chestek, and P. G. Patil, “Estimating Risk for Future Intracranial, Fully Implanted, Modular Neuroprosthetic Systems: A Systematic Review of Hardware Complications in Clinical Deep Brain Stimulation and Experimental Human Intracortical Arrays,” *Neuromodulation*, vol. 23, no. 4, pp. 411–426, 2020.
[21] A. K. Vaskov *et al.*, “Cortical Decoding of Individual Finger Group Motions Using ReFIT Kalman Filter,” *Front. Neurosci.*, vol. 12, no. November, 2018.
[22] S. R. Nason *et al.*, “A low-power band of neuronal spiking activity dominated by local single units improves the performance of brain–machine interfaces,” *Nat. Biomed. Eng.*, vol. 4, no. 10, pp. 973–983, 2020.
[23] K. Famm, B. Litt, K. J. Tracey, E. S. Boyden, and M. Slaoui, “A jump-start for electroceuticals.,” *Nature*, vol. 496, pp. 159–161, 2013.
[24] C. C. Horn, J. L. Ardell, and L. E. Fisher, “Electroceutical targeting of the autonomic nervous system,” *Physiology*, vol. 34, no. 2, pp. 150–162, 2019.
[25] H. H. O. Müller, S. Moeller, C. Lücke, A. P. Lam, N. Braun, and A. Philipsen, “Vagus nerve stimulation (VNS) and other augmentation strategies for therapy-resistant depression (TRD): Review of the evidence and clinical advice for use,” *Front. Neurosci.*, vol. 12, no. 239, 2018.
[26] H. A. Sackeim *et al.*, “Vagus Nerve Stimulation (VNS^{TM}) for Treatment-Resistant Depression: Efficacy, Side Effects, and Predictors of Outcome,” 2001.
[27] R. L. Johnson and C. G. Wilson, “A review of vagus nerve stimulation as a therapeutic intervention,” *J. Inflamm. Res.*, vol. 11, pp. 203–213, 2018.
[28] T. M. Bruns, D. J. Weber, and R. A. Gaunt, “Microstimulation of Afferents in the Sacral Dorsal Root Ganglia Can Evoke Reflex Bladder Activity,” *Neurourol. Urodyn.*, vol. 71, no. January 2014, pp. 65–71, 2015.
[29] Z. Ouyang, Z. J. Sperry, N. D. Barrera, and T. M. Bruns, “Real-Time Bladder Pressure Estimation for Closed-Loop Control in a Detrusor Overactivity Model,” *IEEE Trans. Neural Syst. Rehabil. Eng.*, vol. 27, no. 6, pp. 1209–1216, 2019.
[30] M. L. Settell *et al.*, “SPARC: A Road Map for Vagus Nerve Stimulation: Evidence of Vagotopy in a Swine Model,” *Exp. Biol. 2020 Meet. Abstr.*, vol. 34, no. S1, 2020.
[31] C. Günter, J. Delbeke, and M. Ortiz-Catalan, “Safety of long-term electrical peripheral nerve stimulation: Review of the state of the art,” *J. Neuroeng. Rehabil.*, vol. 16, no. 1, 2019.
[32] C. L. Kolarcik *et al.*, “Host tissue response to floating microelectrode arrays chronically implanted in the feline spinal nerve,” *J. Neural Eng.*, vol. 17, no. 4, 2020.
[33] J. del Valle and X. Navarro, *Interfaces with the peripheral nerve for the control of neuroprostheses*, 1st ed., vol. 109. Elsevier Inc., 2013.
[34] S. Lee and C. Lee, “Toward advanced neural interfaces for the peripheral nervous system (PNS) and their future applications,” *Curr. Opin. Biomed. Eng.*, vol. 6, pp. 130–137, 2018.
[35] H. A. C. Wark *et al.*, “A new high-density (25 electrodes/mm2) penetrating microelectrode array for recording and stimulating sub-millimeter neuroanatomical

structures," *J. Neural Eng.*, vol. 10, no. 4, 2013.
[36] A. Branner, R. B. Stein, E. Fernandez, Y. Aoyagi, and R. A. Normann, "Long-Term Stimulation and Recording with a Penetrating Microelectrode Array in Cat Sciatic Nerve," *IEEE Trans. Biomed. Eng.*, vol. 51, no. 1, pp. 146–157, 2004.
[37] K. S. Mathews, H. A. C. Wark, and R. A. Normann, "Assessment of rat sciatic nerve function following acute implantation of high density utah slanted electrode array (25 electrodes/mm2) based on neural recordings and evoked muscle activity," *Muscle and Nerve*, vol. 50, no. 3, pp. 417–424, 2014.
[38] H. A. C. Wark, K. S. Mathews, R. A. Normann, and E. Fernandez, "Behavioral and cellular consequences of high-electrode count Utah Arrays chronically implanted in rat sciatic nerve," *J. Neural Eng.*, vol. 11, no. 4, 2014.
[39] K. A. Potter, A. C. Buck, W. K. Self, and J. R. Capadona, "Stab injury and device implantation within the brain results in inversely multiphasic neuroinflammatory and neurodegenerative responses," *J. Neural Eng.*, vol. 9, no. 4, 2012.
[40] E. S. Ereifej *et al.*, "Implantation of neural probes in the brain elicits oxidative stress," *Front. Bioeng. Biotechnol.*, vol. 6, no. FEB, 2018.
[41] M. B. Christensen, S. M. Pearce, N. M. Ledbetter, D. J. Warren, G. A. Clark, and P. A. Tresco, "The foreign body response to the Utah Slant Electrode Array in the cat sciatic nerve," *Acta Biomater.*, vol. 10, no. 11, 2014.
[42] R. Biran, D. C. Martin, and P. A. Tresco, "The brain tissue response to implanted silicon microelectrode arrays is increased when the device is tethered to the skull," *J. Biomed. Mater. Res. - Part A*, vol. 82, no. 1, pp. 169–178, 2007.
[43] J. W. Salatino, K. A. Ludwig, T. D. Y. Kozai, and E. K. Purcell, "Glial responses to implanted electrodes in the brain," *Nat. Biomed. Eng.*, vol. 1, no. 11, pp. 862–877, 2017.
[44] A. C. Patil and N. V. Thakor, "Implantable neurotechnologies: a review of micro- and nanoelectrodes for neural recording," *Med. Biol. Eng. Comput.*, vol. 54, no. 1, pp. 23–44, 2016.
[45] S. Romeni, G. Valle, A. Mazzoni, and S. Micera, "Tutorial: a computational framework for the design and optimization of peripheral neural interfaces," *Nat. Protoc.*, vol. 15, no. 10, pp. 3129–3153, 2020.
[46] F. Deku, Y. Cohen, A. Joshi-Imre, A. Kanneganti, T. Gardner, and S. Cogan, "Amorphous silicon carbide ultramicroelectrode arrays for neural stimulation and recording," *J. Neural Eng.*, 2018.
[47] J. P. Seymour and D. R. Kipke, "Neural probe design for reduced tissue encapsulation in CNS," *Biomaterials*, vol. 28, no. 25, pp. 3594–3607, Sep. 2007.
[48] J. L. Skousen, S. M. E. Merriam, O. Srivannavit, G. Perlin, K. D. Wise, and P. A. Tresco, "Reducing surface area while maintaining implant penetrating profile lowers the brain foreign body response to chronically implanted planar silicon microelectrode arrays," in *Progress in Brain Research*, vol. 194, J. Schouenborg, M. Garwicz, and N. Danielsen, Eds. 2011, pp. 167–180.
[49] S. Wurth *et al.*, "Long-term usability and bio-integration of polyimide-based intra-neural stimulating electrodes," *Biomaterials*, vol. 122, pp. 114–129, 2017.
[50] N. Lago, K. Yoshida, K. P. Koch, and X. Navarro, "Assessment of biocompatibility of chronically implanted polyimide and platinum intrafascicular electrodes," *IEEE Trans. Biomed. Eng.*, vol. 54, no. 2, pp. 281–290, 2007.
[51] E. Delivopoulos, D. J. Chew, I. R. Minev, J. W. Fawcett, and S. P. Lacour, "Concurrent

recordings of bladder afferents from multiple nerves using a microfabricated PDMS microchannel electrode array," *Lab Chip*, vol. 12, no. 14, p. 2540, 2012.
[52] B. Lee *et al.*, "An Implantable Peripheral Nerve Recording and Stimulation System for Experiments on Freely Moving Animal Subjects," *Sci. Rep.*, vol. 8, no. 1, p. 6115, 2018.
[53] X. Zheng *et al.*, "Soft Conducting Elastomer for Peripheral Nerve Interface," *Adv. Healthc. Mater.*, vol. 1801311, pp. 1–10, 2019.
[54] J. Liu *et al.*, "Syringe-injectable electronics," *Nat. Nanotechnol.*, vol. 10, no. 7, pp. 629–635, 2015.
[55] G. A. McCallum *et al.*, "Chronic interfacing with the autonomic nervous system using carbon nanotube (CNT) yarn electrodes," *Sci. Rep.*, vol. 7, no. 1, 2017.
[56] J. T. Marmerstein, G. A. McCallum, and D. M. Durand, "Direct measurement of vagal tone in rats does not show correlation to HRV," *Sci. Rep.*, vol. 11, no. 1, 2021.
[57] L. Luan *et al.*, "Ultraflexible nanoelectronic probes form reliable , glial scar – free neural integration," *Sci. Adv.*, vol. 3, 2017.
[58] G. Di Pino *et al.*, "Invasive neural interfaces: The perspective of the surgeon," *J. Surg. Res.*, vol. 188, no. 1, pp. 77–87, 2014.
[59] J. Millar and C. W. A. Pelling, "Improved methods for construction of carbon fibre electrodes for extracellular spike recording," *J. Neurosci. Methods*, vol. 110, no. 1–2, pp. 1–8, 2001.
[60] C. M. Caldwell *et al.*, "Implantation analysis of a 16-channel carbon fiber microelectrode," in *Program No. 90.29. 2017 Neuroscience Meeting Planner*, 2017, p. Online.
[61] P. R. Patel *et al.*, "Insertion of linear 8.4 μ m diameter 16 channel carbon fiber electrode arrays for single unit recordings," *J. Neural Eng.*, vol. 12, no. 4, 2015.
[62] P. R. Patel *et al.*, "Chronic in vivo stability assessment of carbon fiber microelectrode arrays," *J. Neural Eng.*, vol. 13, no. 6, 2016.
[63] W. F. Gillis *et al.*, "Carbon fiber on polyimide ultra-microelectrodes," *J. Neural Eng.*, vol. 15, no. 1, 2017.
[64] A. B. Ajiboye *et al.*, "Restoration of reaching and grasping movements through brain-controlled muscle stimulation in a person with tetraplegia: a proof-of-concept demonstration," *Lancet*, vol. 389, no. 10081, pp. 1821–1830, 2017.
[65] C. E. Bouton *et al.*, "Restoring cortical control of functional movement in a human with quadriplegia," *Nature*, vol. 533, no. 7602, pp. 247–250, 2016.
[66] G. Hotson *et al.*, "Individual finger control of a modular prosthetic limb using high-density electrocorticography in a human subject," *J. Neural Eng.*, vol. 13, no. 026017, 2016.
[67] J. Cowley, L. Resnik, J. Wilken, L. S. Walters, and D. Gates, "Movement quality of conventional prostheses and the DEKA Arm during everyday tasks," *Prosthetics Orthot. Int.*, vol. 41, no. 1, pp. 33–40, 2017.
[68] R. A. R. C. Gopura, D. S. V. Bandara, K. Kiguchi, and G. K. I. Mann, "Developments in hardware systems of active upper-limb exoskeleton robots: A review," *Rob. Auton. Syst.*, vol. 75, pp. 203–220, 2016.
[69] A. J. Bullard *et al.*, "Design and testing of a 96-channel neural interface module for the Networked Neuroprosthesis system," *Bioelectron. Med.*, vol. 5, no. 1, p. 3, 2019.
[70] D. A. Borton, M. Yin, J. Aceros, and A. Nurmikko, "An implantable wireless neural interface for recording cortical circuit dynamics in moving primates," *J. Neural Eng.*, vol.

10, no. 2, 2013.
[71] B. Smith, T. J. Crish, J. R. Buckett, K. L. Kilgore, and P. H. Peckham, “Development of an implantable networked neuroprosthesis,” *2nd Int. IEEE EMBS Conf. Neural Eng.*, pp. 454–457, 2005.
[72] J. L. Collinger, B. Wodlinger, and A. B. Schwartz, “7 Degree-of-Freedom Neuroprosthetic Control By an Individual With Tetraplegia,” *Lancet*, vol. 381, no. 9866, pp. 557–564, 2012.
[73] S. Ben Hamed, M. H. Schieber, and A. Pouget, “Decoding M1 neurons during multiple finger movements,” *J. Neurophysiol.*, vol. 98, no. April 2007, pp. 327–333, 2007.
[74] A. G. Rouse and M. H. Schieber, “Spatiotemporal Distribution of Location and Object Effects in Primary Motor Cortex Neurons during Reach-to-Grasp,” *J. Neurosci.*, vol. 36, no. 41, pp. 10640–10653, 2016.
[75] C. T. Nordhausen, P. J. Rousche, and R. A. Normann, “Optimizing recording capabilities of the Utah Intracortical Electrode Array,” *Brain Res.*, vol. 637, no. 1–2, pp. 27–36, 1994.
[76] M. D. Serruya, N. G. Hatsopoulos, L. Paninski, M. R. Fellows, and J. P. Donoghue, “Instant neural control of a movement signal.,” *Nature*, vol. 416, no. 6877, pp. 141–2, 2002.
[77] V. Gilja *et al.*, “A high-performance neural prosthesis enabled by control algorithm design,” *Nat. Neurosci.*, vol. 15, no. 12, pp. 1752–7, 2012.
[78] L. R. Hochberg *et al.*, “Neuronal ensemble control of prosthetic devices by a human with tetraplegia,” *Nature*, vol. 442, no. 7099, pp. 164–71, 2006.
[79] C. Pandarinath *et al.*, “High performance communication by people with paralysis using an intracortical brain-computer interface,” *Elife*, vol. 6, pp. 1–27, 2017.
[80] T. M. Bruns, R. A. Gaunt, and D. J. Weber, “Multielectrode array recordings of bladder and perineal primary afferent activity from the sacral dorsal root ganglia,” *J. Neural Eng.*, vol. 8, no. 5, 2011.
[81] B. P. Christie, K. R. Ashmont, P. A. House, and B. Greger, “Approaches to a cortical vision prosthesis: Implications of electrode size and placement,” *J. Neural Eng.*, vol. 13, no. 2, 2016.
[82] E. M. Schmidt, M. J. Bak, F. T. Hambrecht, C. V. Kufta, D. K. O’Rourke, and P. Vallabhanath, “Feasibility of a visual prosthesis for the blind based on intracortical microstimulation of the visual cortex,” *Brain*, vol. 119, no. 2, pp. 507–522, 1996.
[83] J. D. Weiland, A. K. Cho, and M. S. Humayun, “Retinal prostheses: Current clinical results and future needs,” *Ophthalmology*, vol. 118, no. 11, pp. 2227–2237, 2011.
[84] R. E. Hampson *et al.*, “Developing a hippocampal neural prosthetic to facilitate human memory encoding and recall,” *J. Neural Eng.*, vol. 15, no. 3, 2018.
[85] C. A. Chestek *et al.*, “Long-term stability of neural prosthetic control signals from silicon cortical arrays in rhesus macaque motor cortex,” *J. Neural Eng.*, vol. 8, no. 4, 2011.
[86] F. Barz *et al.*, “Versatile, modular 3D microelectrode arrays for neuronal ensemble recordings: From design to fabrication, assembly, and functional validation in non-human primates,” *J. Neural Eng.*, vol. 14, no. 3, 2017.
[87] K. A. Ludwig, R. M. Miriani, N. B. Langhals, M. D. Joseph, D. J. Anderson, and D. R. Kipke, “Using a common average reference to improve cortical neuron recordings from microelectrode arrays,” *J. Neurophysiol.*, vol. 101, no. 3, pp. 1679–1689, 2009.
[88] E. Stark and M. Abeles, “Predicting movement from multiunit activity,” *J. Neurosci.*, vol. 27, no. 31, pp. 8387–8394, 2007.

[89] T. D. Kozai *et al.*, “Reduction of neurovascular damage resulting from microelectrode insertion into the cerebral cortex using in vivo two-photon mapping,” *J Neural Eng*, vol. 7, no. 4, p. 46011, 2010.
[90] R. Biran, D. C. Martin, and P. A. Tresco, “Neuronal cell loss accompanies the brain tissue response to chronically implanted silicon microelectrode arrays,” *Exp. Neurol.*, vol. 195, no. 1, pp. 115–126, 2005.
[91] G. R. Holt and C. Koch, “Electrical Interactions via the Extracellular Potential Near Cell Bodies,” *J. Comput. Neurosci.*, vol. 6, no. 2, pp. 169–184, 1999.
[92] M. A. Moffitt and C. C. McIntyre, “Model-based analysis of cortical recording with silicon microelectrodes,” *Clin. Neurophysiol.*, vol. 116, no. 9, pp. 2240–2250, 2005.
[93] J. M. Anderson, A. Rodriguez, and D. T. Chang, “Foreign body reaction to biomaterials,” *Semin. Immunol.*, vol. 20, no. 2, pp. 86–100, 2008.
[94] K. Scholten and E. Meng, “Materials for microfabricated implantable devices: a review,” *Lab Chip*, vol. 15, no. 22, pp. 4256–4272, 2015.
[95] J. R. Capadona, K. Shanmuganathan, D. J. Tyler, S. J. Rowan, and C. Weder, “Stimuli-responsive polymer nanocomposites inspired by the sea cucumber dermis,” *Science (80-.).*, vol. 319, no. 5868, pp. 1370–1374, 2008.
[96] C. Xie, J. Liu, T.-M. Fu, X. Dai, W. Zhou, and C. M. Lieber, “Three-dimensional macroporous nanoelectronic networks as minimally invasive brain probes,” *Nat. Mater.*, vol. 14, no. 12, pp. 1286–1292, 2015.
[97] G. Hong, T. M. Fu, T. Zhou, T. G. Schuhmann, J. Huang, and C. M. Lieber, “Syringe Injectable Electronics: Precise Targeted Delivery with Quantitative Input/Output Connectivity,” *Nano Lett.*, vol. 15, no. 10, pp. 6979–6984, 2015.
[98] T.-M. Fu, G. Hong, T. Zhou, T. G. Schuhmann, R. D. Viveros, and C. M. Lieber, “Stable long-term chronic brain mapping at the single-neuron level,” *Nat. Methods*, no. August, 2016.
[99] E. Musk and Neuralink, “An integrated brain-machine interface platform with thousands of channels,” *bioRxiv*, 2019.
[100] Z. Zhao, X. Li, F. He, X. Wei, S. Lin, and C. Xie, “Parallel, minimally-invasive implantation of ultra-flexible neural electrode arrays,” *J. Neural Eng.*, 2019.
[101] B. J. Kim *et al.*, “3D Parylene sheath neural probe for chronic recordings,” *J. Neural Eng.*, vol. 10, no. 4, 2013.
[102] G. Guitchounts, J. E. Markowitz, W. A. Liberti, and T. J. Gardner, “A carbon-fiber electrode array for long-term neural recording,” *J. Neural Eng.*, vol. 10, no. 4, 2013.
[103] H. N. Schwerdt *et al.*, “Long-term dopamine neurochemical monitoring in primates,” *Proc. Natl. Acad. Sci. U. S. A.*, vol. 114, no. 50, pp. 13260–13265, 2017.
[104] H. N. Schwerdt *et al.*, “Subcellular probes for neurochemical recording from multiple brain sites,” *Lab Chip*, 2017.
[105] T. L. Massey, S. R. Santacruz, J. F. Hou, K. S. J. Pister, J. M. Carmena, and M. M. Maharbiz, “A High-Density Carbon Fiber Neural Recording Array Technology,” *J. Neural Eng.*, vol. 16, no. 016024, 2019.
[106] A. Obaid *et al.*, “Massively Parallel Microwire Arrays Integrated with CMOS chips for Neural Recording,” *Sci. Adv.*, vol. 6, 2020.
[107] G. Guitchounts and D. D. Cox, “64-Channel Carbon Fiber Electrode Arrays for Chronic Electrophysiology,” *bioRxiv*, 2019.
[108] K. A. Malaga *et al.*, “Data-driven model comparing the effects of glial scarring and

interface interactions on chronic neural recordings in non-human primates," *J. Neural Eng.*, vol. 13, no. 1, 2016.
[109] N. J. Michelson and T. D. Y. Kozai, "Isoflurane and Ketamine Differentially Influence Spontaneous and Evoked Laminar Electrophysiology in Mouse V1," *J. Neurophysiol.*, p. jn.00299.2018, 2018.
[110] R. A. Green *et al.*, "Substrate dependent stability of conducting polymer coatings on medical electrodes," *Biomaterials*, vol. 33, no. 25, pp. 5875–5886, 2012.
[111] A. Petrossians, J. J. Whalen, J. D. Weiland, and F. Mansfeld, "Electrodeposition and Characterization of Thin-Film Platinum-Iridium Alloys for Biological Interfaces," *J. Electrochem. Soc.*, vol. 158, pp. D269–D276, 2011.
[112] I. R. Cassar *et al.*, "Electrodeposited platinum-iridium coating improves in vivo recording performance of chronically implanted microelectrode arrays," *Biomaterials*, vol. 205, no. November 2018, pp. 120–132, 2019.
[113] D. W. L. Hukins, A. Mahomed, and S. N. Kukureka, "Accelerated aging for testing polymeric biomaterials and medical devices," *Med. Eng. Phys.*, vol. 30, no. 10, pp. 1270–1274, 2008.
[114] "2016 Standard Guide for Accelerated Aging of Sterile Barrier Systems for Medical Devices," *(ASTM)*, vol. 10.1520/F1.
[115] G. Paxinos and C. Watson, *The Rat Brain in Stereotaxic Coordinates (New York: Academic)*. New York: Academic, 2007.
[116] T. S. Skoglund, R. Pascher, and C. H. Berthold, "The existence of a layer IV in the rat motor cortex," *Cereb. Cortex*, vol. 7, no. 2, pp. 178–180, 1997.
[117] V. S. Polikov, P. A. Tresco, and W. M. Reichert, "Response of brain tissue to chronically implanted neural electrodes," *J. Neurosci. Methods*, vol. 148, no. 1, pp. 1–18, Oct. 2005.
[118] "Offline Sorter User Guide Data Analysis Software," *Plexon Inc. (Dallas, Texas)*, vol. 3.0, 2009.
[119] S. F. Cogan, "Neural Stimulation and Recording Electrodes," *Annu. Rev. Biomed. Eng.*, vol. 10, no. 1, pp. 275–309, 2008.
[120] C. D. Lee, E. M. Hudak, J. J. Whalen, A. Petrossians, and J. D. Weiland, "Low-Impedance, High Surface Area Pt-Ir Electrodeposited on Cochlear Implant Electrodes," *J. Electrochem. Soc.*, vol. 165, no. 12, pp. G3015–G3017, 2018.
[121] J. P. Neto *et al.*, "Does impedance matter when recording spikes with polytrodes?," *Front. Neurosci.*, vol. 12, pp. 1–9, 2018.
[122] S. R. Dupont, F. Novoa, E. Voroshazi, and R. H. Dauskardt, "Decohesion kinetics of PEDOT:PSS conducting polymer films," *Adv. Funct. Mater.*, vol. 24, no. 9, pp. 1325–1332, 2014.
[123] R. D. Meyer, S. F. Cogan, T. H. Nguyen, and R. D. Rauh, "Electrodeposited iridium oxide for neural stimulation and recording electrodes," *IEEE Trans. Neural Syst. Rehabil. Eng.*, vol. 9, no. 1, pp. 2–11, 2001.
[124] T. M. Otchy *et al.*, "Printable microscale interfaces for long-term peripheral nerve mapping and precision control," *bioRxiv*, 2019.
[125] N. Saito *et al.*, "Application of carbon fibers to biomaterials: A new era of nano-level control of carbon fibers after 30-years of development," *Chem. Soc. Rev.*, vol. 40, no. 7, pp. 3824–3834, 2011.
[126] N. Driscoll *et al.*, "Two-Dimensional Ti3C2 MXene for High-Resolution Neural Interfaces," *ACS Nano*, vol. 12, pp. 10419–10429, 2018.

[127] X. Luo, C. L. Weaver, D. D. Zhou, R. Greenberg, and X. T. Cui, “Highly stable carbon nanotube doped poly(3,4-ethylenedioxythiophene) for chronic neural stimulation,” *Biomaterials*, vol. 32, no. 24, pp. 5551–5557, 2011.
[128] E. W. Keefer, B. R. Botterman, M. I. Romero, A. F. Rossi, and G. W. Gross, “Carbon nanotube coating improves neuronal recordings,” *Nat. Nanotechnol.*, vol. 3, no. 7, pp. 434–439, 2008.
[129] R. A. Schmidt *et al.*, “Sacral nerve stimulation for treatment of refractory urinary urge incontinence,” *J. Urol.*, vol. 162, no. 2, pp. 352–357, 1999.
[130] C. DeGiorgio *et al.*, “Vagus nerve stimulation for epilepsy: Randomized comparison of three stimulation paradigms,” *Neurology*, vol. 65, no. 2, pp. 317–319, 2005.
[131] G. Deuschl *et al.*, “A Randomized Trial of Deep-Brain Stimulation for Parkinson’s Disease,” *N. Engl. J. Med.*, vol. 355, no. 9, pp. 896–908, 2006.
[132] U. Andersson and K. J. Tracey, “Neural reflexes in inflammation and immunity,” *J. Exp. Med.*, vol. 209, no. 6, pp. 1057–1068, 2012.
[133] D. A. W. Janssen, F. M. J. Martens, L. L. de Wall, H. M. K. van Breda, and J. P. F. A. Heesakkers, “Clinical utility of neurostimulation devices in the treatment of overactive bladder: Current perspectives,” *Med. Devices Evid. Res.*, vol. 10, pp. 109–122, 2017.
[134] H. Charkhkar, B. P. Christie, G. J. Pinault, D. J. Tyler, and R. J. Triolo, “A translational framework for peripheral nerve stimulating electrodes: Reviewing the journey from concept to clinic,” *J. Neurosci. Methods*, vol. 328, 2019.
[135] X. Navarro, T. B. Krueger, N. Lago, S. Micera, T. Stieglitz, and P. Dario, “A Critical Review of Interfaces with the Peripheral Nervous System for the Control of Neuroprotheses and Hybrid Bionic Systems,” *J. Peripher. Nerv. Syst.*, vol. 10, pp. 229–258, 2005.
[136] M. Panebianco, A. Rigby, J. Weston, and A. G. Marson, “Vagus nerve stimulation for partial seizures,” *Cochrane Database Syst. Rev.*, no. 4, 2015.
[137] A. Branner, R. B. Stein, and R. A. Normann, “Selective Stimulation of Cat Sciatic Nerve Using an Array of Varying-Length Microelectrodes,” *J. Neurophysiol.*, vol. 85, no. 4, pp. 1585–1594, 2001.
[138] T. Boretius *et al.*, “A transverse intrafascicular multichannel electrode (TIME) to interface with the peripheral nerve,” *Biosens. Bioelectron.*, vol. 26, no. 1, pp. 62–69, 2010.
[139] J. Badia, T. Boretius, D. Andreu, C. Azevedo-Coste, T. Stieglitz, and X. Navarro, “Comparative analysis of transverse intrafascicular multichannel, longitudinal intrafascicular and multipolar cuff electrodes for the selective stimulation of nerve fascicles,” *J. Neural Eng.*, vol. 8, no. 3, 2011.
[140] D. M. Page *et al.*, “Motor Control and Sensory Feedback Enhance Prosthesis Embodiment and Reduce Phantom Pain After Long-Term Hand Amputation,” *Front. Hum. Neurosci.*, vol. 12, no. 352, 2018.
[141] T. S. Davis *et al.*, “Restoring motor control and sensory feedback in people with upper extremity amputations using arrays of 96 microelectrodes implanted in the median and ulnar nerves,” *J. Neural Eng.*, vol. 13, no. 3, 2016.
[142] M. M. Straka, B. Shafer, S. Vasudevan, C. Welle, and L. Rieth, “Characterizing longitudinal changes in the impedance spectra of in-vivo peripheral nerve electrodes,” *Micromachines*, vol. 9, no. 11, 2018.
[143] J. E. Woods, E. J. Welle, L. Chen, J. M. Richie, P. R. Patel, and C. A. Chestek, “Bending Properties of Materials for Peripheral Nerve Interfaces,” *Proc. 15th Annu. IEEE Int. Conf.*

Nano/Micro Eng. Mol. Syst., pp. 407–412, 2020.
[144] A. A. Jiman *et al.*, “Multi-channel intraneural vagus nerve recordings with a novel high-density carbon fiber microelectrode array,” *Sci. Rep.*, vol. 15501, 2020.
[145] Z. J. Sperry *et al.*, “Flexible microelectrode array for interfacing with the surface of neural ganglia,” *J. Neural Eng.*, vol. 15, no. 3, 2018.
[146] A. K. Ostrowski, Z. J. Sperry, G. Kulik, and T. M. Bruns, “Quantitative models of feline lumbosacral dorsal root ganglia neuronal cell density,” *J. Neurosci. Methods*, vol. 290, pp. 116–124, 2017.
[147] D. Ntiloudi, S. Zanos, M. A. Gatzoulis, H. Karvounis, and G. Giannakoulas, “How to evaluate patients with congenital heart disease-related pulmonary arterial hypertension,” *Expert Rev. Cardiovasc. Ther.*, vol. 17, no. 1, pp. 11–18, 2019.
[148] B. Panda *et al.*, “SPARC: Wireless, Continuous Monitoring of Bowel State and Function,” *Exp. Biol. 2020 Meet. Abstr.*, vol. 34, no. S1, 2020.
[149] T. P. Zanos *et al.*, “Identification of cytokine-specific sensory neural signals by decoding murine vagus nerve activity,” *Proc. Natl. Acad. Sci. U. S. A.*, vol. 115, no. 21, pp. E4843–E4852, 2018.
[150] A. Furniturewalla, P. Rustogi, E. Patrick, and J. W. Judy, “Modeling the Recording of Intraneural Action Potentials with Microelectrodes Using FEM and Point-Source Methods,” *Int. IEEE/EMBS Conf. Neural Eng. NER*, pp. 1191–1194, 2019.
[151] J. Pusch and B. Wohlmann, “Carbon Fibers,” in *Inorganic and Composite Fibers*, 2018, pp. 31–51.
[152] E. E. D. M. El-Giar and D. O. Wipf, “Preparation of tip-protected poly(oxyphenylene) coated carbon-fiber ultramicroelectrodes,” *Electroanalysis*, vol. 18, no. 23, pp. 2281–2289, 2006.
[153] M. S. Saleh *et al.*, “CMU Array: A 3D Nano-Printed, Customizable Ultra-High-Density Microelectrode Array Platform,” *bioRxiv*, 2019.
[154] K. Bielefeldt, F. Zhong, H. R. Koerber, and B. M. Davis, “Phenotypic characterization of gastric sensory neurons in mice,” *Am. J. Physiol. - Gastrointest. Liver Physiol.*, vol. 291, no. 5, pp. 987–997, 2006.
[155] K. Na *et al.*, “Novel diamond shuttle to deliver flexible neural probe with reduced tissue compression,” *Microsystems Nanoeng.*, vol. 6, no. 1, 2020.
[156] D. N. Lyttle, J. P. Gill, K. M. Shaw, P. J. Thomas, and H. J. Chiel, “Robustness, flexibility, and sensitivity in a multifunctional motor control model,” *Biol. Cybern.*, vol. 111, no. 1, pp. 25–47, 2017.
[157] A. Khurram *et al.*, “Chronic monitoring of lower urinary tract activity via a sacral dorsal root ganglia interface,” *J. Neural Eng.*, vol. 14, no. 3, 2017.
[158] L. E. Fisher, C. A. Ayers, M. Ciollaro, V. Ventura, D. J. Weber, and R. A. Gaunt, “Chronic recruitment of primary afferent neurons by microstimulation in the feline dorsal root ganglia,” *J. Neural Eng.*, vol. 11, no. 3, 2014.
[159] D. Yan *et al.*, “Microneedle Penetrating Array with Axon-Sized Dimensions for Cuff-less Peripheral Nerve Interfacing,” *Int. IEEE/EMBS Conf. Neural Eng. NER*, vol. 2019-March, pp. 827–830, 2019.
[160] T. S. Davis *et al.*, “Restoring motor control and sensory feedback in people with upper extremity amputations using arrays of 96 microelectrodes implanted in the median and ulnar nerves,” *J. Neural Eng.*, vol. 13, no. 3, 2016.
[161] G. A. Clark, N. M. Ledbetter, D. J. Warren, and R. R. Harrison, “Recording sensory and

motor information from peripheral nerves with Utah Slanted Electrode Arrays," *Proc. Annu. Int. Conf. IEEE Eng. Med. Biol. Soc. EMBS*, pp. 4641–4644, 2011.
[162] C. T. Nordhausen, E. M. Maynard, and R. A. Normann, "Single unit recording capabilities of a 100 microelectrode array," *Brain Res.*, vol. 726, no. 1–2, pp. 129–140, 1996.
[163] N. Y. Masse *et al.*, "Non-causal spike filtering improves decoding of movement intention for intracortical BCIs," *J. Neurosci. Methods*, vol. 236, pp. 58–67, 2014.
[164] J. D. Simeral, S. P. Kim, M. J. Black, J. P. Donoghue, and L. R. Hochberg, "Neural control of cursor trajectory and click by a human with tetraplegia 1000 days after implant of an intracortical microelectrode array," *J. Neural Eng.*, vol. 8, no. 2, 2011.
[165] R. Caldwell, M. G. Street, R. Sharma, P. Takmakov, B. Baker, and L. Rieth, "Characterization of Parylene-C degradation mechanisms: In vitro reactive accelerated aging model compared to multiyear in vivo implantation," *Biomaterials*, vol. 232, no. December 2019, p. 119731, 2020.
[166] L. Karumbaiah *et al.*, "Relationship between intracortical electrode design and chronic recording function," *Biomaterials*, vol. 34, no. 33, pp. 8061–8074, Nov. 2013.
[167] D. H. Szarowski *et al.*, "Brain responses to micro-machined silicon devices," *Brain Res.*, vol. 983, no. 1–2, pp. 23–35, 2003.
[168] M. P. Ward, P. Rajdev, C. Ellison, and P. P. Irazoqui, "Toward a comparison of microelectrodes for acute and chronic recordings," *Brain Res.*, vol. 1282, pp. 183–200, Jul. 2009.
[169] D. McCreery, S. Cogan, S. Kane, and V. Pikov, "Correlations between histology and neuronal activity recorded by microelectrodes implanted chronically in the cerebral cortex," *J. Neural Eng.*, vol. 13, no. 3, 2016.
[170] B. J. Black *et al.*, "Chronic recording and electrochemical performance of utah microelectrode arrays implanted in rat motor cortex," *J. Neurophysiol.*, vol. 120, no. 4, pp. 2083–2090, 2018.
[171] D. A. Henze, Z. Borhegyi, J. Csicsvari, A. Mamiya, K. D. Harris, and G. Buzsáki, "Intracellular features predicted by extracellular recordings in the hippocampus in vivo," *J. Neurophysiol.*, vol. 84, no. 1, pp. 390–400, 2000.
[172] T. D. Y. Kozai *et al.*, "Mechanical failure modes of chronically implanted planar silicon-based neural probes for laminar recording," *Biomaterials*, vol. 37, pp. 25–39, Jan. 2015.
[173] D. Byun, S. Cho, B. H. Lee, J. Min, J.-H. Lee, and S. Kim, "Recording nerve signals in canine sciatic nerves with a flexible penetrating microelectrode array," *J. Neural Eng.*, vol. 14, no. 4, p. 046023, 2017.
[174] B. Shafer, C. Welle, and S. Vasudevan, "A rat model for assessing the long-term safety and performance of peripheral nerve electrode arrays," *J. Neurosci. Methods*, vol. 328, no. August, p. 108437, 2019.
[175] J. C. Barrese, J. Aceros, and J. P. Donoghue, "Scanning electron microscopy of chronically implanted intracortical microelectrode arrays in non-human primates," *J. Neural Eng.*, vol. 13, no. 2, 2016.
[176] A. J. Bullard, "Feasibility of Using the Utah Array for Long-Term Fully Implantable Neuroprosthesis Systems," University of Michigan, 2019.
[177] Z. T. Irwin *et al.*, "Neural control of finger movement via intracortical brain-machine interface," *J. Neural Eng.*, vol. 14, no. 6, 2017.
[178] X. Xie *et al.*, "Bi-layer encapsulation of utah array based nerual interfaces by atomic layer deposited Al2O3 and parylene C," *2013 Transducers Eurosensors XXVII 17th Int. Conf.*

Solid-State Sensors, Actuators Microsystems, TRANSDUCERS EUROSENSORS 2013, no. June, pp. 1267–1270, 2013.
[179] N. Atapour, P. Majka, I. H. Wolkowicz, D. Malamanova, K. H. Worthy, and M. G. P. Rosa, "Neuronal Distribution across the Cerebral Cortex of the Marmoset Monkey (Callithrix jacchus)," *Cereb. Cortex*, vol. 29, no. 9, pp. 3836–3863, 2019.
[180] P. A. House, J. D. MacDonald, P. A. Tresco, and R. A. Normann, "Acute microelectrode array implantation into human neocortex: preliminary technique and histological considerations.," *Neurosurg. Focus*, vol. 20, no. 5, pp. 19–22, 2006.
[181] P. J. Rousche and R. A. Normann, "Chronic recording capability of the utah intracortical electrode array in cat sensory cortex," *J. Neurosci. Methods*, vol. 82, no. 1, pp. 1–15, 1998.
[182] P. A. Cody, J. R. Eles, C. F. Lagenaur, T. D. Y. Kozai, and X. T. Cui, "Unique electrophysiological and impedance signatures between encapsulation types: An analysis of biological Utah array failure and benefit of a biomimetic coating in a rat model," *Biomaterials*, vol. 161, pp. 117–128, 2018.
[183] C. G. Welle and D. Contreras, "Sensory-driven and spontaneous gamma oscillations engage distinct cortical circuitry," *J. Neurophysiol.*, vol. 115, no. 4, pp. 1821–1835, 2016.
[184] C. M. Bacmeister *et al.*, "Motor learning promotes remyelination via new and surviving oligodendrocytes," *Nat. Neurosci.*, vol. 23, no. 7, pp. 819–831, 2020.
[185] M. R. Chuapoco, M. Choy, F. Schmid, B. A. Duffy, H. J. Lee, and H. Lee, "Carbon monofilament electrodes for unit recording and functional MRI in same subjects," *Neuroimage*, vol. 186, pp. 806–816, 2019.
[186] D. Cai, K. B. Cohen, T. Luo, J. W. Lichtman, and J. R. Sanes, "NEW TOOLS FOR THE BRAINBOW TOOLBOX," *Nat. Methods*, vol. 10, no. 6, pp. 540–547, 2013.
[187] C. G. Welle and V. Krauthamer, "FDA regulation of invasive neural recording electrodes: A daunting task for medical innovators," *IEEE Pulse*, vol. 3, no. 2, pp. 37–41, 2012.
[188] F. Pothof *et al.*, "Chronic neural probe for simultaneous recording of single-unit, multi-unit, and local field potential activity from multiple brain sites," *J. Neural Eng.*, vol. 13, no. 4, 2016.
[189] J. K. Krauss *et al.*, "Technology of deep brain stimulation: current status and future directions," *Nat. Rev. Neurol.*, 2020.
[190] G. A. Clark *et al.*, "Using multiple high-count electrode arrays in human median and ulnar nerves to restore sensorimotor function after previous transradial amputation of the hand," *Conf. Proc. ... Annu. Int. Conf. IEEE Eng. Med. Biol. Soc. IEEE Eng. Med. Biol. Soc. Annu. Conf.*, vol. 2014, pp. 1977–1980, 2014.
[191] D. W. Tan, M. A. Schiefer, M. W. Keith, J. R. Anderson, J. Tyler, and D. J. Tyler, "A neural interface provides long-term stable natural touch perception," *Sci. Transl. Med.*, vol. 6, no. 257, 2014.
[192] P. P. Vu *et al.*, "Closed-Loop Continuous Hand Control via Chronic Recording of Regenerative Peripheral Nerve Interfaces," *IEEE Trans. Neural Syst. Rehabil. Eng.*, vol. 26, no. 2, pp. 515–526, 2018.
[193] S. Micera *et al.*, "Decoding information from neural signals recorded using intraneural electrodes: Toward the development of a neurocontrolled hand prosthesis," *Proc. IEEE*, vol. 98, no. 3, pp. 407–417, 2010.
[194] P. P. Vu *et al.*, "A regenerative peripheral nerve interface allows real-time control of an artificial hand in upper limb amputees," *Sci. Transl. Med.*, vol. 12, no. 533, pp. 1–12,

2020.
[195] S. Jezernik, M. Craggs, W. M. Grill, G. Creasey, and N. J. M. Rijkhoff, “Electrical stimulation for the treatment of bladder dysfunction: Current status and future possibilities,” *Neurol. Res.*, vol. 24, no. 5, pp. 413–430, 2002.
[196] B. Brembs, F. D. Lorenzetti, F. D. Reyes, D. A. Baxter, and J. H. Byrne, “Operant reward learning in Aplysia: Neuronal correlates and mechanisms,” *Science (80-.).*, vol. 296, no. 5573, pp. 1706–1709, 2002.
[197] M. D. Sunshine, F. S. Cho, D. R. Lockwood, A. S. Fechko, M. R. Kasten, and C. T. Moritz, “Cervical intraspinal microstimulation evokes robust forelimb movements before and after injury,” *J. Neural Eng.*, vol. 10, no. 3, 2013.
[198] A. J. Ciciriello, D. R. Smith, M. K. Munsell, S. J. Boyd, L. D. Shea, and C. M. Dumont, “IL-10 lentivirus-laden hydrogel tubes increase spinal progenitor survival and neuronal differentiation after spinal cord injury,” *Biotechnol. Bioeng.*, vol. Accepted, 2021.
[199] A. B. Schwartz, X. T. Cui, D. J. Weber, and D. W. Moran, “Brain-Controlled Interfaces: Movement Restoration with Neural Prosthetics,” *Neuron*, vol. 52, no. 1, pp. 205–220, 2006.
[200] G. A. Worrell, L. Parish, S. D. Cranstoun, R. Jonas, G. Baltuch, and B. Litt, “High-frequency oscillations and seizure generation in neocortical epilepsy,” *Brain*, vol. 127, no. 7, pp. 1496–1506, 2004.
[201] S. Reardon, “Electroceuticals spark interest.,” *Nature*, vol. 511, no. 7507, p. 18, 2014.